Study of Adsorption and Photochemical Behavior of Cationic Acridinium Derivatives on Clay Surface

Yuma YOSHIDA

March 2022

Preface

The thesis is based on the studies which were worked under the guidance of Professor Shinsuke Takagi at the Department of Applied Chemistry, Graduate Course of Urban Environmental Sciences, Tokyo Metropolitan University.

Yuma YOSHIDA

Department of Applied Chemistry

Graduate Course of Urban Environmental Sciences

Tokyo Metropolitan University

1-1 Minami-ohsawa, Hachiohji

Tokyo 192-0364, JAPAN

Contents

Chapter 1.General Introduction

1.1. Inorganic layered compounds as functional materials

Inorganic layered compounds are composed of inorganic nano-sheets laminated by electrostatic interactions, van der Waals forces, hydrogen bonds, and other interactions. Inorganic layered compounds are characterized by i) a large aspect ratio, ii) a large specific surface area, iii) a flat surface at the atomic level, iv) reversible exfoliation and lamination, v) the ability to intercalate various substances, and vi) the ability to adsorb various substances on the surface. Due to the specific properties described above, inorganic layered compounds have been utilized for various applications. For example, it has been utilized as catalysts[1–3], adsorbents[4,5], electrodes[6], and biological materials.[7,8] By modifying its surface and inserting various substances between its layers, new applications such as optical functional materials and improvements of the above applications have been promoted. [9-13]

Layered compounds not only intercalate substances in their interlayer space but also provide a specific reaction field. The hierarchy of flexibility and definition of reaction fields is shown in Figure 1.1. Gas state, liquid state, molecular assemblies such as micelle and

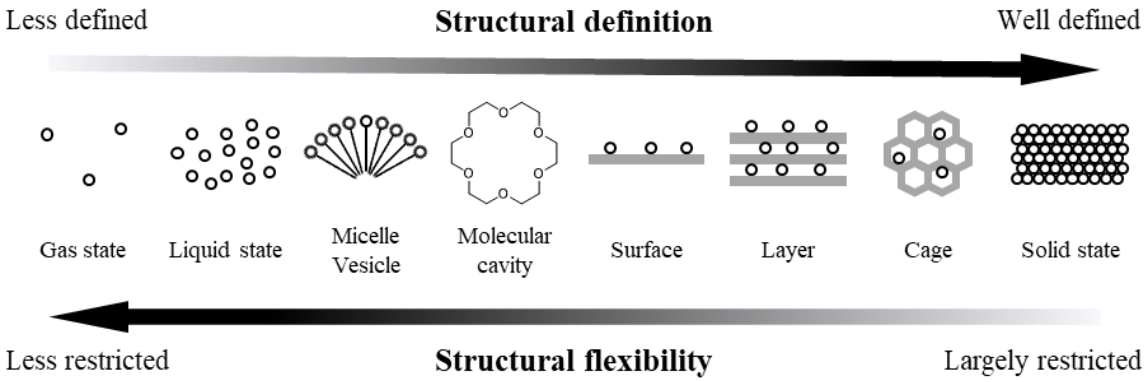

Figure 1.1 Structural flexibility and definition on the reaction filed.

vesicle, and solid-state are general chemical reaction fields. Each of these reaction fields has a different flexibility and is utilized depending on the purpose. Gas state and liquid state provide ideal reaction fields for physicochemical observation and measurement because gas state and liquid state are homogeneous systems. These homogeneous systems, such as gas and liquid state, have been widely used for a long time because it is easy to analyze kinetics theoretically.[14–16].

On the other hand, it is difficult to analyze the reaction mechanism in a molecular assembly and on the solid surface, which are heterogeneous systems, because the reaction mechanism is complicated. However, the tissues with advanced functions, such as biological tissues, are often composed of heterogeneous systems. Molecular assemblies, such as micelle and vesicle, have a function as heterogeneous systems in which molecules can be arranged at specific positions, while these are macroscopically uniform. Since the structural definition of molecular assemblies is not very high, the substance incorporated into the system has fluidity.[17–19] The solid-state and cage-shaped compounds such as zeolite have the advantage of designing selective chemical reactions using their high structural definition. By contrast, it has the disadvantage of being narrowly applicable due to its low structural flexibility.[20–22] Because layered compounds have an extremely flat two-dimensional surface, they are not as flexible as molecular assemblies such as micelles. On the other hand, the definition of layered compounds is not as high as that of the solid-state since layered compounds also have the flexibility that the interlayer distance is variable. Layered compounds, therefore, are materials that provide a chemical reaction field with flexibility and definition between molecular assemblies and solid states.

This thesis focused on clay minerals as layered compounds. Clay minerals have been

widely used for various applications because they are naturally ubiquitous materials and are characterized by swelling property, thermal stability, and ion adsorption property.[23–32] For example, they have been used as an adsorbent for a long time. They have also been utilized as filler materials to modify resin. In addition, much research has been conducted to apply clay minerals for new applications since clay minerals as host materials have received much attention in recent years. Because clay minerals have a flat surface at the atomic level, can be exfoliated into a single layer, and have optical transparency in a solution state, they have been investigated as photo-functional host materials. (For details, see Subsection 1.2.6.)

1.2. Clay minerals

Clay minerals are mainly composed of elements such as O, Si, Al, Mg, Fe, Ca, Na, K, and H, and there are many types. Most of them are layered silicates. Amorphous, low crystalline, and clay minerals with no layered structure are also defined as clay minerals in a broad sense.[33] This section describes the structure and composition of layered silicates.

1.2.1. Structure of clay minerals

Plane, sheet, and layer are used as the units that compose layered silicates. The plane is the network of which atoms and ions are arranged planarly. The sheet is the two-dimensional connection of a coordinated polyhedron. A layer is a composite unit in which sheets are combined. A Silicate sheet is composed of ionic bonds of O^{2-} anion with metal ions. The tetrahedral sheet and an octahedral sheet are composed by coordinating O^{2-} around the metal ion. The layered silicate is composed of a two-layered or three-layered structure in which the tetrahedral sheets and octahedral sheets are stacked. (Figure 1.2)

The tetrahedral sheet is composed of coordinating four O^{2-} anions around Si^{4+} cations. Three vertices of this tetrahedron are shared with adjacent tetrahedra and have a hexagonal array in two dimensions. (Figure 1.3) The fourth vertex is unshared with other tetrahedra and all tetrahedra point in the same direction. Three oxygen atoms shared with adjacent tetrahedra are called "bottom oxygen," the fourth oxygen atom is called "vertex oxygen." The vertex oxygen in the tetrahedral sheet is shared with octahedral sheets when tetrahedral sheets stack with octahedral sheets. Al^{3+} and Fe^{3+} are replaced as a center cation in the tetrahedral sheets instead of Si^{4+} (isomorphic substitution). The isomorphic substitution of Si^{4+} by Al^{3+} or Fe^{3+} in the tetrahedral sheet produces negative charges on the surface of clay minerals. The octahedral sheet is composed by coordinating six OH^- or O^{2-} anions around Mg^{2+}, Al^{3+}, Fe^{2+}, or Fe^{3+} and sharing their diagonals (Figure 1.4). If divalent elements are introduced in octahedral sheets, all cation positions are fulfilled (3-octahedral type). If trivalent elements

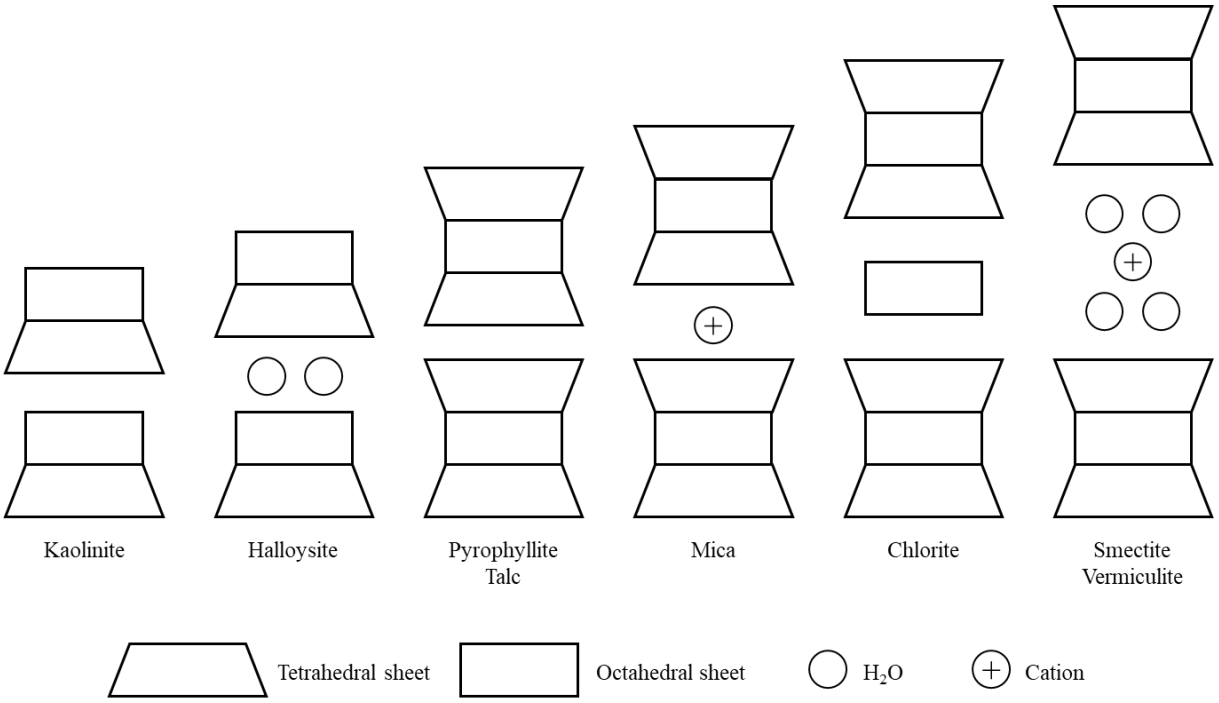

Figure 1.2 Schematic diagram of the structure of layered silicate.

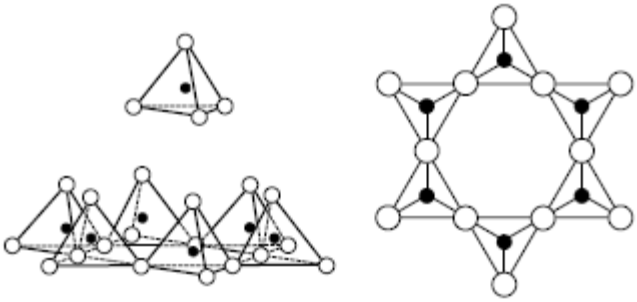

Figure 1.3 Structure of tetrahedral sheet

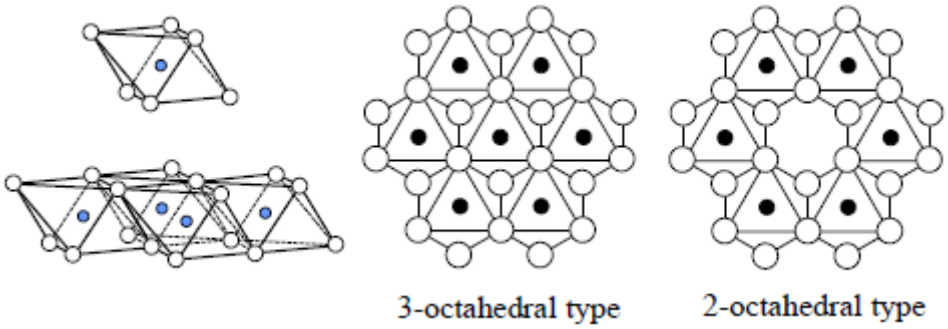

Figure 1.4 Structure of octahedral sheet.

are introduced in octahedral sheets, one-third of cation positions are empty (2-octahedral type). The octahedral sheet is also negatively charged depending on the ratio of central cations of octahedral sheets.

1.2.2. Classification of clay minerals

By sharing the anions of the tetrahedral sheet and octahedral sheet, these sheets can be conjugated. If one tetrahedral sheet and one octahedral sheet are conjugated, it is known as a 1:1 layer. If two tetrahedral sheets are conjugated on both sides of one octahedral sheet, it is known as a 1:2 layer. The layered silicates are composed of repeatedly stacking these layers. Generally, the interlayer has water molecules and counter cations. In some cases, only the 1:1 layer or 2:1 layer is laminated. The group of clay minerals is classified according to their composition of tetrahedral sheets and octahedral sheets, and the type of octahedral sheet is

classified according to the composition of octahedral sheets, and the name of clay minerals is classified according to the valence of cation in a polyhedron. The classification of clay

Table 1.1. Classification of Clay Minerals[34,35]

crystalloid	structure	type	group	octahedral type	name
crystalline	layer	1:1	kaolinite-serpentite	2	kaolinite
					dickite
					halloysite
				3	chrysotile
					lizardite
					antigorite
		2:1	pyrophyllite-talk	2	pyrophylite
					ferripyrophylite
				3	talc
					willemseite
					pimelite
			smectite	2	montmorillonite
					beidellite
					nontronite
				3	saponite
					hectorite
					sauconite
					stevensite
			vermiculite	2	dioctahedral vermiculite
				3	trioctahedral vermiculite
			mica	2	muscovite
					celadonite
					paragonite
					illite
				3	biotite
					phlogopite
					lepidolite
					polylithionite
			brittle mica	2	margarite
				3	clintonite
			chlorite	2	donbassite
				2−3	sudoite
				3	cookeite
	ribbon	2:1	sepiolite-palygorskite	3	sepiolite
					palygorskite
amorphous					allophane
					imogolite

minerals is shown in Table 1.1.

1.2.3. Properties of clay minerals

Clay minerals indicate the characteristics not found in other minerals due to their chemical composition, crystal structure, and being fine particles.

Ion-exchange ability

The surface of clay minerals is negatively or positively charged due to isomorphic substitution in tetrahedral sheets or octahedral sheets. The charged surface of clay minerals electrostatically adsorbs ions with opposite charges by Coulomb force and maintains electrical neutrality. Most of the electrostatically adsorbed ions are maintained on the clay surface with a relatively weak force. The exchange reaction occurs between ions on the clay surface and other ions in the solution when a solution containing other ions contacts with clay minerals. This reaction is called the ion exchange reaction. Not all ions adsorbed on the clay surface are exchanged. For example, K^+ and Cs^+ adsorbed on vermiculite are difficult to be exchanged by other ions.[36,37] Ions that can participate in the ion exchange reaction are called "exchangeable ions."

The ion-exchange ability of clay minerals is represented as a cation exchange capacity (CEC) or anion exchange capacity (AEC). CEC and AEC are expressed as equivalents of

Table 1.2. Cation Exchangeable Capacities of Clay Minerals[38]

name	cation exchange capacity (meq/100g)
kaolinite	1–15
smectite	70–130
vermiculite	130–200
sepiolite-palygorskite	<40

charge per 100 g of dry clay minerals. The CEC of clay minerals are shown in Table 1.2. The CEC, which is the number of cations per unit weight of clay minerals, represents the number of negative charges on the clay surface. The number of negative charges on the clay surface is an important parameter to discuss the adsorption phenomenon on the clay surface since it represents the average distance between negative charges. This subsection describes how to theoretically calculate the negative charge distance on the clay surface is described.

CEC (eq g^{-1}) is expressed as the number of negative charges per unit molecular weight as shown in Eq. (1.1).

$$CEC = \frac{n}{M} \tag{1.1}$$

where n represents the number of negative charges of the unit composition formula, M represents the molecular weight of the unit composition formula (g mol^{-1}). The specific surface area of clay minerals S (m g^{-2}) is expressed as shown in Eq. (1.2).

$$S = \frac{2abN_A}{M} \tag{1.2}$$

where N_A represents Avogadro number (mol^{-1}), a and b represent the width and depth of the unit cell (nm). The width and depth of the unit cell of smectite clays are shown in Table 1.3. The negative charge occupied area A is calculated by dividing the specific surface area by the number of negative charges per unit weight of clay minerals, as shown in Eq. (1.3).

Table 1.3. Unit Cell of Smectite[39]

name	*a* / nm	*b* / nm
montmorillonite	0.515	0.898
beidellite	0.515	0.895
nontronite	0.523	0.911
saponite	0.520	0.912
hectorite	0.525	0.918

$$A = \frac{S}{CECN_A} \tag{1.3}$$

If it is assumed that the negative charges on the clay surface are arranged hexagonally, the negative charge occupied area A is expressed using the average negative charge distance d (nm) as shown in Eq. (1.4).

$$A = \frac{\sqrt{3}}{2} d^2 \tag{1.4}$$

Therefore, the average negative charge distance d is expressed as shown in Eq. (1.5).

$$d = \sqrt{\frac{4ab}{\sqrt{3}n}} \tag{1.5}$$

Because the unit lattice constants a and b are unique values and n, which is the number of negative charges in the unit composition formula, is determined by the chemical composition of clay minerals, the average negative charge distance is estimated from the composition ratio of clay minerals. Clay minerals are natural compounds, whereas they can be synthesized artificially. It has been studied to control the average negative charge distance by adjusting the raw materials and the changing ratio during the synthesis of clay minerals. Details will be described later in 1.2.5.

Dispersion and aggregation[39]

Clay particles, which are fine particles, are well dispersed in water. The state in which particles are suspended in water is called dispersion, and the state in which dispersed particles are aggregated is called aggregation. The dispersion and aggregation are mainly governed by the balance of van der Waals force and electrostatic repulsion force between clay particles. The behavior of clay particles, when they are dispersed in water, is basically governed by the

theory of interfacial chemistry for general colloidal particles based on the electric double layer. However, it is extremely complex since it is affected by the shape of the clay particles, surface charge, and pH of the solution.

Adsorption[39]

It has been known that various substances are adsorbed on clay minerals. Clay minerals have an extremely large specific surface area since the structure of clay minerals is a layered structure. Since the clay surface is negatively charged, the interlayer space has cationic ions. Therefore, polar molecules interact with the anionic site on the clay surface by electrostatic interaction and adsorb on the clay surface by hydrogen bonding with oxygen and hydroxyl group on the clay surface. The adsorbed molecules may also coordinate with the cations in the interlayer.

1.2.4. Smectite clays[39]

Smectite is a dioctahedral or trioctahedral 2:1 layered silicate with water molecules in between the layers. The isomorphic substitution of Si^{4+} by Al^{3+} in the tetrahedral sheet or Si^{4+} and Al^{3+} by Al^{3+}, Mg^{2+}, and Fe^{2+} produces negative charges on the surface of smectite. The structure of typical smectite is shown in Figure 1.5. Cations such as Na^{+}, K^{+}, and Ca^{2+} in the

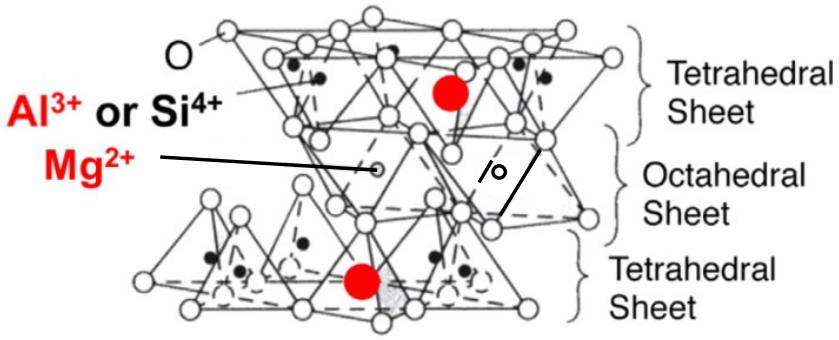

Figure 1.5. The unit structure of saponite.

interlayer neutralize the layer charge. These cations are exchangeable and can form organic complexes by incorporating various organic materials in addition to inorganic cations. It also has unique properties compared to other clay minerals, such as interlayer expansion due to the insertion of interlayer water and organic matter into the interlayer.

1.2.5. Synthesis of clay minerals

In order to utilize in industrial applications and elucidate the formation mechanism of clay minerals in nature, the synthesis of clay minerals, which are natural compounds, has been investigated for a long time.[40–47] Hydrothermal synthesis is generally used because clay minerals have structural water and OH^-. Hydrothermal synthesis is a method in which raw materials and water are mixed in a sealed container under high temperature and high pressure. A number of studies have investigated the types of raw materials, preparation ratios, and reaction conditions of the hydrothermal synthesis of clay minerals to control the chemical composition. For example, Madejová *et al.* reported the preparation method of reduced-charge montmorillonite by heating Li-montmorillonite.[48] Egawa *et al.* succeeded in controlling the distance between negative charges on the clay surface between 0.83 and 1.92 nm by adjusting the raw material preparation ratio of saponite in order to control the distance

Table 1.4. Chemical Formulas of Synthetic Saponites

synthetic saponite	negative charge distance / nm	$[(Si_{8-x}Al_x)(Mg_{6-y}Al_y)O_{20}(OH)_4]^{-(x-y)}$		
		x	y	x-y
Sap1.0	1.04	1.03	0.00	1.03
Sap1.2	1.20	0.80	0.03	0.77
Sap1.4	1.45	0.56	0.03	0.53
Sap1.6	1.57	0.45	0.00	0.45

between dyes adsorbed on clay minerals.[49] Table 1.4 shows the negative charge distances and chemical formulas of synthetic saponites reported in the previous literature.[49]

1.2.6. Dye-clay complex

It was known that organic dyes could be adsorbed on the clay surface since it was used as an adsorbent. For example, benzidine turns blue when adsorbed on montmorillonite. Weil-Malherde *et al*. reported that it was due to the transfer of unpaired electrons from the nitrogen atom of benzidine to montmorillonite, producing a monovalent radical cation with a blue color.[50] Villemure *et al.* also reported that the fluorescence was significantly enhanced by adsorbing methyl viologen onto montmorillonite. [51,52] It was found that clay minerals not only adsorb dyes on their surfaces or between their layers but also affect the photochemical properties of the dyes through some interaction with the dyes. These studies have led to widespread research on photo-functional materials using clay minerals. [53–57] However, it was found that many dyes are prone to forming H-aggregates or irregular aggregates. In particular, the electronic excitation time of the dye molecules was found to be significantly shorter when the aggregates were formed. [55,58,59]

Size-Matching Effect

Cationic porphyrins are adsorbed on the clay surface through electrostatic and hydrophobic interactions with the clay surface. The maximum wavelength of the cationic porphyrin *p*-TMPyP showed a red shift about 30 nm upon adsorption to the clay surface, indicating that the rotational substituents of porphyrins are planarized, and the π-conjugated system is extended by adsorption on the clay surface. [64,65] The absorbance at 450 nm derived from the adsorbed component and the absorbance at 420 nm derived from the non-adsorbed component showed

linearity in the Lambert-Beer plot, indicating that *p*-TMPyP does not show aggregation behavior. Takagi *et al.* have proposed this phenomenon as a "Size-Matching Effect" in which porphyrin molecules with multiple cations in the molecule adsorb onto the clay surface at high density without aggregation. [49,60-64]

Surface-Fixation Induced Emission

At the time when the fluorescence enhancement by complexation of methyl viologen with clay minerals was reported, no systematic study was conducted because it was often reported that dyes aggregate when adsorbed on clay. However, the report of the Size-Matching rule in which multivalent cationic dyes adsorb on clay minerals without aggregation led to the discovery that various dyes can be adsorbed on clay minerals without aggregation if the conditions are met. Furthermore, it was found that the photochemical properties of the dye were significantly changed by adsorption on clay minerals. For example, Tsukamoto *et al.* reported the effect of adsorption on clay minerals on the potential curves of the ground and excited states of triphenylbenzene derivatives.[66] The non-radiative deactivation constant of TPAB, which has rotational substituents, was significantly decreased by adsorption on clay minerals. It was suggested that the potential curves of the ground and excited states were sharpened, and the energy levels at the intersection of the potential curves were raised by the fixation of the rotational substituents due to adsorption on the clay surface. Tsukamoto *et al.* also reported on the effect of the clay surface on the potential curve from the changes in the integral of absorption coefficient, the radiative deactivation rate constant, and the non-radiative deactivation rate constants of Sb porphyrin with different positive valence on the clay surface.[67] Ishida *et al.* summarized the above two effects and proposed the fluorescence enhancement on

clay minerals and the associated potential curve change between the ground and excited states as Surface-Fixation Induced Emission (S-FIE).[68]

1.3. Adsorption

Adsorption is a phenomenon in which a substance concentrates at the interface of two layers that are in contact.[69] Unlike the atoms inside the material, the atoms at the interface are unsaturated and therefore have higher free energy than the atoms inside the material. Adsorption occurs when the free energy is reduced by the binding of molecules or ions to atoms at the interface. When molecules are adsorbed on a solid surface, the solid is called "adsorbent," and the molecules are called "adsorbate".[69]

1.3.1. Physisorption and chemisorption

Adsorption of molecules on the solid surface can be classified into physisorption and chemisorption.[70] Physisorption is a phenomenon in which an adsorbate is adsorbed on an adsorbent by a relatively weak interaction such as van der Waals force. The adsorption heat and activation energy of physisorption are generally small, and the adsorption rate is relatively fast. Since activation energy of desorption is also small, adsorption is reversible. On the other hand, chemisorption is a phenomenon in which adsorbate adsorb to the surface of the

Table 1.5. Physisorption and Chemisorption

	physisorption	chemisorption
adsorption speed	fast	slow
adsorption layer	mono-layer or multi-layer	mono-layer
adsorption enthalpy	~40 kJ/mol	200 kJ/mol
activation energy	small	large
reversibility	reversible	reversible or irreversible

adsorbent by forming chemical bonds. Since it can be regarded as a chemical reaction between adsorbent and adsorbent, its adsorption rate is slower than that of physical adsorption. The adsorption heat and activation energy are equivalent to the heat of the chemical reaction and the activation energy during the chemical reaction. Since the activation energy of desorption is the sum of the adsorption heat and the activation energy of adsorption, the activation energy of desorption of chemisorption is large. Chemisorption is, therefore, often irreversible.

1.3.2. Adsorption isotherms

The adsorption isotherm is the relationship between the pressure or concentration of the adsorbent and the amount adsorbed at a constant adsorption temperature. Direct and indirect methods are used to measure adsorption isotherms. The direct method is a method to directly determine the adsorption amount from the decrease in pressure or concentration of the adsorbent or the increase in weight of the adsorbent due to adsorption at a certain temperature.

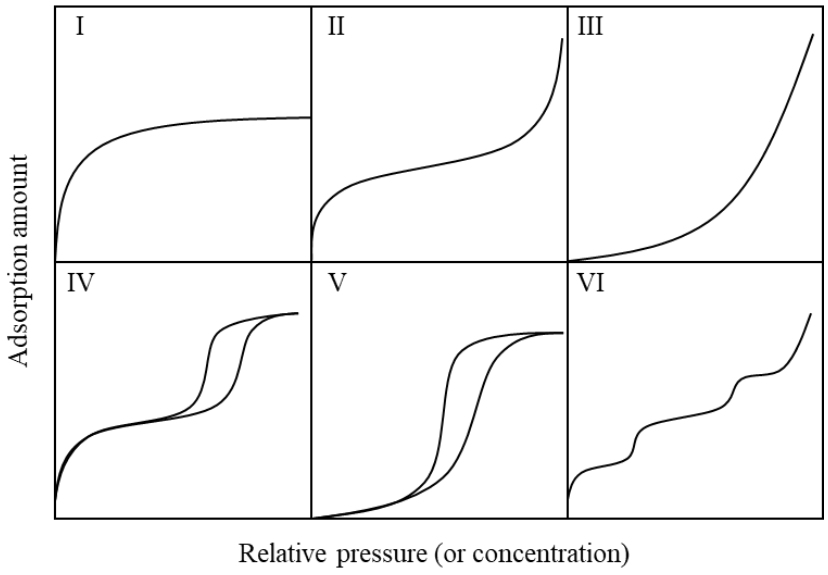

Figure 1.6. Types of adsorption isotherms.

The indirect method is a method to indirectly determine the adsorption amount from any physical change of adsorbent or adsorbate due to adsorption. A known example of the indirect method is a method in which a spectrometer measures adsorbents in a specific adsorption state.

IUPAC has classified typical adsorption isotherms into six types as shown in Figure 1.6.[71] In isotherms classified as Type I, the adsorption amount approaches a constant value as the pressure or concentration of the adsorbent increases. Type II is the isotherm of physical adsorption that forms the multilayer adsorption, represented by the BET (Brunauer-Emmett-Teller) equation. It is often the case that adsorption expressed as type II is physisorption, where the heat of adsorption is greater than the condensation heat of the adsorbent. Type III is also the isotherm of physical adsorption adopted at multilayer adsorption. The adsorption represented by type III is often the case of adsorption with the small adsorption heat equal to the condensation heat of the adsorbent. Type IV and type V are adsorption isotherms generally observed in physisorption. When the adsorption amount obtained by gradually increasing the adsorption equilibrium pressure is different from the adsorption amount obtained by gradually decreasing the equilibrium pressure, the adsorption is represented by type IV or type V adsorption isotherm. Similar to type II, type IV is observed when the heat of adsorption is large. Type V is observed when the heat of adsorption is as same as the condensation heat of adsorption, like type III. Type VI is the stepwise adsorption isotherm observed when the attraction between adsorbents forms the ordered adsorption layer. The expression of adsorption isotherm in the form of the mathematical equation is called the adsorption isotherm equation. In this section, Langmuir's adsorption isotherm, which is the adsorption isotherm treated in this paper, is described.

Langmuir adsorption isotherms

Langmuir adsorption isotherm is an adsorption isotherm for monolayer adsorption and is based on the following three assumptions. (i) Adsorption does not proceed beyond the monolayer. (ii) All adsorption sites are equivalent, and the surface is uniform. (iii) The adsorbates adsorb at the adsorption sites without interaction with each other. Langmuir adsorption isotherm is expressed as shown in Eq. (1.6). [72]

$$q = \frac{q_{max} K_{eq} C}{1 + K_{eq} C} \tag{1.6}$$

where q represents the adsorption amount at equilibrium (mol g^{-1}), C represents the equilibrium concentration (mol L^{-1}), and q_{max} represents the maximum monolayer adsorption capacity (mol g^{-1}). K_{eq} represents the concentration equilibrium constant of adsorption (L mol^{-1}). Especially, q_{max} and K are called Langmuir constants. K_{eq} denotes the affinity between the adsorbent and the adsorbate. The Langmuir equation (Eq. (1.6)) can be re-written as follows.[72]

$$\frac{C}{q} = \frac{1}{q_{max} K_{eq}} + \frac{C}{q_{max}} \tag{1.7}$$

Therefore, q_{max} and K_{eq} are calculated from the slope and intercept of the plot of C/q versus C. For the thermodynamic analysis described later in 1.4.2, K_{eq} needs to be converted into an apparent adsorption equilibrium constant explained by kinetics. K can be written by using K_{eq} as follow.

$$K = K_{eq} \frac{C_r}{\gamma_e} \tag{1.8}$$

C_r, which is typically 1 mol L^{-1}, is the molar concentration of the reference state. γ_e is the activity coefficient (unitless). The magnitude of the activity coefficient depends on the ionic

adsorbate concentration. When the adsorbate concentrations in this system are dilute, γ_e can be supposed to be 1. Therefore, the apparent equilibrium constant K is represented as follow:

$$K = K_{eq} C_r \quad (1.9)$$

1.4. Thermodynamics

1.4.1. Measurement method of thermodynamic parameters

In order to discuss the molecular recognition phenomena quantitatively, it is necessary to determine the thermodynamic parameters of each intermolecular interaction. In principle. the thermodynamic parameters are measured by calorimetric measurements. However, since accurate calorimetry requires many samples, sophisticated equipment, and measurement experiments, alternative methods are widely used.[73,74] The thermodynamic parameters are determined by measuring the equilibrium constants of the molecular recognition process by spectroscopic and electrochemical titration methods at several different temperatures and analyzing these with the van't Hoff equation. Because the thermodynamic parameters determined by the van't Hoff equation do not consider the temperature dependence of the enthalpy change, these are not accurate.[75,76] Therefore, there is a trade-off between the accuracy of the value and the convenience of the measurement. Furthermore, it should be noted that the treatment of thermodynamic parameters determined from equilibrium constants measured by titration and the comparison of the thermodynamic parameters determined from different methods.

1.4.2. Calculation method of thermodynamic parameters

In a typical stoichiometric host-guest interaction shown in Eq. (1.10), the association constant K is expressed as shown in Eq. (1.11).

$$Host + Guest \rightleftharpoons Host \cdot Guest \tag{1.10}$$

$$K = \frac{[Host][Guest]}{[Host \cdot Guest]} \tag{1.11}$$

Gibbs free energy change (ΔG) of this host-guest interaction is expressed using the association constant K as shown in Eq. (1.12).

$$\Delta G = -RT \ln K \tag{1.12}$$

where R is the gas constant (R = 8.314 J mol^{-1} K^{-1}), and T is the absolute temperature (K). The relationship between ΔG, ΔH, and ΔS is represented as follows.

$$\Delta G = \Delta H - T\Delta S \tag{1.13}$$

Substituting Eq. (1.12) into Eq. (1.13), van't Hoff equation is obtained.

$$\ln K = -\frac{\Delta H}{RT} + \frac{\Delta S}{R} \tag{1.14}$$

According to Eq. (1.14), the values of ΔH and ΔS are calculated from the slope and intercept of the linear plot of ln$K$ versus 1/T. In most cases, the plot of the natural logarithm of association constants at various temperatures and reciprocal temperatures gives a linear relationship. This calculation assumes that ΔH and ΔS do not change within the temperature range analyzed. However, this assumption overlooking the temperature dependence of ΔH and ΔS is not applicable if there is a difference in heat capacity between the right and left sides of Eq. (1.10).

1.4.3. Enthalpy-entropy compensation

The compensatory relationship of which these enthalpy and entropy has a positive correlation was observed in various host-guest systems in general and was reported as an empirical rule by Leffler.[77] Inoue *et al.* proposed that the slope in the ΔH-$T\Delta$S plot is used as an index of the structural change, and the intercept is used as an index of the desolvation.[78]

The report conducted by Inoue *et al.* has discussed the slope and intercept of enthalpy-entropy compensation by integrating the values of ΔH and $T\Delta S$ reported individually in various papers. The features of structural change and desolvation have been discussed by the slope and intercept of enthalpy-entropy compensations for molecular inclusion by cyclodextrin, cation capture by crown ether, and intercalation by DNA/RNA.[78–80] In particular, natural host-guest systems such as enzymes and DNA indicated slopes and intercepts. This result suggested that the structural change and the desolvation are largely due to their flexible structures. On the other hand, artificial host-guest systems such as crown ether and cryptand showed small slopes and intercepts, suggesting that the structural change and the desolvation are small due to their rigid structures.

1.5. Twisted intramolecular charge transfer (TICT)

Twisted intramolecular charge transfer (TICT) is a phenomenon reported by Grabowski, Rotkiewicz, and Rettig *et al.* in which a donor and acceptor are bound by a single bond.[81] In a polar environment, fast electron transfer occurs between the donor and acceptor in a molecule bound by covalent bonds. This electron transfer is accompanied by twisting between the donor and acceptor in the molecule, forming an orthogonal state of donor and acceptor. The equilibrium between the orthogonal state and the flattened state often results in dual fluorescence: fluorescence due to relaxation from the locally excited (LE) state in the high energy band and fluorescence due to relaxation from the charge transfer (CT) state in the low energy band. Since these relaxation pathways can be easily modulated by substituents, polarity, steric hindrance, and the surrounding environment, the TICT process has become one of the design strategies for functional molecules. Therefore, TICT-active molecules hold

great promise for OLEDs, chemical sensors, optoelectronic devices, and catalysis.

Aggregation-Induced Emission

The molecules exhibiting aggregation-induced emission (AIEgens) show a weak fluorescence when dissolved in good solvents but high fluorescence when aggregated in poor solvents or solids. AIEgens have been widely investigated in the field of optoelectronics, bio-imaging, and various applications.[82–84] In general, the restriction of intramolecular motion due to aggregation causes AIE. Tetraphenylethene, one of the most famous AIEgens, is known to form TICT state in the excited state,[85] and stilbene derivatives such as tetraphenylethene also often form TICT state in the excited state.[81] When these molecules are placed in a poor solvent environment, a strong fluorescence derived from the LE state is emitted since the aggregation of the molecules prevents the formation of TICT by restricting the torsion between donor and acceptor.

Catalyst

In order to efficiently utilize solar energy, it is necessary to maintain the charge separation state generated by photo-excitation for a long time. The charge separation state must be much faster than the charge recombination process, such as the reaction center in the natural photosynthesis system, to achieve a long-lived charge separation state. Molecular design that reduces the charge transfer interaction between donor and acceptor was a common strategy to suppress the charge recombination process. Therefore, charge separation has been studied in coupled systems where an insulating bridge or spacer separates the donor and acceptor. For example, in a ternary system of fullerene, ferrocene, and porphyrin, charge recombination was suppressed by a multi-step electron transfer reaction, resulting in a long-lived charge-separated

state.[86–88] However, when the charge separation state is obtained by multi-step electron transfer, the energy loss to reach the final charge separation state is large because the free energy change at each step is negative. Furthermore, it is difficult to synthesize molecules in which multiple molecules are covalently linked.

Molecules that form TICT states in the excited states can achieve charge separation in a single step. Molecules with rotatable bridges between donor and acceptor generate CT states accompanied by intramolecular structural changes from LE states of donor or acceptor. A similarly large structural change accompanies the transition from the excited state to the ground state. For example, it is known that 4-(dimethylamino)benzonitrile emits double fluorescence from the LE and CT states in polar solvents because the dimethylamino group and the benzene ring are orthogonal. Wasielewski *et al*. investigated the dynamics of charge separation in several twisted donor-acceptor systems where donor and acceptor are directly bound or connected by conjugated bridges.[89] As a result, it was suggested that the charge recombination from the sterically twisted donor-acceptor pair efficiently generates a locally excited triplet state. In addition, Fukuzumi *et al.* achieved a generation of long-lived charge separation state by a single bonded donor-acceptor pair such as 9-mesityl-10-methylacridinium.[90] (For details, Section 1.6)

1.6. Acridinium derivatives

Acridinium is a compound in which the nitrogen of acridine, a heterocyclic compound, is methylated. Acridinium shows a high fluorescence quantum yield due to its rigid structure, like anthracene. It also shows chemiluminescence when it reacts with hydrogen peroxide under a basic environment. For example, ester-linked acridinium derivatives and lucigenin,

in which two acridinium rings are linked via the 9-position, are utilized as immunoassays and target reagents.[91–93]

A number of studies have been investigated the dynamics of photoinduced electron transfer in acridinium derivatives in which various substituents conjugate to the 9-position with sterically twisted structures.[94–96] Since the acridinium group has high acceptor property, a donor-acceptor system can be designed by conjugating a functional group with high donor property to the 9-position. The mechanism has been proposed to generate an electron transfer state (CT) from a locally excited state (LE) of the acridinium group by very fast electron transfer from the donor moiety to the acceptor moiety. The electron transfer rate tuned over more than three orders of magnitude (ps to ns) depending on the substituents and solvent.

It has been previously observed that 9-mesityl-10-methylacridinium ($MesAcr^+$) forms a long-lived charge-separated state upon light irradiation because the ortho methyl group of the mesityl group acts as a steric hindrance and maintains the orthogonal state of donor and acceptor.[97–99] Many catalytic reactions based on the photo-redox potential using this charge separation state have been reported.[100–102] For example, $MesAcr^+$ is an efficient photocatalyst in the selective bromination of aromatic hydrocarbons such as 1,2,4-trimethoxybenzene using aqueous HBr solution as a Br source and O_2 as an oxidant under visible light irradiation.[103]

1.7. Purpose of this thesis

In recent years, various organic-inorganic complexes have been widely studied from the viewpoint of application to energy conversion materials and optical functional materials. In particular, complexes of inorganic layered compounds and photo-functional molecules have attracted much attention because they exhibit specific optical functions based on the orientation

and arrangement of the functional molecules in the two-dimensional field of the layered compound. Control of the adsorption and aggregation states of photo-functional molecules on solid surfaces is essential for developing their physical properties. In the case of cationic dye adsorbed on clay minerals, which is an example of active alignment and orientation of photo-functional molecules, it has been demonstrated that electrostatic interaction and hydrophobic interaction are the driving forces for the complex formation. On the other hand, the effects of host and guest structures on these driving forces have not been clarified. Because of the more significant guest interaction, monovalent cationic dyes may form aggregates on the clay surface. Optimization of the adsorption state of the monovalent cationic dye on the clay surface is expected to enhance its photo-function.

This thesis evaluated the adsorption behavior of mono-cationic acridinium derivatives on synthetic saponites with various negative charge densities on the surface. The purpose of this thesis is to clarify the driving force for the adsorption of cationic acridinium derivatives on synthetic saponite and the photophysical behavior of these complexes. In Chapters 2 and 3, we evaluated the effects of the guest molecule and host material structures on the adsorption of acridinium derivatives on clay minerals. In Chapter 4, we evaluated the compensation relationship between enthalpy changes and entropy changes for the adsorption of derivatives on clay minerals. In Chapter 5, we evaluated the fluorescence self-quenching behavior of acridinium derivatives on synthetic saponites. In Chapter 6, we evaluated the effects of guest and host structures on the fluorescence enhancement behavior of acridinium derivatives on synthetic saponites. In Chapter 7, we evaluated the effect of adsorption on a synthetic saponite on LE and CT fluorescence emitted from 9-mesityl-10-methylacridinium.

These investigations provide new strategies for using the complex of mono-cationic dyes

and clay minerals as photo-functional materials and will facilitate the organic-inorganic composites with new functions in the future.

1.8. references

1. Pinnavaia, T. J. Intercalated Clay Catalysts. *Science* **1983**, *220*, 365-371.
2. Tatsumi, T.; Yamamoto, K.; Tajima, H.; Tominaga, H. Shape Selective Epoxidation of Alkenes Catalyzed by Polyoxometalate-Intercalated Hydrotalcite. *Chem. Lett.* **1992**, *21*, 815-818.
3. Kudo, A.; Tanaka, A.; Domen, K.; Maruya, K.; Onishi, T. Photocatalytic Decomposition of Water Over NiO□$K_4Nb_6O_{17}$ Catalyst. *J. Catal.* **1988**, *111*, 67-76.
4. Juang, R. S.; Wu, F. C.; Tseng, R. L. The Ability of Activated Clay for the Adsorption of Dyes from Aqueous Solutions. *Environ. Technol.* **1997**, *18*, 525-531.
5. Orthman, J. A.; Zhu, H.; Lu, G. Q. Use of Anion Clay Hydrotalcite to Remove Coloured Organics from Aqueous Solutions. *Sep. Purif. Technol.* **2003**, *31*, 53-59.
6. Whittingham, M. S.; Gamble, F. R. The Lithium Intercalates of the Transition Metal Dichalcogenides. *Mater. Res. Bull.* **1975**, *10*, 363-371.
7. Danjo, M.; Mizuguchi, Y.; Yagita, Y.; Kakiguchi, K.; Yanagida, T.; Tsuhako, M. Intercalation of Anticancer Agent Cytarabine and Its Related Compounds into γ-Titanium Phosphate. *Bull. Chem. Soc. Jpn.* **1997**, *70*, 3011-3015.
8. Choy, J. H.; Kwak, S. Y.; Park, J. S.; Jeong, Y. J.; Portier, J. Intercalative Nanohybrids of Nucleoside Monophosphates and DNA in Layered Metal Hydroxide. *J. Am. Chem. Soc.* **1999**, *121*, 1399-1400.
9. Saupe, G. B.; Mallouk, T. E.; Kim, W.; Schmehl, R. H. Visible Light Photolysis of

Hydrogen Iodide Using Sensitized Layered Metal Oxide Semiconductors: The Role of Surface Chemical Modification in Controlling Back Electron Transfer Reactions. *J. Phys. Chem. B* **1997**, *101*, 2508-2513.

10. Motokura, K.; Tada, M.; Iwasawa, Y. Heterogeneous Organic Base-Catalyzed Reactions Enhanced by Acid Supports. *J. Am. Chem. Soc.* **2007**, *129*, 9540-9541.
11. Ras, R. H. A.; Umemura, Y.; Johnston, C. T.; Yamagishi, A.; Schoonheydt, R. A. Ultrathin Hybrid Films of Clay Minerals. *Phys. Chem. Chem. Phys.* **2007**, *9*, 918-932.
12. Ogawa, M.; Okutomo, S.; Kuroda, K. Control of Interlayer Microstructures of a Layered Silicate by Surface Modification with Organochlorosilanes. *J. Am. Chem. Soc.* **1998**, *120*, 7361-7362.
13. Okada, T.; Seki, Y.; Ogawa, M. Designed Nanostructures of Clay for Controlled Adsorption of Organic Compounds. *J. Nanosci. Nanotech*. **2014**, *14*, 2121-2134.
14. Lindemann, F. A.; Arrhenius, S.; Langmuir, I.; Dhar, N. R.; Perrin, J.; Lewis, W. C. McC. Discussion on "the Reaction Theory of Chemical Action." *Trans. Faraday Soc.* **1922**, *17*, 598-606.
15. Marcus, R. A. Chemical and Electrochemical Electron-Transfer Theory. *Ann. Rev. Phys. Chem.* **1964**, *15*, 155-196.
16. Richardson, W.; Volk, L.; Lau, K. H.; Lin, S. H.; Eyring, H. Application of the Singular Perturbation Method to Reaction Kinetics. *Proc. Natl. Acad. Sci. U.S.A.* **1973**, *70*, 1588-1592.
17. Landini, D.; Maia, A.; Montanari, F. Phase-Transfer Catalysis. Nucleophilicity of Anions in Aqueous Organic Two-Phase Reactions Catalyzed by Onium Salts. A Comparison with Homogeneous Organic Systems. *J. Am. Chem. Soc.* **1978**, *100*, 2796-

2801.

18. Starks, C. M. Phase-Transfer Catalysis. I. Heterogeneous Reactions Involving Anion Transfer by Quaternary Ammonium and Phosphonium Salts. *J. Am. Chem. Soc.* **1981**, *93*, 195-199.

19. Gordon, J. E.; Kutina, R. E. Theory of Phase-Transfer Catalysis. *J. Am. Chem. Soc.* **1977**, *99*, 3903-3909.

20. Dessau, R. M. Shape-Selective Platinum/ZSM-5 Catalysts. *J. Catal.* **1984**, *89*, 520-526.

21. Herron, N.; Tolman, C. A. A Highly Selective Zeolite Catalyst for Hydrocarbon Oxidation. A Completely Inorganic Mimic of the Alkane ω-Hydroxylases. *J. Am. Chem. Soc.* **1987**, *109*, 2837-2839.

22. Kim, J. H.; Sugi, Y.; Matsuzaki, T.; Hanaoka, T.; Kubota, Y.; Tu, X.; Matsumoto, M. Effect of $SiO_2Al_2O_3$ Ratio of H-mordenite on the Propylation of Naphthalene with Propylene. *Micropor. Mater.* **1995**, *5*, 113-121.

23. Tahir, S. S.; Rauf, N. Removal of a Cationic Dye from Aqueous Solutions by Adsorption onto Bentonite Clay. *Chemosphere* **2006**, *63*, 1842-1848.

24. Moet, A. S.; Akelah, A. Polymer-Clay Nanocomposites: Polystyrene Grafted onto Montmorillonite Interlayers. *Mater. Lett.* **1993**, *18*, 97-102.

25. Weimer, M. W.; Chen, H.; Giannelis, E. P.; Sogah, D. Y. Direct Synthesis of Dispersed Nanocomposites by in Situ Living Free Radical Polymerization Using a Silicate-Anchored Initiator. *J. Am. Chem. Soc.* **1999**, *121*, 1615-1616.

26. Hasegawa, N.; Kawasumi, M.; Kato, M.; Usuki, A.; Okada, A. Preparation and Mechanical Properties of Polypropylene-Clay Hybrids Using a Maleic Anhydride-Modified Polypropylene Oligomer. *J. Apply. Polym. Sci*. **1998**, *67*, 87-92.

27. Zilg, C.; Thomann, R.; Finter, J.; Mülhaupt, R. The Influence of Silicate Modification and Compatibilizers on Mechanical Properties and Morphology of Anhydride-Cured Epoxy Nanocomposites. *Macromol. Mater. Eng.* **2000**, *280-281*, 41-46.

28. Henmi, T.; Huang, P. M. Removal of Phosphorus by Poorly Ordered Clays as Influenced by Heating and Grinding. *Appl. Clay Sci.* **1985**, *1*, 133-144.

29. Danis, T. G.; Albanis, T. A.; Petrakis, D. E.; Pomonis, P. J. Removal of Chlorinated Phenols from Aqueous Solutions by Adsorption on Alumina Pillared Clays and Mesoporous Alumina Aluminum Phosphates. *Water Res*. **1998**, *32*, 295-302.

30. Celis, R.; HermosÍn, M. C.; Cornejo, J. Heavy Metal Adsorption by Functionalized Clays. *Environ. Sci. Technol.* **2000**, *34*, 4593-4599.

31. Ruiz-Hitzky, E. Conducting Polymers Intercalated in Layered Solids. *Adv. Mater.* **1993**, *5*, 334-340.

32. Blumstein, A. Polymerization of Adsorbed Monolayers. I. Preparation of the Clay–polymer Complex. *J. Polymer Sci.* **1965**, *3*, 2653-2664.

33. Guggenheim, S.; Martin, R. T. Definition of Clay and Clay Mineral: Joint Report of the Aipea Nomenclature and CMS Nomenclature Committees. *Clays Clay Miner.* **1995**, *43*, 255-256.

34. Bailey, S. W. Summary of Recommendations of AIPEA Nomenclature Committee. *Clays Clay Miner.* **1980**, *28*, 73-78.

35. Shichi, T.; Takagi, K. Clay Minerals as Photochemical Reaction Fields. *J. Photochem. Photobiol. C: Photochem. Rev.* **2000**, *1*, 113-130.

36. Sawhney, B. L. Selective Sorption and Fixation of Cations by Clay Minerals: A Review. *Clays Clay Miner.* **1972**, *20*, 93-100.

37. Staunton, S. Adsorption of Radiocaesium on Various Soils: Consequences of the Effects of Soil: Solution Composition on the Distribution Coefficient. *Eur. J. Soil Sci.* **1994**, *45*, 409-418.

38. Christidis, G. E. Chapter 4.1 - Assessment of Industrial Clays. in: Bergaya, F.; Lagaly, G. (Eds.), *Developments in Clay Science*, **2013**, *5*, 425-449.

39. *Handbook of Clays and Clay Minerals*, 3rd ed. The Clay Science Society of Japan 2009.

40. Vogels, R. J. M. J.; Kloprogge, J. T.; Geus, J. W. Synthesis and Characterization of Saponite Clays. *Am. Mineral.* **2005**, *90*, 931-944.

41. Iiyama, J. T.; Roy, R. Controlled Synthesis of Heteropolytypic (Mixed-Layer) Clay Minerals. *Clays Clay Miner.* **1961**, *10*, 4-22.

42. Iiyama, J. T.; Roy, R. Unusually Stable Saponite in the System Na_2O-MgO-Al_2O_3-SiO_2. *Clay Miner. Bull.* **1963**, *5*, 161-171.

43. Roy, D. M.; Roy, R. Synthesis and Stability of Minerals in the System MgO-Al_2O_3-SiO_2-H_2O. *Am. Mineral*. **1955**, *40*, 147-178.

44. Kloprogge, J. T.; Frost, R. L. The Effect of Synthesis Temperature on the FT-Raman and FT-IR Spectra of Saponites. *Vib. Spectrosc*. **2000**, *23*, 119-127.

45. Koizumi, M.; Roy, R. Synthetic Montmorillonoids with Variable Exchange Capacity. *Am. Mineral.* **1959**, *44*, 788-805.

46. Kuchta, L.; Fajnor, V. Š. Optimal Conditions for Hydrothermal Synthesis of Saponite. *Chem. Pap.* **1988**, *42*, 339-345.

47. Vogels, R. J. M. J.; Kerkhoffs, M. J. H. V.; Geus, J. W. Non-hydrothermal Synthesis, Characterization and Catalytic Properties of Saponite Clays. *Stud. Surf. Sci. Catal.* **1995**, *91*, 1153-1161.

48. Madejová, J.; Bujdák, J.; Gates, W. P.; Komadel, P. Preparation and Infrared Spectroscopic Characterization of Reduced-Charge Montmorillonite with Various Li Contents. *Clay Miner.* **1996**, *31*, 233-241.

49. Egawa, T.; Watanabe, H.; Fujimura, T.; Ishida, Y.; Yamato, M.; Masui, D.; Shimada, T.; Tachibana, H.; Yoshida, H.; Inoue, H.; Takagi, S. Novel Methodology To Control the Adsorption Structure of Cationic Porphyrins on the Clay Surface Using the "Size-Matching Rule." *Langmuir* **2011**, *27*, 10722-10729.

50. Weil-Malherbe, H.; Weiss, J. 436. Colour Reactions and Adsorption of Some Aluminosilicates. *J. Chem. Soc.* **1948**, 2164-2169.

51. Villemure, G.; Detellier, C.; Szabo, A. G. Fluorescence of Clay-intercalated Methylviologen. *J. Am. Chem. Soc.* **1986**, *108*, 4658-4659.

52. Villemure, G.; Detellier, C.; Szabo, A. G. Fluorescence of Methylviologen Intercalated into Montmorillonite and Hectorite Aqueous Suspensions. *Langmuir* **1991**, *7*, 1215-1221.

53. Schoonheydt, R. A.; De Pauw, P.; Vliers, D. Luminescence of Tris(2,2'-bipyridine)ruthenium(II) in Aqueous Clay Minerals Suspensions. *J. Phys. Chem.* **1984**, *88*, 5113-5118.

54. Suzuki, Y.; Tenma, Y.; Nishioka, Y. Efficient Nonlinear Optical Properties of Dyes Confined in Interlayer Nanospaces of Clay Minerals. *Chem. Asian J.* **2012**, *7*, 1170-1179.

55. Ogawa, M.; Kuroda, K. Photofunctions of Intercalation Compounds. *Chem. Rev.* **1995**, *95*, 399-438.

56. Grabolle, M.; Starke, M.; Resch-Genger, U. Highly Fluorescent Dye-Nanoclay Hybrid

Materials Made from Different Dye Classes. *Langmuir* **2016**, *32*, 3506-3513.

57. Wu, L.; Lv, G.; Liu, M. Adjusting the Layer Charges of Host Phyllosilicates to Prevent Luminescence Quenching of Fluorescence Dyes. *J. Phys. Chem. C* **2015**, *119*, 22625-22631.

58. Shichi, T.; Takagi, K. Clay Minerals as Photochemical Reaction Fields. *J. Photochem. Photobiol. C: Photochem. Rev.* **2000**, *1*, 113-130.

59. Kuykendall, V. G.; Thomas, J. K. Photophysical and Photochemical Studies of Ruthenium (Tris(bipyridine) on Hectorite. *J. Phys. Chem.* **1990**, *94*, 4224-4230.

60. Takagi, S.; Shimada, T.; Eguchi, M.; Yui, T.; Yoshida, H.; Tryk, D. A.; Inoue, H. High Density Adsorption of Cationic Porphyrins on Clay Layer Surfaces Without Aggregation: The Size-Matching Effect. *Langmuir* **2002**, *18*, 2265-2272.

61. Takagi, S.; Tryk, D. A.; Inoue, H. Photochemical Energy Transfer of Cationic Porphyrin Complexes on Clay Surface. *J. Phys. Chem. B* **2002**, *106*, 5455-5460.

62. Ishida, Y.; Shimada, T.; Masui, D.; Tachibana, H.; Inoue, H.; Takagi, S. Efficient Excited Energy Transfer Reaction in Clay/Porphyrin Complex Toward an Artificial Light-Harvesting System. *J. Am. Chem. Soc.* **2011**, *133*, 14280-14286.

63. Ishida, Y.; Masui, D.; Tachibana, H.; Inoue, H.; Shimada, T.; Takagi, S. Controlling the Micro-Adsorption Structure of Porphyrin Dye Assembly on Clay Surfaces Using the "Size-Matching Rule" for Constructing an Efficient Energy Transfer System. *ACS Appl. Mater. Interfaces* **2012**, *4*, 811-816.

64. Ishida, Y.; Masui, D.; Shimada, T.; Tachibana, H.; Inoue, H.; Takagi, S. The Mechanism of the Porphyrin Spectral Shift on Inorganic Nanosheets: The Molecular Flattening Induced by the Strong Host-Guest Interaction Due to the "Size-Matching Rule" *J. Phys.*

Chem. C **2012**, *116*, 7879-7885.

65. Takagi, S.; Shimada, T.; Yui, T.; Inoue, H. High Density Adsorption of Porphyrins onto Clay Layer without Aggregation: Characterization of Smectite-Cationic Porphyrin Complex. *Chem. Lett.* **2001**, *30*, 128-129.

66. Tsukamoto, T.; Shimada, T.; Takagi, S. Unique Photochemical Properties of p-Substituted Cationic Triphenylbenzene Derivatives on Clay Layer Surface. *J. Phys. Chem. C* **2013**, *117*, 2774-2779.

67. Tsukamoto, T.; Shimada, T.; Takagi, S. Photochemical Properties of Mono-, Tri-, Penta-Cationic Antimony(V) Metalloporphyrin Derivatives on Clay Layer Surface. *J. Phys. Chem. A* **2013**, *117*, 7823-7832.

68. Ishida, Y.; Shimada, T.; Takagi, S. "Surface-Fixation Induced Emission" of Porphyrazine Dye by a Complexation with Inorganic Nanosheets. *J. Phys. Chem. C* **2014**, *118*, 20466-20471.

69. Calvert, J. G. Glossary of Atmospheric Chemistry Terms. *Pure Appl. Chem*. **1990**, *62*, 2167-2219.

70. Oura, K.; Lifshits, V. G.; Saranin, A. A.; Zotov, A. V.; Katayama, M. *Surface Science*, An Introduction. Springer 2003.

71. Sing, K. S.; Everett, D. H.; Haul, R. A.; Moscou, L.; Pierotti, R. A.; Rouquérol, J.; Siemieniewska, T. Reporting Physisorption Data for Gas/solid Systems with Special Reference to the Determination of Surface Area and Porosity. *Pure Appl. Chem.* **1985**, *57*, 603-619.

72. Ghosal, P. S.; Gupta, A. K. Determination of Thermodynamic Parameters from Langmuir Isotherm Constant-Revisited. *J. Mol. Liq.* **2017**, *225*, 137-146.

73. Grime, J. K. *Analytical Solution Calorimetry*; Wiley: New York, 1985.

74. Inoue, Y.; Wada, T. *Incomprehensive Supramolecular Chemistry*; Pergamon: Oxford 1996, Vol. 8, Chapter 1, Section 4.1.

75. Smithrud, D. B.; Wyman, T. B. Enthalpically Driven Cyclophane-Arene Inclusion Complexation: Solvent-Dependent Calorimetric Studies. *J. Am. Chem. Soc*. **1991**, *113*, 5420-5426.

76. Naghibi, H.; Tamura, A. Significant Discrepancies Between van't Hoff and Calorimetric Enthalpies. *Proc. Natl. Acad. Sci. U.S.A.* **1995**, *92*, 5597-5599.

77. Leffler, J. E. The Interpretation of Enthalpy and Entropy Data. *J. Org. Chem.* **1966**, *31*, 533-537.

78. Rekharsky, M. V.; Inoue, Y. Complexation Thermodynamics of Cyclodextrins. *Chem. Rev.* **1998**, *98*, 1875-1917.

79. Liu, Y.; Tong, L. H.; Tian, B. Z.; Inoue, Y.; Hakushi, T. Complexation Thermodynamics of Bis(Crown Ether)s. 4. Calorimetric Titration of Intramolecular Sandwich Complexation of Thallium and Sodium Ions with Bis(15-crown-5)s and Bis(12-crown-4)s: Enthalpy-Entropy Compensation. *J. Phys. Chem.* **1990**, *94*, 2666-2670.

80. Inoue, Y.; Wada, T. *Advances in Supramolecular Chemistry*, 1997, vol.4, 55-96.

81. Grabowski, Z. R.; Rotkiewicz, K.; Rettig, W. Structural Changes Accompanying Intramolecular Electron Transfer: Focus on Twisted Intramolecular Charge-Transfer States and Structures. *Chem. Rev.* **2003**, *103*, 3899-4032.

82. Hong, Y.; Lam, J. W. Y.; Tang, B. Z. Aggregation-Induced Emission. *Chem. Soc. Rev*. **2011**, *40*, 5361-5388.

83. Mei, J.; Lam, J. W. Y.; Qin, A.; Tang, Y.; Tang, B. Z. Aggregation-Induced Emission: The Whole Is More Brilliant than the Parts. *Adv. Mater.* **2014**, *26*, 5429-5479.

84. Kwok, R. T.; Leung, C. W. T.; Lam, J. W. Y.; Tang, B. Z. Biosensing by Luminogens with Aggregation-Induced Emission Characteristics. *Chem. Soc. Rev.* **2015**, *44*, 4428-4238.

85. Dong, Y.; Lam, J. W. Y.; Qin, A.; Liu, J.; Li, Z.; Tang, B. Z. Aggregation-Induced Emissions of Tetraphenylethene Derivatives and their Utilities as Chemical Vapor Sensors and in Organic Light-Emitting Diodes. *Appl. Phys. Lett.* **2007**, *91*, 011111.

86. Imahori, H.; Guldi, D. M.; Tamaki, K.; Yoshida, Y.; Luo, C.; Sakata, Y.; Fukuzumi, S. Charge Separation in a Novel Artificial Photosynthetic Reaction Center Lives 380 ms. *J. Am. Chem. Soc*. **2001**, *123*, 6617-6628.

87. Fukuzumi, S.; Ohkubo, K.; Imahori, H.; Shao, J.; Ou, Z.; Zheng, G.; Chen, Y.; Pandey, R. K.; Fujitsuka, M.; Ito, O.; Kadish, K. M. Photochemical and Electrochemical Properties of Zinc Chlorin−C60 Dyad as Compared to Corresponding Free-Base Chlorin−C60, Free-Base Porphyrin−C60, and Zinc Porphyrin−C60 Dyads. *J. Am. Chem. Soc.* **2001**, *123*, 10676-10683.

88. Guldi, D. M.; Imahori, H.; Tamaki, K.; Kashiwagi, Y.; Yamada, H.; Sakata, Y.; Fukuzumi, S. A Molecular Tetrad Allowing Efficient Energy Storage for 1.6 s at 163 K. *J. Phys. Chem. A* **2004**, *108*, 541-548.

89. Dance, Z. E.; Mickley, S. M.; Wilson, T. M.; Ricks, A. B.; Scott, A. M.; Ratner, M. A.; Wasielewski, M. R. Intersystem Crossing Mediated by Photoinduced Intramolecular Charge Transfer: Julolidine−Anthracene Molecules with Perpendicular π Systems. *J. Phys. Chem. A* **2008**, *112*, 4194-4201.

90. Fukuzumi, S.; Kotani, H.; Ohkubo, K.; Ogo, S.; Tkachenko, N. V.; Lemmetyinen, H. Electron-Transfer State of 9-Mesityl-10-methylacridinium Ion with a Much Longer Lifetime and Higher Energy Than That of the Natural Photosynthetic Reaction Center. *J. Am. Chem. Soc*. **2004**, *126*, 1600-1601.

91. Krzymiński, K.; Roshal, A. D.; Zadykowicz, B.; Białk-Bielińska, A.; Sieradzan, A. Chemiluminogenic Properties of 10-Methyl-9-(phenoxycarbonyl)acridinium Cations in Organic Environments. *J. Phys. Chem. A* **2010**, *114*, 10550-10562.

92. Krzymiński, K.; Ożóg, A.; Malecha, P.; Roshal, A. D.; Wróblewska, A.; Zadykowicz, B.; Błażejowski, J. Chemiluminogenic Features of 10-Methyl-9-(phenoxycarbonyl)acridinium Trifluoromethanesulfonates Alkyl Substituted at the Benzene Ring in Aqueous Media. *J. Org. Chem*. **2011**, *76*, 1072-1085.

93. Maskiewicz, R.; Sogah, D.; Bruice, T. C. Chemiluminescent Reactions of Lucigenin. 2. Reactions of Lucigenin with Hydroxide Ion and Other Nucleophiles. *J. Am. Chem. Soc.* **1979**, *101*, 5355-5364.

94. Jones II, G.; Farahat, M. S.; Greenfield, S. R.; Gosztola, D. J.; Wasielewski, M. R. Ultrafast Photoinduced Charge-Shift Reactions in Electron Donor-Acceptor 9-Arylacridinium Ions. *Chem. Phys. Lett*. **1994**, *229*, 40-46.

95. Horng, M. L.; Dahl, K.; Jones II, G.; Maroncelli, M. Electron Transfer in a Donor-Substituted Acridinium Dye: Evidence for Dynamical Solvent Control. *Chem. Phys. Lett*. **1999**, *315*, 363-370.

96. Benniston, A. C.; Harriman, A.; Li, P.; Rostron, J. P.; van Ramesdonk, H. J.; Groeneveld, M. M.; Zhang, H.; Verhoeven, J. W. Charge Shift and Triplet State Formation in the 9-Mesityl-10-methylacridinium Cation. *J. Am. Chem. Soc.* **2005**, *127*, 16054-16064.

97. Ohkubo, K.; Kotani, H.; Fukuzumi, S. Misleading Effects of Impurities Derived from the Extremely Long-Lived Electron-Transfer State of 9-Mesityl-10-methylacridinium Ion. *Chem. Commun.* **2005**, 4520-4522.

98. Tanaka, M.; Ohkubo, K.; Gros, C. P.; Guilard, R.; Fukuzumi, S. Persistent Electron-Transfer State of a π-Complex of Acridinium Ion Inserted between Porphyrin Rings of Cofacial Bisporphyrins. *J. Am. Chem. Soc.* **2006**, *128*, 14625-14633.

99. Tsukada, T.; Kotani, H.; Ohkubo, K.; Nakagawa , T.; Tkachenko, N. V.; Lemmetyinen, H.; Fukuzumi, S. Photoinduced Electron Transfer in 9-Substituted 10-Methylacridinium Ions. *Chem. Eur. J*. **2014**, *23*, 1306-1317.

100. Ohkubo, K.; Nanjo, T.; Fukuzumi, S. Efficient Photocatalytic Oxygenation of Aromatic Alkene to 1,2-Dioxetane with Oxygen via Electron Transfer, *Org. Lett*. **2005**, *7*, 4265-4268.

101. Joshi-Pangu, A.; Lévesque, F.; Roth, H. G.; Oliver, S. F.; Campeau, L.; Nicewicz, D. A.; Dirocco, D. Acridinium-Based Photocatalysts: A Sustainable Option in Photoredox Catalysis. *J. Org. Chem*. **2016**, *81*, 7244-7249.

102. Mcmanus, J. B.; Nicewicz, D. A. Direct C–H Cyanation of Arenes via Organic Photoredox Catalysis. *J. Am. Chem. Soc.* **2017**, *139*, 2880-2883.

103. Ohkubo, K.; Mizushima, K.; Iwata, R.; Fukuzumi, S. Selective Photocatalytic Aerobic Bromination with Hydrogen Bromide via an Electron-Transfer State of 9-Mesityl-10-methylacridinium Ion. *Chem. Sci.* **2011**, *2*, 715-722.

Chapter 2. Effect of the Molecular Structure on Adsorption of Acridinium Derivatives on the Clay Surface

2.1. Introduction

Clay minerals are composed of a two-layered or three-layered structure in which the tetrahedral sheets and octahedral sheets are stacked. The isomorphic substitution of Si^{4+} by Al^{3+} in the tetrahedral layer produces negative charges on the surface of clay minerals (Figure 1.5). Clay minerals have been used for various purposes because they have the properties such as ion adsorption capacity, swelling property, thermal stability, and these are naturally ubiquitous materials.[1–3] Furthermore, since clay minerals have a flat surface at the atomic level, can be exfoliated into a single layer, and have optical transparency in a solution state, they have been investigated as photo-functional host materials as well.[4–13] In order to utilize clay minerals as photo-functional materials, they are often used as complexes in which some molecules are adsorbed. So far, various studies have been investigated the adsorption behavior of cationic molecules on clay minerals. However, cationic molecules tend to aggregate on the solid surface due to interaction between guest molecules because intercalation of guest molecules between the layers of the laminated clay minerals makes the interaction between guest molecules easy.[14–16] Since it is difficult to analyze the interaction between guest molecules and the clay surface in such cases, the adsorption factor has not been clarified

in detail.[17–20] Therefore, the evaluation of the relationship between the parameters that affect the electrostatic interaction, the van der Waals force, and the hydrophobic interaction, which are the interactions between the clay surface and the guest molecule, is insufficient. Selecting the appropriate adsorbates and the conditions in which the nanosheets are exfoliated enables us to discuss the interaction between adsorbents and adsorbates without aggregation.

In this chapter, we focused on the effect of molecular structure on interactions in adsorption. In order to evaluate the effect of the molecular structure, it is necessary to be able to change the substituents for a certain basic molecular structure systematically. Acridinium derivatives are mono-cationic dyes and can have various substituents and counter anions. The effect of the molecular structure on interactions in adsorption was investigated by evaluating the thermodynamic parameters of adsorption of acridinium derivatives shown in Figure 2.1. Sumecton SA, a synthetic saponite, was selected as the adsorbent because it has a very high dispersity in water and can be kept completely peeled off. Thus, this can be expected to simplify the adsorption phenomenon and make the analysis easy. This study can also be expected to clarify the effect of molecular structure on the adsorption of the cationic molecule on the clay surface and what interactions are dominant. In addition, acridinium derivatives,

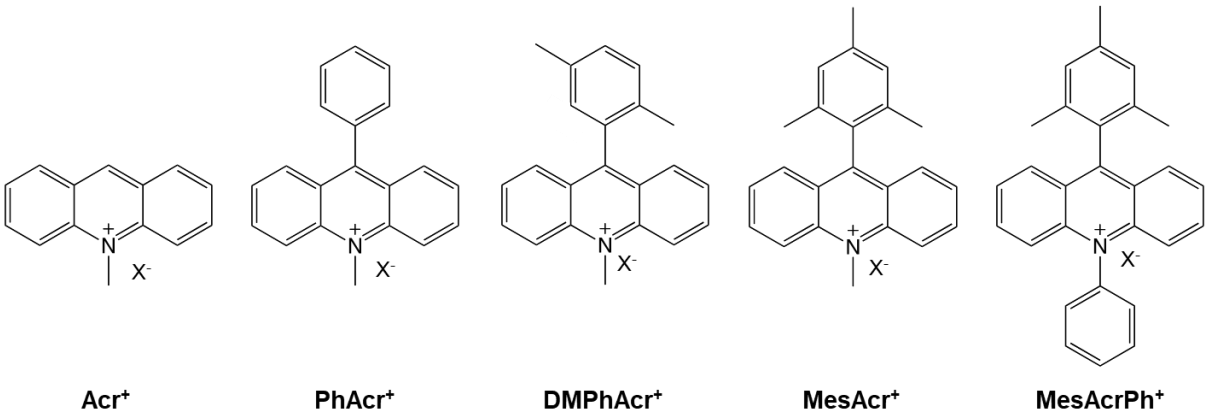

Figure 2.1. Structures of acridinium derivatives. The counter ion X^- is perchlorate or chloride

such as 9-mesityl-10-methylacridinium, have attracted attention as a photo-redox catalyst because this molecule can generate a long-lived electron-transfer state due to their orthogonal geometry.[21–23] Moreover, extensive research has been devoted to improving their photo-function and developing solid catalysts by incorporating acridinium derivatives into adsorbents.[24–26] On the other hand, little is currently known about the adsorption of acridinium derivatives on the clay surface.[27,28] The purpose of this chapter is also to provide a hint for establishing suitable conditions for the complexation of clay-acridinium derivatives.

2.2. Experimental section

2.2.1. Materials

Clay minerals (saponite): Sumecton SA (Sap1.2, $(Si_{7.2}Al_{0.8})(Mg_{5.97}Al_{0.03})O_{20}(OH)_4]^{-0.77}$ $(Na_{0.49}Mg_{0.14})^{+0.77}$) as a synthetic saponite was purchased from Kunimine Industries Co., Ltd. and was used without further purification. The unit structure of synthetic saponite is shown in Figure 1.5. Sap1.2 was analyzed with atomic force microscopy (AFM), X-ray diffraction (XRD), X-ray fluorescence (XRF), and Fourier transform infrared spectroscopy (FT-IR), as described in the previous paper.[29] Judging from AFM measurements, the shape of Sap1.2 is disc-like, and the diameter is 20–50 nm. The specific surface area and the cation exchange capacity (CEC) of Sap1.2 are 750 $m^2\ g^{-1}$ and 9.97×10^{-4} equiv. g^{-1}, respectively.[30] The area occupied per one negative charge calculated from the specific surface area and CEC is 1.25 nm^2. The aqueous dispersion of synthetic saponites, whose particle size is 100 nm or less, is substantially transparent in the UV-visible range. The water was deionized with an ORGANO BB-5A system (PF filter ×2 + G-10 column). 9-Phenyl-10-methylacridinium perchlorate, 9-(2,5-dimethylphenyl)-10-methylacridinium perchlorate, and 9-mesityl-10-methylacridinium

perchlorate were purchased from Tokyo Kasei (Japan). 10-Methylacridinium methyl sulfate and 9-mesityl-10-phenylacridinium tetra-fluoroborate were purchased from Aldrich. The counter ion was exchanged to perchlorate or chloride with an ion-exchange resin (Organo, Amberlite Resin IRA-400 treated with $HClO_4$ or HCl).

2.2.2. Analysis

TG-DTA curves were measured with Shimadzu DTG-60H analyzer to determine the water content of acridinium derivatives and Sap1.2. The temperature was ramped from room temperature to 120℃ with a heating rate of 10℃/min under dry air as a purge gas and was held for 60 minutes. Absorption spectra were obtained on a UV-3150 UV-vis. spectrophotometer (SHIMADZU). Molecular models of acridinium derivatives were depicted by molecular drawing software (i.e., Chem 3D). The structures of the molecular model were optimized by a semi-empirical molecular orbital method using MOPAC 2016. The calculation was carried out by using the following command: PM6 CHARGE=1 GRAPHF AUX BONDS DENSITY PI ENPART MMOK. The height of acridinium derivatives from its aromatic plane was calculated by the optimized structure. The projected cross-section of acridinium derivatives horizontal to its aromatic plane was defined as the molecular cross-section and was calculated by image processing software (i.e., Image J). The charge density at nitrogen atom and energy levels of HOMO and LUMO in acridinium derivatives were calculated by DFT calculation performed at B3LYP/6-31G* level using Gaussian09 package.[31]

2.2.3. Sample preparation for the acridinium derivatives/clay complex

1.0×10^{-4} M stock solutions of acridinium derivatives and 1.0×10^{-4} equiv. L^{-1} stock dispersion of Sap1.2 were prepared in water. In order to prepare the acridinium derivatives-

Sap1.2 complex, the stock solution of acridinium derivatives, stock dispersion of Sap1.2, and water were mixed arbitrarily under stirring in a quartz cell (1.0 × 1.0 cm). The concentration of acridinium derivatives was adjusted in a concentration range of $2.28 \times 10^{-6} – 2.59 \times 10^{-5}$ M. The concentration of Sap1.2 was adjusted in a concentration range of 1.06×10^{-5}–1.40×10^{-5} equiv. L^{-1}. By changing the volume of acridinium derivatives stock solution and Sap1.2 stock dispersion, the adsorption density of acridinium derivatives was adjusted to be 16.3, 24.5, 32.6, 40.8, 48.9, 57.1, 65.2, 73.4, 81.5, 97.8, 122.3, 163.0, 244.6% vs. CEC of Sap1.2.

2.3. Results and discussion

2.3.1. Adsorption behavior of acridinium derivatives on Sap1.2

The adsorption behavior was examined by measuring the UV-vis absorption spectra of acridinium derivatives. Figure 2.2 shows the UV-vis absorption spectra of acridinium derivatives with and without Sap1.2 in water. The spectra of each acridinium derivative with Sap1.2 at 16.3% vs. CEC showed a redshift by approximately 3 nm compared to that without Sap1.2. The redshift of maximum absorption wavelength indicates the adsorption of acridinium derivatives on the clay surface. Previous reports have demonstrated that the causes of this phenomenon are the change in molecular structure [8,11,29,32] and the aggregation on the clay surface.[33,34] The arbitrary observed spectra could be expressed by the spectral fitting using the spectrum in water and the spectrum of 16.3% vs. CEC. Furthermore, the absorption spectra of acridinium derivatives with and without Sap1.2 showed isosbestic points in association with increasing loading level, as shown in Figure S2.1–S2.5. These isosbestic points indicated that these spectral changes were expressed by the equilibrium system with two components: adsorbed and non-adsorbed components. No isosbestic point could not be

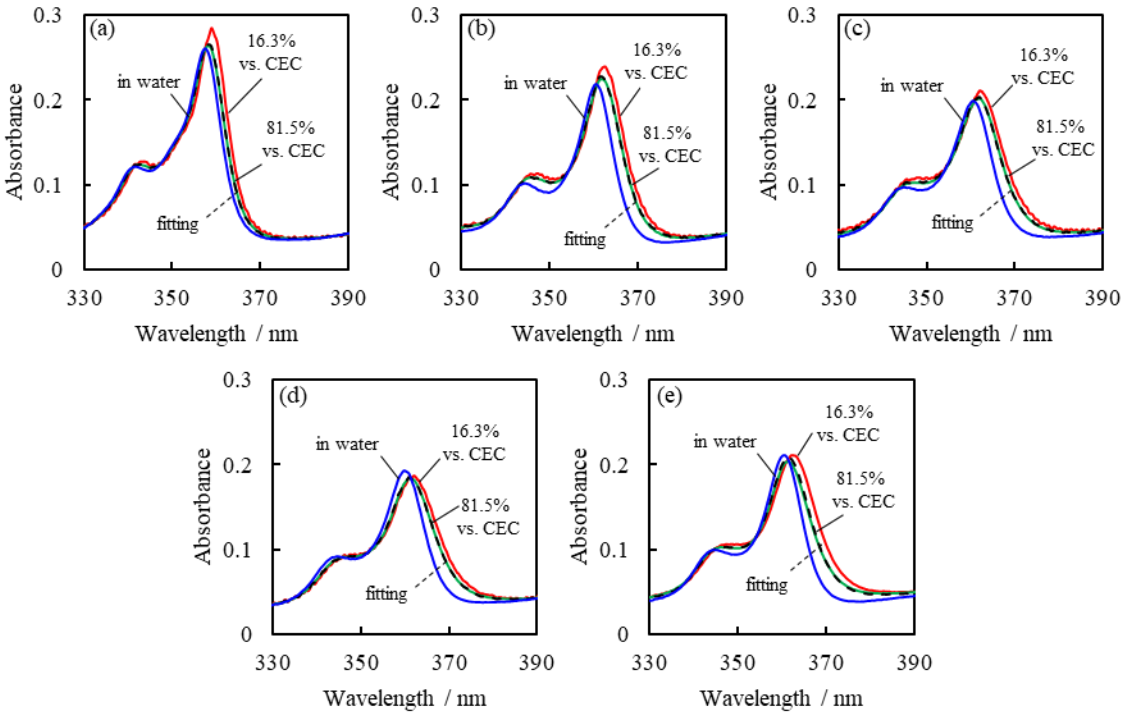

Figure 2.2. UV-vis absorption spectra of acridinium derivatives with and without Sap1.2 in water at 298.15 K. (a) Acr^+, (b) $PhAcr^+$, (c) $DMPhAcr^+$, (d) $MesAcr^+$, and (e) $MesPhAcr^+$ The spectra were corrected with each acridinium derivatives concentration.

observed if aggregates formed. Therefore, it was suggested that the change in absorption spectra of acridinium derivatives on the surface of synthetic saponite was not the aggregation but the change in molecular structure.

2.3.2. Langmuir adsorption isotherms

An adsorption isotherm means the relationship between the adsorbate concentration and the adsorption amount in the adsorption equilibrium state at a certain temperature. The adsorption isotherm shape depends on the combination of adsorbent and adsorbate. Because the absorption spectra of acridinium derivatives-Sap1.2 system were expressed by the two-components equilibrium system of adsorbed and non-adsorbed components as shown in Subsection 2.3.1, these systems could satisfy the assumption of Langmuir adsorption isotherm

described in Subsection 1.3.2. Hence, we calculated the adsorption amount from UV-vis absorption spectra and analyzed the adsorption parameters using Langmuir adsorption isotherms.

In order to obtain thermodynamic parameters from the van't Hoff plot, the adsorption equilibrium constants at 293.15–313.15 K were measured. The UV-vis adsorption spectra of five acridinium derivatives at each loading level at each temperature are shown in Figure S2.1–S2.5. Figure 2.3 shows the Langmuir plots calculated from the absorption spectral change in Figure S2.1–S2.5. As can be seen, the plots were straight for all acridinium derivatives at each temperature. The parameters q_{max}, $K_{eq,}$ and ΔG, calculated from these Langmuir plots, are summarized in Table 2.1. In general, it is difficult to analyze the adsorption of mono-

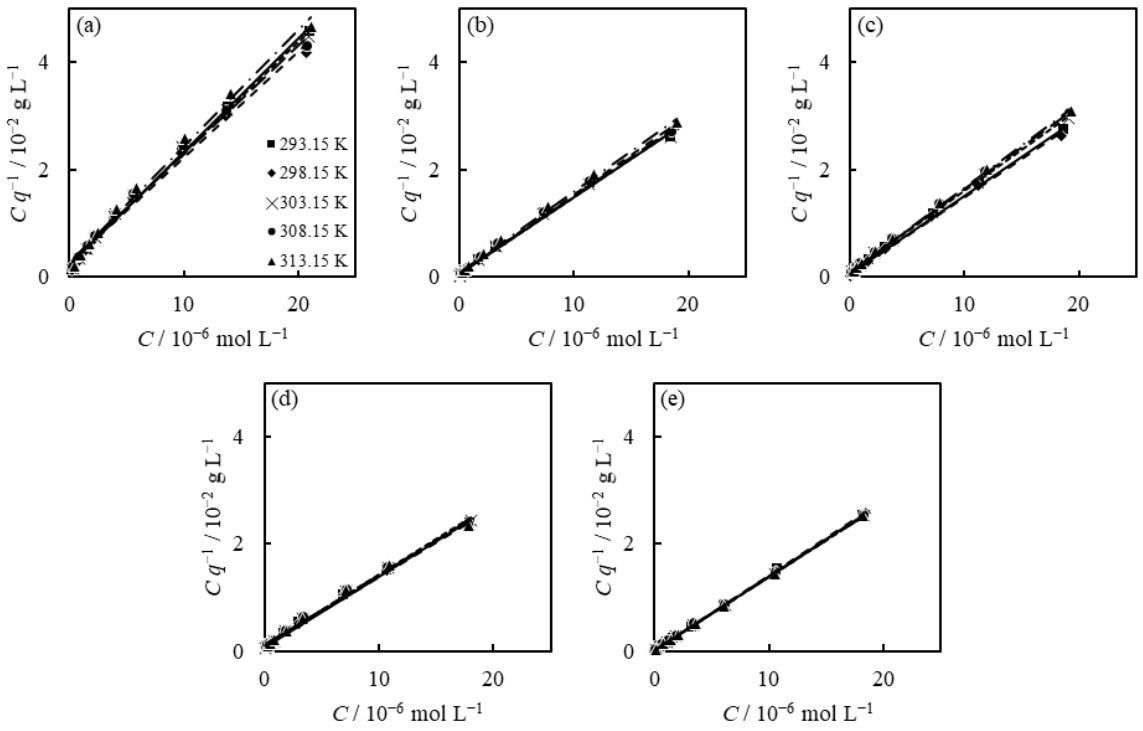

Figure 2.3. Langmuir isotherms for the adsorption of acridinium derivatives (perchlorate) on Sap1.2 at each temperature: (a) Acr^+, (b) $PhAcr^+$, (c) $DMPhAcr^+$, (d) $MesAcr^+$, and (e) $MesPhAcr^+$.

cationic molecules on the clay surface by the Langmuir plot because mono-cationic molecules often aggregate on the clay surface.[35–37]

Δ*G* for adsorption of acridinium derivatives on the surface of Sap1.2 were negative values, indicating that the adsorption of acridinium derivatives on Sap1.2 is an exergonic reaction. Furthermore, the value of Δ*G* varied with the structure of substituents, indicating that the molecular structure influenced the adsorption mechanism.

2.3.3. Thermodynamic parameters for adsorption

For adsorption, various interactions such as electrostatic, van der Waals forces, and hydrophobic interactions could work. As shown in 1.4.2, the relationship between Δ*G*, Δ*H,* and Δ*S* is represented as Eq. (1.13). Among those interactions, it is known that Δ*H* depends on electrostatic and van der Waals forces interactions and Δ*S* depends on hydrophobic interactions.[38,39] The values of Δ*H* and Δ*S* were calculated from the slope and intercept of the van't Hoff plot. Figure 2.4 shows the van't Hoff plot, and Table 2.1 shows the values of Δ*H* and Δ*S* for adsorption of acridinium derivatives on Sap1.2.

The Δ*H* for adsorption of acridinium derivatives on the surface of Sap1.2 were negative

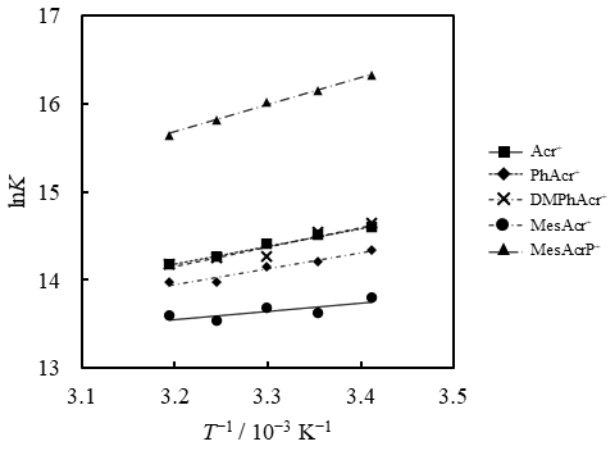

Figure 2.4. The van't Hoff plot for adsorption of acridinium derivatives on Sap1.2.

Table 2.1. Adsorption Equilibrium Constants and Maximum Adsorption Amounts for Acridinium Derivatives on Sap1.2 at Each Temperature

compound	temperature / K	K_{eq} / L mol^{-1}	q_{max} / % vs.CEC	ΔG / kJ mol^{-1}	ΔH / kJ mol^{-1}	ΔS / kJ mol^{-1} K^{-1}
Acr^+	293.15	9.86×10^5	47.3	−33.64	−7.83	0.0876
	298.15	8.29×10^5	50.6	−33.78		
	303.15	8.81×10^5	48.3	−34.50		
	308.15	7.56×10^5	49.7	−34.68		
	313.15	8.00×10^5	46.4	−35.39		
$PhAcr^+$	293.15	2.19×10^6	70.3	−35.59	−16.75	0.0644
	298.15	2.01×10^6	68.4	−35.97		
	303.15	1.81×10^6	71.2	−36.32		
	308.15	1.56×10^6	70.2	−36.53		
	313.15	1.44×10^6	66.9	−36.91		
$DMPhAcr^+$	293.15	2.30×10^6	68.9	−35.71	−18.62	0.0581
	298.15	2.06×10^6	71.0	−36.04		
	303.15	1.56×10^6	66.1	−35.94		
	308.15	1.55×10^6	64.6	−36.52		
	313.15	1.45×10^6	64.2	−36.93		
$MesAcr^+$	293.15	1.70×10^6	76.3	−34.96	−14.94	0.0681
	298.15	1.47×10^6	77.4	−35.21		
	303.15	1.40×10^6	75.6	−35.66		
	308.15	1.17×10^6	77.0	−35.80		
	313.15	1.17×10^6	77.4	−36.37		
$MesAcrPh^+$	293.15	1.24×10^7	72.6	−39.80	−26.02	0.0471
	298.15	1.05×10^7	71.9	−40.06		
	303.15	9.13×10^6	73.0	−40.40		
	308.15	7.49×10^6	73.0	−40.55		
	313.15	6.22×10^6	73.5	−40.73		

values. These results indicate that the adsorption of acridinium derivatives on Sap1.2 is an exothermic reaction. In order to discuss what factors determine the ΔH value, Figure 2.5 shows the relationships between ΔH and molecular parameters such as molecular cross-sectional area, bulkiness, charge density of N atom, and chemical hardness(η). The optimized molecular structures and the estimated energy levels of acridinium derivatives by DFT calculation are shown in Figure S2.6 and Table S2.1. The calculation method of the chemical

hardness is shown in the Supporting Information. Among them, the molecular cross-sectional area showed a strong correlation with Δ*H*. Δ*H* became more negative with the increase in the molecular cross-sectional area. Previous research has suggested that van der Waals forces depend on the molecular cross-sectional area among the interactions,[40] whereas there is no relationship between Δ*H* and the charge density of nitrogen atoms. These results suggest that van der Waals force between clay surface and adsorbates is dominant for Δ*H* of adsorption. On the other hand, the Δ*S* for adsorption of acridinium derivatives on the surface of Sap1.2 were positive values. The values of Δ*S* are generally negative in the case of gas-phase adsorption because of the decrease in the randomness of gas molecules on the solid surface.[41] However, various researches have reported that the Δ*S* of adsorption in a liquid phase is positive.[1,42,43]

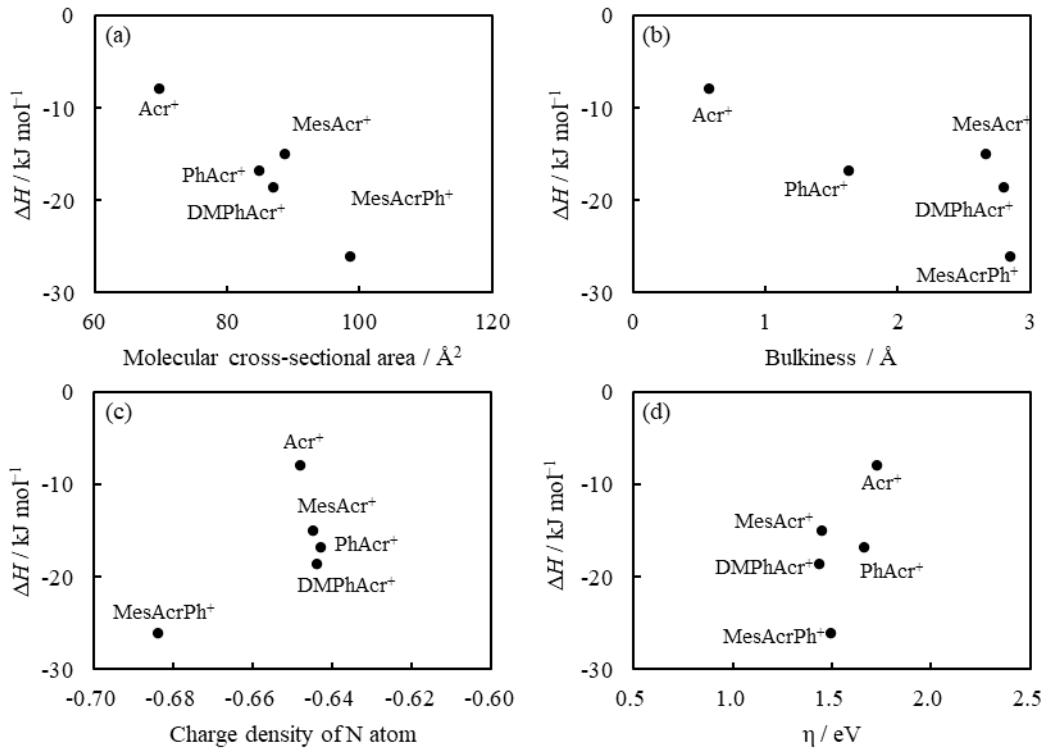

Figure 2.5. Relationships between Δ*H* with (a) molecular cross-sectional area, (b) bulkiness, (c) charge density of N atom, and (d) chemical hardness.

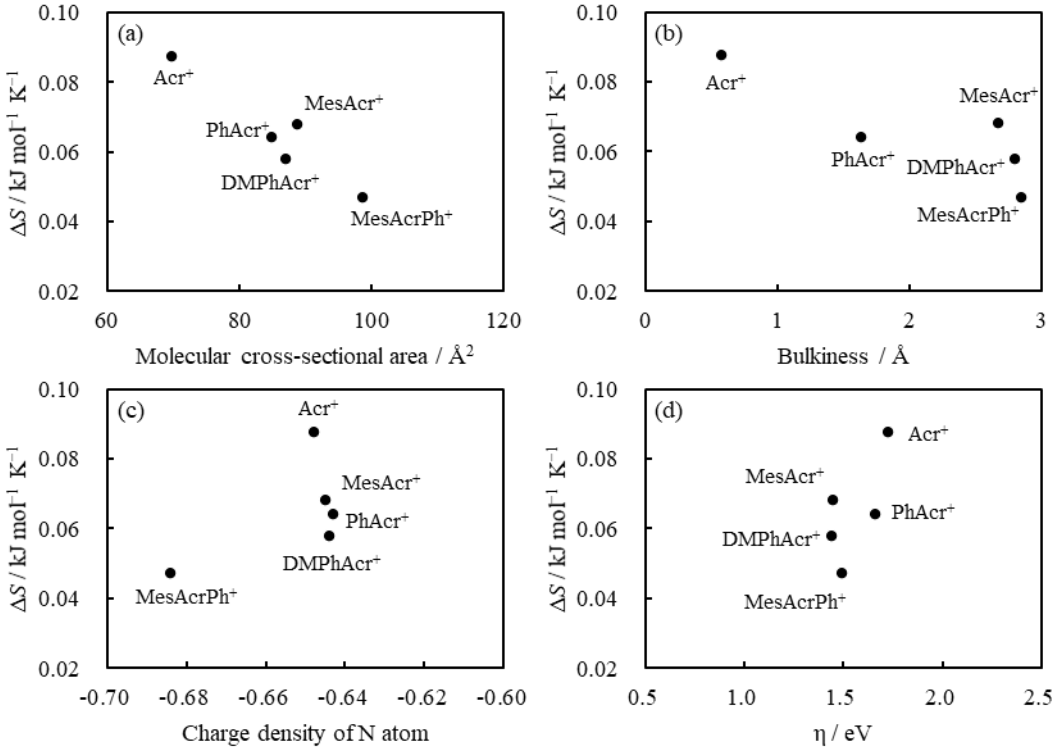

Figure 2.6. Relationships between Δ*S* with (a) molecular cross-sectional area, (b) bulkiness, (c) charge density of N atom, and (d) chemical hardness.

In the case of adsorption of acridinium derivatives on Sap1.2, the positive Δ*S* indicates the increase in the randomness in this system. It was suggested that the randomness of water molecules increased because the water molecules detached from the solid surface by adsorption of the adsorbate and the iceberg-like water molecules surrounding the adsorbate could obtain entropy.

In order to discuss what factors determine the Δ*S* value, the relationship between Δ*S* and molecular parameters such as molecular cross-sectional area, bulkiness, charge density of N atom, and chemical hardness was examined, as shown in Figure 2.6. Among them, the molecular cross-sectional area showed a strong correlation with Δ*S* (Figure 2.6 (a)). Iceberg-like water molecules would be detached from the surface of adsorbents and adsorbates if

acridinium derivatives are adsorbed parallelly on the clay surface. Hence, ΔS should become more positive by the enlargement of the molecular cross-sectional area in such cases. However, Figure 2.6 (a) showed that the values of ΔS varied in an unfavorable direction in adsorption with the increase in the molecular cross-sectional area. Although it is not easy to interpret the behavior of ΔS, the following hypothesis can be considered.

In the case of a small molecular cross-sectional area such as Acr^+ and $PhAcr^+$, the aromatic ring of these acridinium derivatives could adsorb parallelly on the clay surface. It is known that ΔS increases by adsorption under such conditions.[6] In water, an iceberg-like solvent network should form a hydrogen bonding network on the surfaces of the complex of hydrophobic aromatic rings and clay minerals. Because there are no dangling bonds at oxygen atoms due to the sharing of oxygen atoms by two tetrahedral silicates at the clay surface, the clay surface is considered hydrophobic. It is known that talc, which has a very low charge density, is completely hydrophobic. The formation of an iceberg-like solvent network varies the ΔS of the system more negatively. In order to avoid a negative change in ΔS, the hydrophobic surfaces tend to face each other in order to decrease their total surface area facing the solvent molecules. Thus, a hydrophobic interaction derived from the entropy term plays an important role in water. Previous research has shown that the parallel orientation of the porphyrin is more stable than the tilted orientation due to hydrophobic interactions.[6] In the case of a larger molecular cross-sectional area and a large bulkiness, such as $MesAcr^+$ and $MesAcrPh^+$, the aromatic ring of these acridinium derivatives could adsorb on the clay surface with tilted orientation because of their steric effects. In such a case, the hydrophobic interaction between the aromatic ring of acridinium derivatives and the clay surface could be weakened. These interpretations are consistent with the tendency shown in Figure 2.6.

2.3.4. The effect of counter anion on adsorption

In order to investigate the effect of counter anion on ΔG, ΔH, and ΔS of adsorption, the adsorption experiments were carried out by replacing the counter anions of Acr^+ and $PhAcr^+$ with chloride from perchlorate. The UV-vis absorption spectra at each temperature are shown in Figure S2.7 and Figure S2.8. Figure 2.8 shows the Langmuir plot of Acr^+ and $PhAcr^+$ with chloride as a counter anion calculated from the absorption spectral change in Figure S2.7 and S2.8. Figure 2.8 shows the van't Hoff plot for Acr^+ and $PhAcr^+$ with perchlorate and chloride as counter anions. The obtained values of K_{eq}, q_{max}, ΔG, ΔH, and ΔS from the van't Hoff plot are shown in Table 2.2.

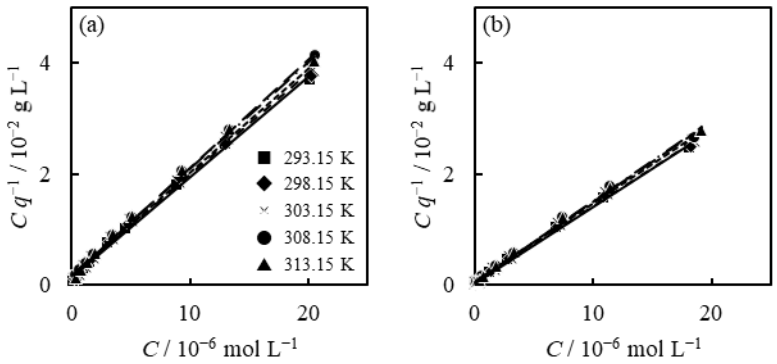

Figure 2.8. Langmuir isotherms for the adsorption of acridinium derivatives (perchlorate) on Sap1.2 at each temperature: (a) Acr^+ Cl^- and (b) $PhAcr^+Cl^-$.

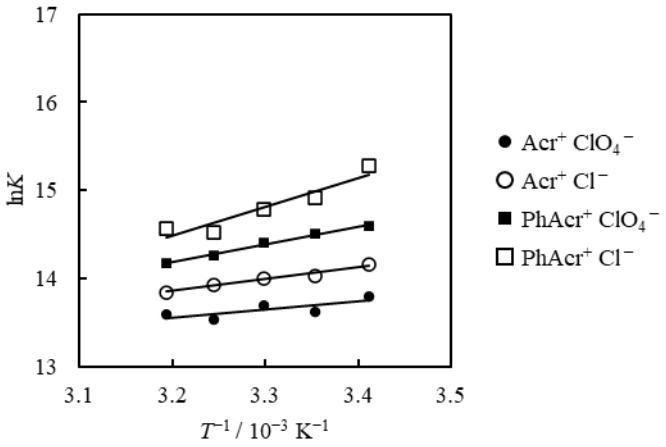

Figure 2.8. van't Hoff plot for adsorption of acridinium derivatives on Sap1.2.

Table 2.2. Adsorption Equilibrium Constants and Maximum Adsorption Amounts for Acridinium Derivatives on Sap1.2 at Each Temperature

compound	temperature / K	K_{eq} / L mol^{-1}	q_{max} / % vs.CEC	ΔG / kJ mol^{-1}	ΔH / kJ mol^{-1}	ΔS / kJ mol^{-1} K^{-1}
$Acr^+ ClO_4^-$	293.15	9.86×10^5	47.3	−33.64	−7.83	0.0876
	298.15	8.29×10^5	50.6	−33.78		
	303.15	8.81×10^5	48.3	−34.50		
	308.15	7.56×10^5	49.7	−34.68		
	313.15	8.00×10^5	46.4	−35.39		
$Acr^+ Cl^-$	293.15	1.42×10^6	55.2	−34.53	−11.30	0.0790
	298.15	1.24×10^6	54.7	−34.77		
	303.15	1.21×10^6	53.8	−35.29		
	308.15	1.12×10^6	51.5	−35.70		
	313.15	1.03×10^6	52.5	−36.04		
$PhAcr^+ ClO_4^-$	293.15	2.19×10^6	70.3	−35.59	−16.75	0.0644
	298.15	2.01×10^6	68.4	−35.97		
	303.15	1.81×10^6	71.2	−36.32		
	308.15	1.56×10^6	70.2	−36.53		
	313.15	1.44×10^6	66.9	−36.91		
$PhAcr^+ Cl^-$	293.15	4.29×10^6	73.0	−37.22	−27.58	0.0321
	298.15	3.02×10^6	72.6	−36.98		
	303.15	2.64×10^6	70.9	−37.27		
	308.15	2.04×10^6	69.7	−37.23		
	313.15	2.12×10^6	69/1	−37.93		

The ΔG of Acr^+ and $PhAcr^+$ with chloride became more negative than those with perchlorate, indicating that the adsorption becomes more exergonic by replacing the counter anion of acridinium derivatives from perchlorate to chloride. The change in the negative direction of ΔH and ΔS indicates that the contribution of the enthalpy term on adsorption increased. Since the dissociation of ionic molecules relates to the ΔH, the values of ΔH of dissociation become more negative with a decrease in the counter ion diameter.[44] In the present study, ΔH became more negative when the counter anion of acridinium derivatives was exchanged from perchlorate to chloride, which ionic diameter was smaller. It suggests that the counter anion dissociation was reflected in the ΔH of adsorption. Moreover, the

dissociation of counter ion causes increasing the number of hydrated water molecules to the dissociated counter ion. It is presumed that the contribution of the entropy term was reduced due to an increase in hydrated water molecules.

2.4. Conclusion

The adsorption behavior of mono-cationic acridinium derivatives on Sap1.2 was expressed by a two-components equilibrium system of adsorbed and non-adsorbed components, indicating that acridinium derivatives adsorb on Sap1.2 without aggregation. The adsorption equilibrium constants were determined by analyzing Langmuir adsorption isotherm. The thermodynamic parameters ΔG, ΔH, and ΔS were calculated from the van't Hoff plot using the adsorption equilibrium constants. ΔG (at 298.15 K), ΔH, and ΔS of adsorption of acridinium derivatives on the Sap1.2 were calculated to be −33.8 to −40.0 kJ mol^{-1}, −7.82 to −26.0 kJ $mol^{-1,}$ and 0.047 to 0.088 kJ mol^{-1} K^{-1}, respectively. The adsorption of acridinium derivatives on Sap1.2 was an exothermic reaction because the value of ΔH was negative for all derivatives. It was found that both van der Waals interaction and hydrophobic interaction contributed to the adsorption of mono-cationic acridinium derivatives on Sap1.2 because the value of ΔH was negative and the value of ΔS was positive. The ΔH and ΔS showed good correlations with the molecular cross-sectional area of acridinium derivatives. Moreover, ΔG and ΔH of Acr^+ and $PhAcr^+$ with chloride became more negative than those with perchlorate. The more negative ΔG due to replacing the counter anion to chloride suggests that acridinium derivatives with chloride have a higher affinity on the clay surface than the perchlorate type. The more negative ΔH suggests that the contribution of the enthalpy term increased when a higher dissociable ion, such as chloride ion, was counter ion of the adsorbate.

2.5. Supporting information

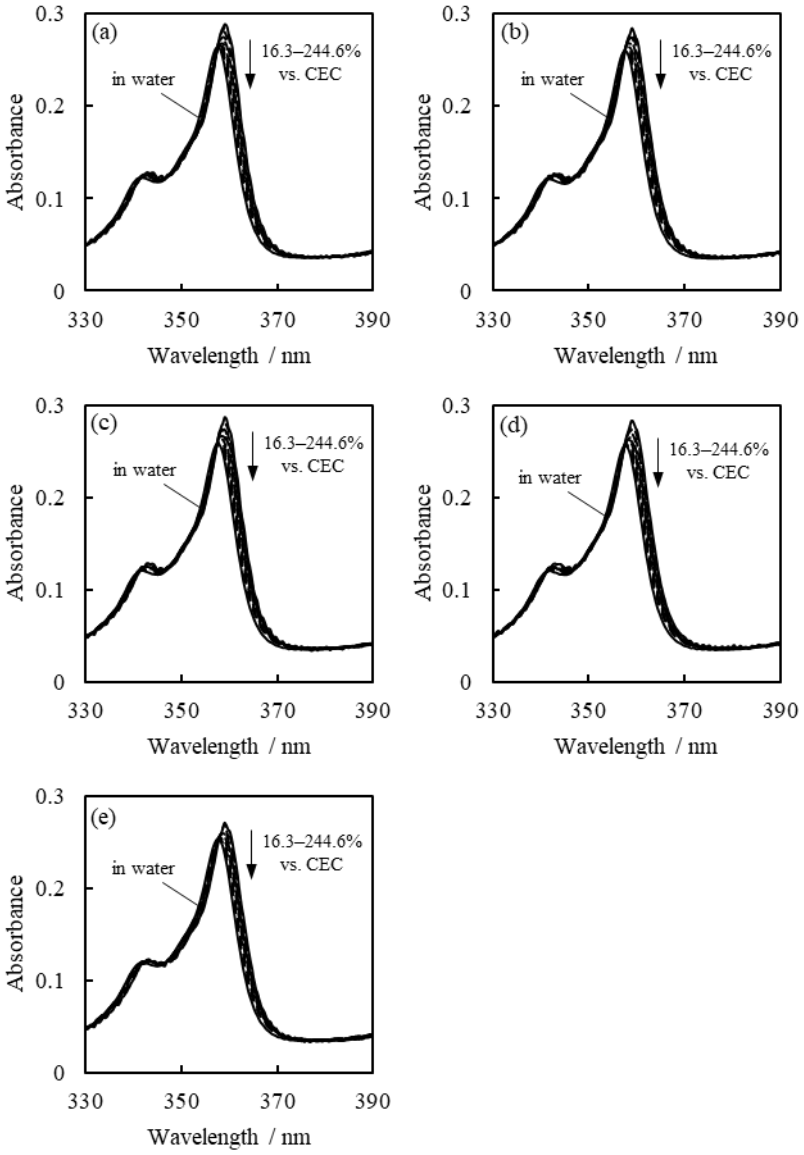

Figure S2.1. UV-vis absorption spectra of $Acr^+ ClO_4^-$ with and without Sap1.2 in water. The loading levels of $Acr^+ ClO_4^-$ were 16.3, 24.5, 32.6, 40.8 48.9, 65.2, 81.5, 122.3, 163.0, 244.6% vs. CEC: (a)293.15 K, (b)298.15 K, (c)303.15 K, (d)308.15 K, (e)313.15 K. The spectra were corrected with each acridinium derivatives concentration.

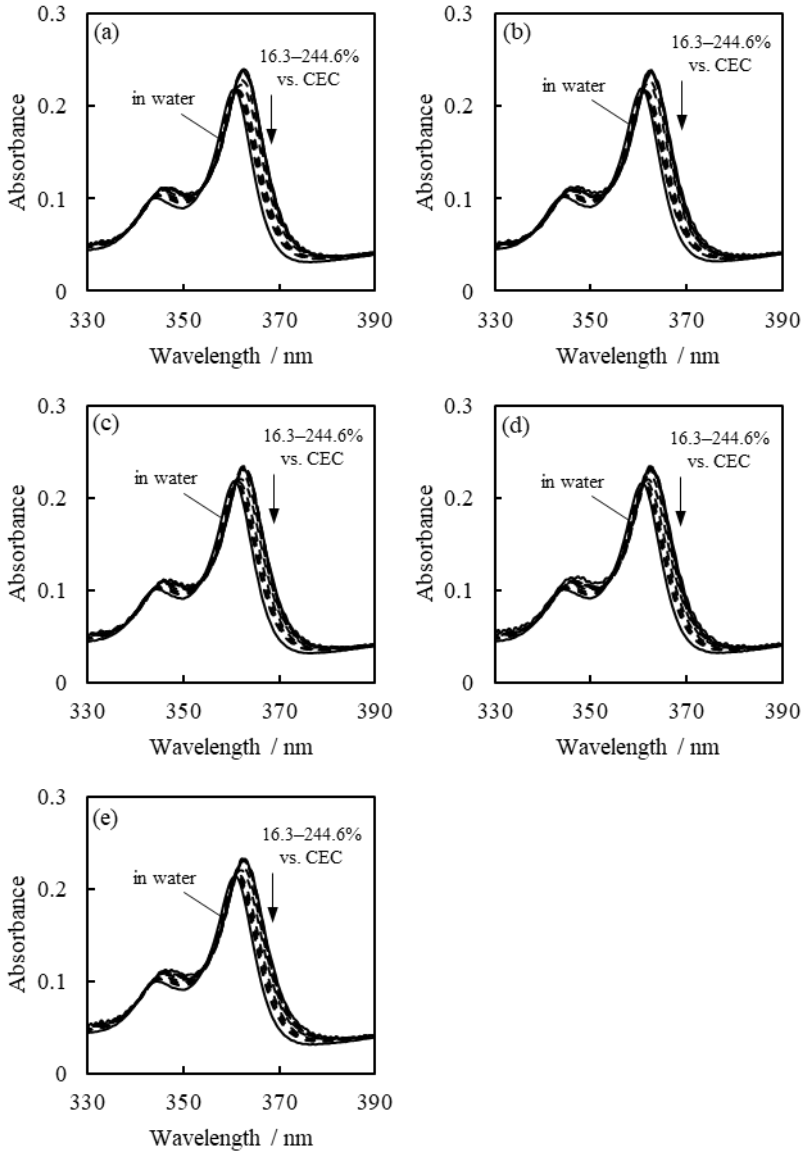

Figure S2.2. UV-vis absorption spectra of $PhAcr^{+}\ ClO_4^{-}$ with and without Sap1.2 in water. The loading levels of $PhAcr^{+}\ ClO_4^{-}$ were 16.3, 24.5, 32.6, 40.8 48.9, 65.2, 81.5, 122.3, 163.0, 244.6% vs. CEC: (a)293.15 K, (b)298.15 K, (c)303.15 K, (d)308.15 K, (e)313.15 K. The spectra were corrected with each acridinium derivatives concentration.

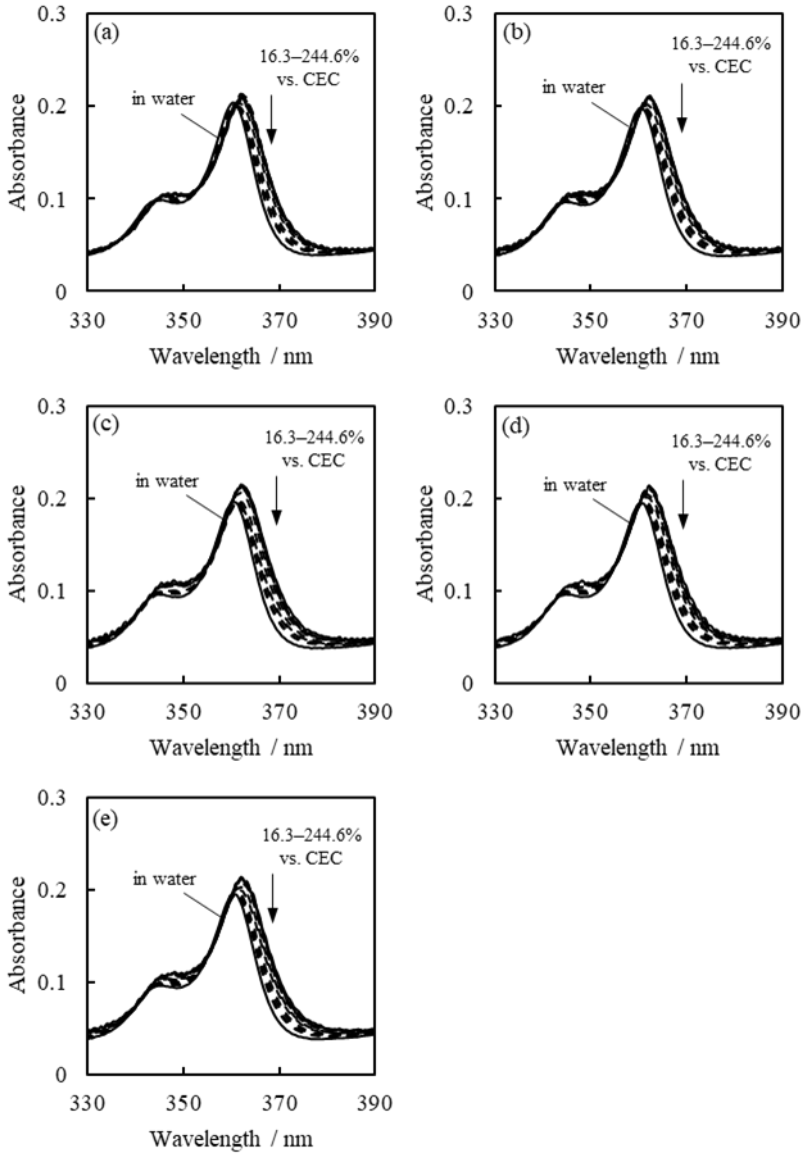

Figure S2.3. UV-vis absorption spectra of $DMPhAcr^{+}\,ClO_4^{-}$ with and without Sap1.2 in water. The loading levels of $DMPhAcr^{+}\,ClO_4^{-}$ were 16.3, 24.5, 32.6, 40.8 48.9, 65.2, 81.5, 122.3, 163.0, 244.6% vs. CEC: (a)293.15 K, (b)298.15 K, (c)303.15 K, (d)308.15 K, (e)313.15 K. The spectra were corrected with each acridinium derivatives concentration.

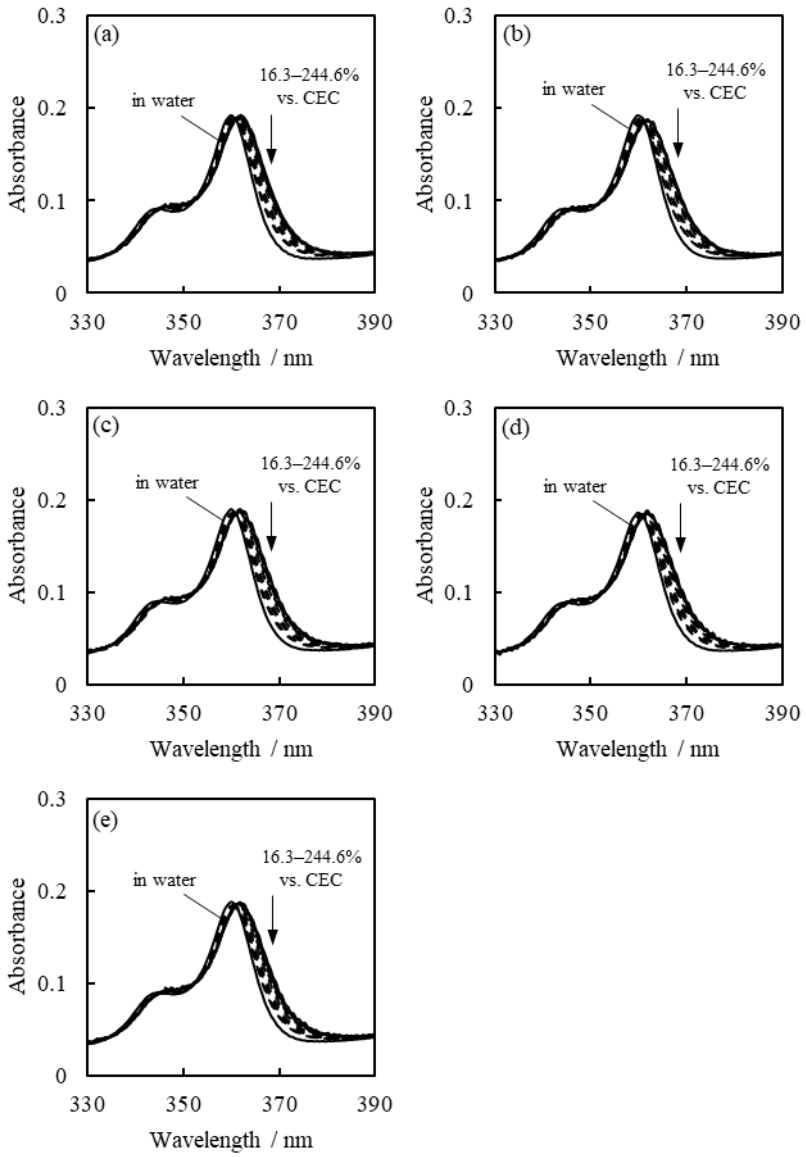

Figure S2.4. UV-vis absorption spectra of $MesAcr^+ ClO_4^-$ with and without Sap1.2 in water. The loading levels of $MesAcr^+ ClO_4^-$ were 16.3, 24.5, 32.6, 40.8 48.9, 65.2, 81.5, 122.3, 163.0, 244.6% vs. CEC: (a)293.15 K, (b)298.15 K, (c)303.15 K, (d)308.15 K, (e)313.15 K. The spectra were corrected with each acridinium derivatives concentration.

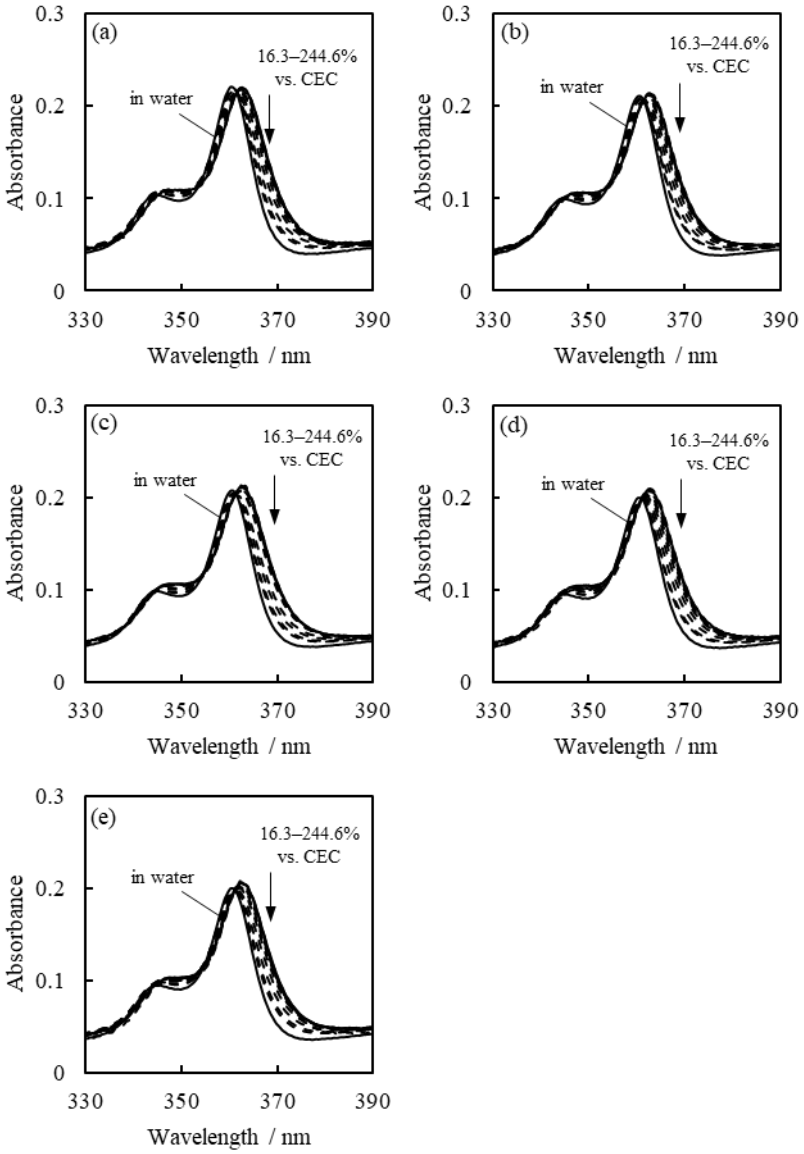

Figure S2.5. UV-vis absorption spectra of $MesAcrPh^+ ClO_4^-$ with and without Sap1.2 in water. The loading levels of $MesAcrPh^+ ClO_4^-$ were 16.3, 24.5, 32.6, 40.8 48.9, 65.2, 81.5, 122.3, 163.0, 244.6% vs. CEC: (a)293.15 K, (b)298.15 K, (c)303.15 K, (d)308.15 K, (e)313.15 K. The spectra were corrected with each acridinium derivatives concentration.

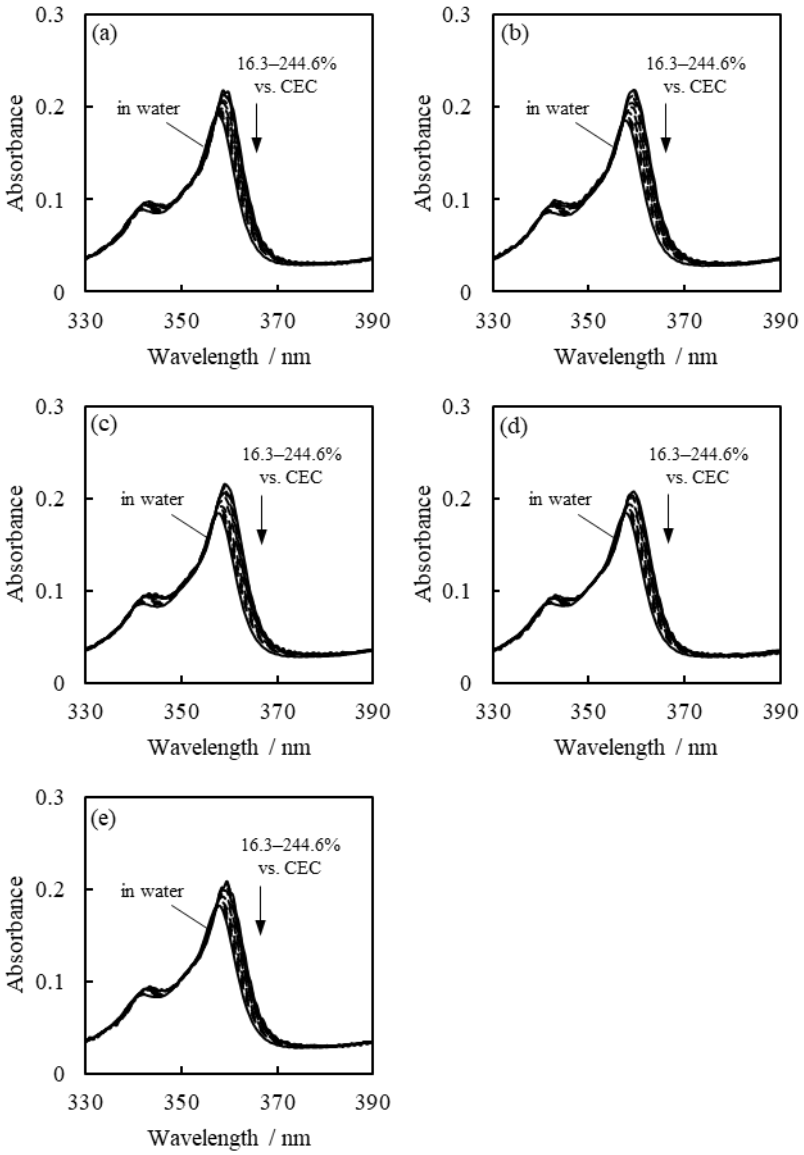

Figure S2.6. UV-vis absorption spectra of $Acr^+ Cl^-$ with and without Sap1.2 in water. The loading levels of $Acr^+ Cl^-$ were 16.3, 24.5, 32.6, 40.8 48.9, 65.2, 81.5, 122.3, 163.0, 244.6% vs. CEC: (a)293.15 K, (b)298.15 K, (c)303.15 K, (d)308.15 K, (e)313.15 K. The spectra were corrected with each acridinium derivatives concentration.

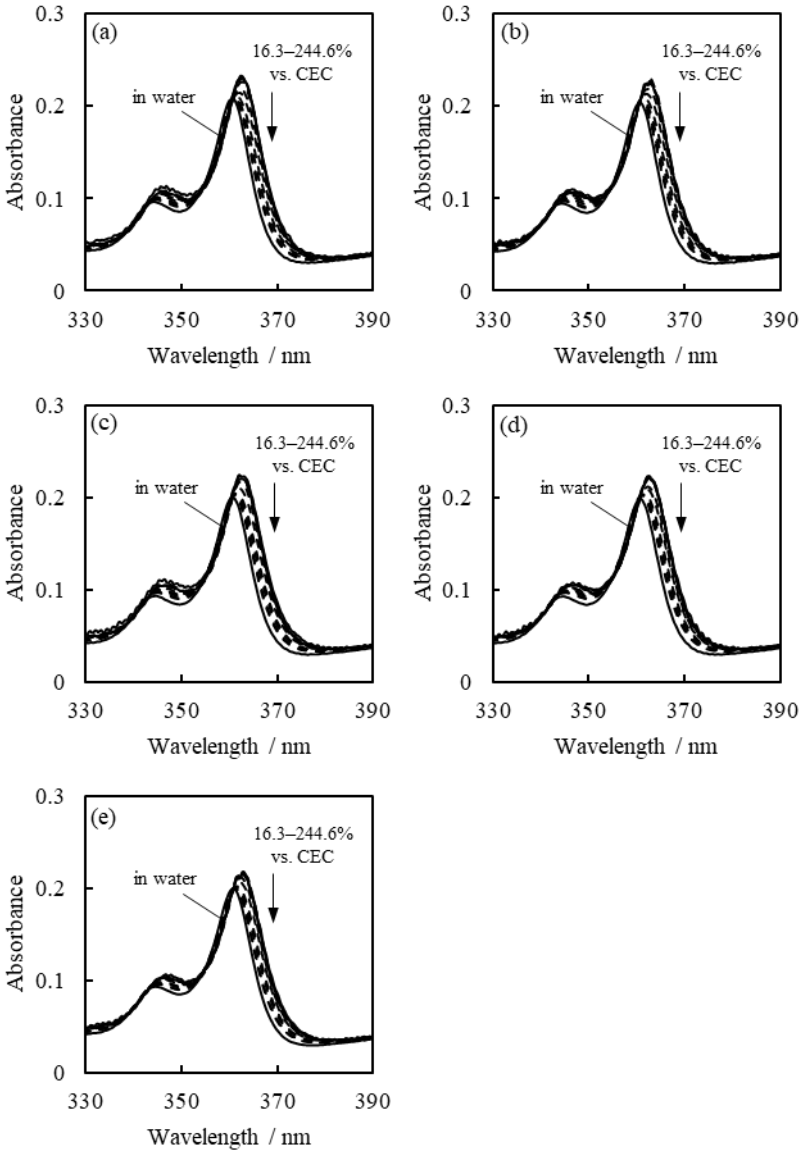

Figure S2.7. UV-vis absorption spectra of $PhAcr^{+}\,Cl^{-}$ with and without Sap1.2 in water. The loading levels of $PhAcr^{+}\,Cl^{-}$ were 16.3, 24.5, 32.6, 40.8 48.9, 65.2, 81.5, 122.3, 163.0, 244.6% vs. CEC: (a)293.15 K, (b)298.15 K, (c)303.15 K, (d)308.15 K, (e)313.15 K. The spectra were corrected with each acridinium derivatives concentration.

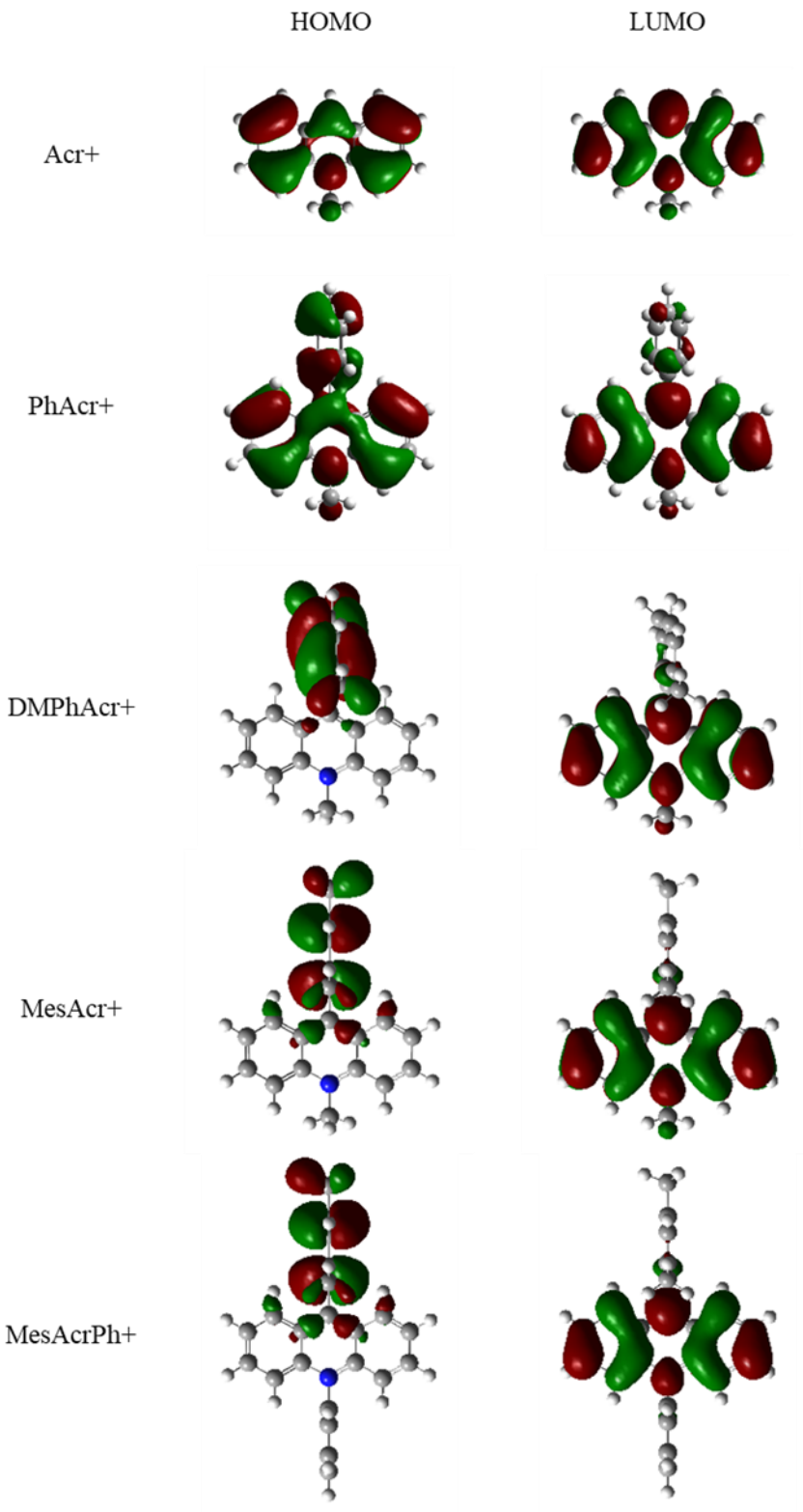

Figure S2.8. Optimized molecular structures of acridinium derivatives obtained from DFT calculations performed at B3LYP/6-31G* level using Gaussian09 package.

Calculation method of chemical hardness

Pearson *et al.* have proposed that the chemical hardness is calculated by the electron affinity and the ionization energy by the expansion of the Hard and Soft Acids and Bases (HSAB) theory.[45] The chemical hardness is used as a fundamental tool to understand the affinity on the solid surface since it is defined as hard acids having a higher affinity with hard bases, and soft acids having a higher affinity with soft bases.[46,47] The chemical hardness is calculated by equation (2.1) using molecular energy levels of HOMO and LUMO.[45]

$$\eta = \frac{1}{2}(\varepsilon_{LUMO} - \varepsilon_{HOMO}) \quad (2.1)$$

Table S2.1. Estimated Energy Levels of HOMO and LUMO for Acridinium Derivatives and Chemical Hardness

compound	ε_{HOMO} / eV	ε_{LUMO} / eV	η / eV
Acr^+	−10.119	−6.671	1.724
$PhAcr^+$	−9.678	−6.359	1.659
$DMPhAcr^+$	−9.201	−6.311	1.445
$MesAcr^+$	−9.095	−6.110	1.493
$MesAcrPh^+$	−9.196	−6.322	1.437

2.6. References

1. Tahir, S. S.; Rauf, N. Removal of a Cationic Dye from Aqueous Solutions by Adsorption onto Bentonite Clay. *Chemosphere* **2006**, *63*, 1842–1848.

2. Moet, A. S.; Akelah, A. Polymer-clay Nanocomposites: Polystyrene Grafted onto Montmorillonite Interlayers. *Mater. Lett.* **1993**, *18*, 97–102.

3. Weimer, M. W.; Chen, H.; Giannelis, E. P.; Sogah, D. Y. Direct Synthesis of Dispersed Nanocomposites by in Situ Living Free Radical Polymerization Using a Silicate-Anchored Initiator. *J. Am. Chem. Soc.* **1999**, *121*, 1615–1616.

4. Takagi, S.; Eguchi, M.; Inoue, H. Photochemical Electron Transfer Reactions in Clay-porphyrin Complexes. *Clay Sci.* **2006**, *12*, 82–87.

5. Ishida, Y.; Shimada, T.; Masui, D.; Tachibana, H.; Inoue, H.; Takagi, S. Efficient Excited Energy Transfer Reaction in Clay/Porphyrin Complex toward an Artificial Light-Harvesting System. *J. Am. Chem. Soc.* **2011**, *133*, 14280–14286.

6. Eguchi, M.; Shimada, T.; Tryk, D. A.; Inoue, H.; Takagi, S. Role of Hydrophobic Interaction in Controlling the Orientation of Dicationic Porphyrins on Solid Surfaces. *J. Phys. Chem. C.* **2013**, *117*, 9245–9251.

7. Tsukamoto, T.; Shimada, T.; Takagi, S. Photophysical Properties and Adsorption Behaviors of Novel Tri-Cationic Boron(III) Subporphyrin on Anionic Clay Surface. *ACS Appl. Mater. Interfaces* **2016**, *8*, 7522–7528.

8. Takagi, S.; Shimada, T.; Eguchi, M.; Yui, T.; Yoshida, H.; Tryk, D. A.; Inoue, H. High-Density Adsorption of Cationic Porphyrins on Clay Layer Surfaces without Aggregation: The Size-Matching Effect. *Langmuir* **2002**, *18*, 2265–2272.

9. Schoonheydt, R. A.; De Pauw, P.; Vliers, D.; De Schrijver, F. C. Luminescence of Tris(2,2'-bipyridine)ruthenium(II) in Aqueous Clay Minerals Suspensions. *J. Phys. Chem.* **1984**, *88*, 5113–5118.

10. Suzuki, Y.; Tenma, Y.; Nishioka, Y.; Kawamata, J. Efficient Nonlinear Optical Properties of Dyes Confined in Interlayer Nanospaces of Clay Minerals. *Chem. Asian J.* **2012**, *7*, 1170–1179.

11. Ogawa, M.; Kuroda, K. Photofunctions of Intercalation Compounds. *Chem. Rev.* **1995**, *95*, 399–438.

12. Grabolle, M.; Starke, M.; Resch-Genger, U. Highly Fluorescent Dye-Nanoclay Hybrid

Materials Made from Different Dye Classes. *Langmuir* **2016**, *32*, 3506–3513.

13. Wu, L.; Lv, G.; Liu, M.; Li, Z.; Liao, L.; Pan, C. Adjusting the Layer Charges of Host Phyllosilicates To Prevent Luminescence Quenching of Fluorescence Dyes. *J. Phys. Chem. C* **2015**, *119*, 22625–22631.

14. Bujdák, J.; Iyi, N. Molecular Aggregation of Rhodamine Dyes in Dispersions of Layered Silicates: Influence of Dye Molecular Structure and Silicate Properties. *J. Phys. Chem. B* **2006**, *110*, 2180–2186.

15. Bujdák, J.; Iyi, N. Molecular Orientation of Rhodamine Dyes on Surfaces of Layered Silicates. *J. Phys. Chem. B* **2005**, *109*, 4608–4615.

16. Iwasaki, M.; Kita, M.; Ito, K.; Kohno, A.; Fukunishi, K. Intercalation Characteristics of 1,1'-Diethyl-2,2'-Cyanine and other Cationic Dyes in Synthetic Saponite: Orientation in the Interlayer. *Clays Clay Miner* **2000**, *48*, 329–399.

17. Elmoubarki, R.; Mahjoubi, F. Z.; Tousadi, H.; Moustadraf, J.; Abdennouri, M.; Zouhri, A.; El-Albani, A.; Barka, N. Adsorption of Textile Dyes on Raw and Decanted Moroccan Clays: Kinetics, Equilibrium and Thermodynamics. *Water Resour. Ind.* **2015**, *9*, 16–29.

18. Eren, E.; Afsin, B. Investigation of a Basic Dye Adsorption from Aqueous Solution onto Raw and Pre-treated Bentonite Surfaces. *Dyes Pigm.* **2008**, *76*, 220–225.

19. Özcan, A.; Öncü, M. E.; Özcan, S. A. Kinetics, Isotherm and Thermodynamic Studies of Adsorption of Acid Blue 193 from Aqueous Solutions onto Natural Sepiolite. *Colloid Surf. A Physicochem. Eng. Asp.* **2006**, *277*, 90–97.

20. Javed, S. H.; Zahir, A.; Khan, A.; Afzal, S.; Mansha, M. Adsorption of Mordant Red 73 Dye on Acid Activated Bentonite: Kinetics and Thermodynamic study. *J. Mol. Liq*.

2018, *254*, 398–405.

21. Fukuzumi, S.; Kotani, H.; Ohkubo, K.; Ogo, S.; Tkachenko, N. V.; Lemmetyinen, H. Electron-Transfer State of 9-Mesityl-10-methylacridinium Ion with Much Longer Lifetime and Higher Energy Than That of the Natural Photosynthetic Reaction Center. *J. Am. Chem. Soc.* **2004**, *126*, 1600–1601.

22. Joshi-Pangu, A.; Lévesque, F.; Roth, H. G.; Oliver, S. F.; Campeau, L.; Nicewicz, D.; DiRocco, D. A. Acridinium-Based Photocatalysts: A Sustainable Option in Photoredox Catalysis. *J. Org. Chem.* **2016**, *81*, 7244–7249.

23. Gini, A.; Rigotti, T.; Pérez-Ruiz, R.; Uygur, M.; Mas-Ballesté, R.; Corral, I.; Martínez-Fernández, L.; de la Peña O'Shea, V. A.; Mancheño, O. G.; Alemán, J. Mesityl or Imide Acridinium Photocatalysts: Accessible Versus Inaccessible Charge-Transfer States in Photoredox Catalysis. *ChemPhotoChem* **2019**, *3*, 609–612.

24. Fukuzumi, S.; Doi, K.; Itoh, A.; Ohkubo, K.; Yamada, Y.; Karlin, K. D. Formation of a Long-Lived Electron-Transfer State in Mesoporous Silica-Alumina Composites Enhances Photocatalytic Oxygenation Reactivity. *Proc. Natl. Acad. Sci. U.S.A.* **2012**, *109*, 15572–15577.

25. Fukuzumi, S.; Itoh, A.; Suenobu, T.; Ohkubo, K. Formation of the Long-Lived Charge-Separated State of the 9-Mesityl-10-methylacridinium Cation Incorporated into Mesoporous Aluminosilicate at High Temperatures. *J. Phys. Chem. C* **2014**, *118*, 24188–24196.

26. Mizoshita, N.; Yamanaka, K.; Shimada, T.; Tani, T.; Inagaki, S. Mesostructured Organosilica with a 9-Mesityl-10-methylacridnium Bridging Unit: Photoinduced Charge Separation in the Organosilica Framework. *Chem. Commun.* **2010**, *46*, 9235–

9237.

27. Traina, S. J.; Onken, B. M. Cosorption of Aromatic N-heterocycles and Pyrene by Smectites in Aqueous Solutions. *J. Contam. Hydrol.* **1991**, *7*, 237–259.

28. Teng, Y.; Chang, I.; Wang, C. M. Direct Evidence of Clay-Mediated Charge Transfer. *J. Phys. Chem. B* **1997**, *101*, 10386–10389.

29. Egawa, T.; Watanabe, H.; Fujimura, T.; Ishida, Y.; Yamato, M.; Masui, D.; Shimada, T.; Tachibana, H.; Yoshida, H.; Inoue, H.; Takagi, S. Novel Methodology To Control the Adsorption Structure of Cationic Porphyrins on the Clay Surface Using the "Size-Matching Rule." *Langmuir* **2011**, *27*, 10722–10729.

30. Takagi, S.; Tryk, D. A.; Inoue, H. Photochemical Energy Transfer of Cationic Porphyrin Complexes on Clay Surface. *J. Phys. Chem. B* **2002**, *106*, 5455–5460.

31. Frisch, M. J.; Trucks, G. W.; Schlegel, H. B.; Scuseria, G. E.; Robb, M. A.; Cheeseman, J. R.; Scalmani, G.; Barone, V.; Mennucci, B.; Petersson, G. A.; Nakatsuji, H.; Caricato, M.; Li, X.; Hratchian, H. P.; Izmaylov, A. F.; Bloino, J.; Zheng, G.; Sonnenberg, J. L.; Hada, M.; Ehara, M.; Toyota, K.; Fukuda, R.; Hasegawa, J.; Ishida, M.; Nakajima, T.; Honda, Y.; Kitao, O.; Nakai, H.; Vreven, T.; Montgomery, J. A., Jr.; Peralta, J. E.; Ogliaro, F.; Bearpark, M.; Heyd, J. J.; Brothers, E.; Kudin, K. N.; Staroverov, V. N.; Kobayashi, R.; Normand, J.; Raghavachari, K.; Rendell, A.; Burant, J. C.; Iyengar, S. S.; Tomasi, J.; Cossi, M.; Rega, N.; Millam, J. M.; Klene, M.; Knox, J. E.; Cross, J. B.; Bakken, V.; Adamo, C.; Jaramillo, J.; Gomperts, R.; Stratmann, R. E.; Yazyev, O.; Austin, A. J.; Cammi, R.; Pomelli, C.; Ochterski, J. W.; Martin, R. L.; Morokuma, K.; Zakrzewski, V. G.; Voth, G. A.; Salvador, P.; Dannenberg, J. J.; Dapprich, S.; Daniels, A. D.; Farkas, O.; Foresman, J. B.; Ortiz, J. V.; Cioslowski, J.; Fox, D. J. *Gaussian 09*,

Revision A. 1; Gaussian, Inc.: Wallingford CT, **2009**.

32. Nakazato, R.; Shimada, T.; Ohtani, Y.; Ishida, T.; Takagi, S. Adsorption and Emission Enhancement Behavior of 4,4'-Bipyridine on Dispersed Montmorillonite Nano-Sheets Under Aqueous Conditions. *Tetrahedron Lett.* **2018**, *59*, 2459–2462.

33. Valandro, S. R.; Poli, A. L.; Correia, T. F.; Lombardo, P. C.; Schmitt, C. C. Photophysical Behavior of Isocyanine/Clay Hybrids in the Solid State. *Langmuir* **2017**, *33*, 891–899.

34. Bujdák, J.; Iyi, N.; Sasai, R. Spectral properties, Formation of Dye Molecular Aggregates, and Reactions in Rhodamine 6G/Layered Silicate Dispersions. *J. Phys. Chem. B* **2004**, *108*, 4470–4477.

35. Grauer, Z.; Grauer, G. L.; Avnir, D.; Yariv, S. Metachromasy in Clay Minerals. Sorption of Pyronin Y by Montmorillonite and Laponite. *J. Chem. Soc., Faraday Trans.* **1987**, *83*, 1685–1701.

36. López-Arbeloa, F.; Martínez-Martínez, V.; Bañuelos Prieto, J.; López-Arbeloa, I. Adsorption of Rhodamine 3B Dye on Saponite Colloidal Particles in Aqueous Suspensions. *Langmuir* **2002**, *18*, 2658–2664.

37. Iyi, N.; Sasai, R.; Fujita, T.; Deguchi, T.; Sota, T.; López-Arbeloa, F.; Kitamura, K. Orientation and Aggregation of Cationic Laser Dyes in a Fluoromica: Polarized Spectrometry Studies. *Appl. Clay Sci.* **2002**, *20*, 125–136.

38. Ullah, S.; Bustam, M. A.; Assiri, M. A.; Al-Sehemi, A. G.; Gonfa, G.; Mukhtar, A.; Abdul Kareem, F. A.; Ayoub, M.; Saqib, S.; Mellon, N. B. Synthesis and Characterization of Mesoporous MOF UMCM-1 for CO_2/CH_4 Adsorption; an Experimental, Isotherm Modeling and Thermodynamic Study. *Microporous*

Mesoporous Mater. **2020**, *294*, 109844–109848.

39. Krishna, B. S.; Murty, D. S.; Jai Prakash, B. S. Thermodynamics of Chromium (VI) Anionic Species Sorption onto Surfactant-Modifies Montmorillonite Clay. *J. Colloid Interface Sci.* **2000**, *229*, 230–236.

40. van Oss, C. J.; Absolom, D. R.; Neumann, A. W. Applications of Net Repulsive van der Waals Forces Between Different Particles, Macromolecules, or Biological Cells in Liquids. *Colloids Surf.* **1980**, *1*, 45–56.

41. Kemball, C. Entropy of Adsorption. *Advances in Catalysis* **1950**, *2*, 233–250.

42. Ghosh, D.; Bhattacharyya, K. G. Adsorption of Methylene Blue on Kaolinite. *Appl. Clay Sci.* **2002**, *20*, 295–300.

43. Bhatt, A. S.; Sakaria, P. L.; Vasudevan, M.; Pawar, R. R.; Sudheesh, N.; Bajaj, H. C.; Mody, H. M. Adsorption of an Anionic Dye from Aqueous Medium by Organoclays: Equilibrium Modeling, Kinetic and Thermodynamic Exploration. *RSC Adv.* **2012**, *2*, 8663–8671.

44. Franks, G. V.; Djerdjev, A. M.; Beattie, J. K. Absence of Specific Cation or Anion Effects at Low Salt Concentrations on the Charge at the Oil/Water Interface. *Langmuir* **2005**, *21*, 8670–8674.

45. Parr, R. G.; Pearson, R. G. Absolute Hardness: Companion Parameter to Absolute Electronegativity. *J. Am. Chem. Soc*. **1983**, *105*, 7512-7516.

46. Li, H.; Zhu, S.; Wu, P.; Pang, J.; Zhu, W.; Jiang, W.; Li, H. Tuning the Chemical Hardness of Boron Nitride Nanosheets by Doping Carbon for Enhanced Adsorption Capacity. *ACS Omega* **2017**, *2*, 5385-5394.

47. Shu, Y. J.; Chae, J. W.; Jang, H. D.; Cho, K. Role of Chemical Hardness in the

Adsorption of Hexavalent Chromium Species onto Metal Oxide Nanoparticles. *Chem. Eng. J.* **2015**, *273*, 401-405.

Chapter 3. Effect of Negative Charge Distance of Clay Minerals on Adsorption of Acridinium Derivatives on the Clay Surface

3.1. Introduction

Clay minerals are typical layered materials and have a two- or three-sheet structure of which tetrahedral sheets and octahedral sheets are stacked. The isomorphic substitution of Si^{4+} by Al^{3+} in the tetrahedral sheet or Al^{3+} by Mg^{2+} in the octahedral sheet produces negative charges on the surface of clay minerals. Clay minerals have been used for various purposes because these are ubiquitous materials with unique properties such as ion-exchangeable capacity, swelling property, and thermal stability.[1–8]

Adsorption phenomena of molecules on the clay surface have also been investigated in detail. Adsorption phenomena of molecules are kinds of host-guest systems from the perspective of supramolecular chemistry. Thermodynamic parameters, such as enthalpic change (ΔH), and entropic change (ΔS), have been widely investigated to understand the dominant interaction of molecular adsorption on clay minerals quantitatively because these are parameters that represent the driving force of molecular recognition behavior.[1,9–15] As shown in Chapter 2, we found that the molecular cross-sectional area of guest molecules correlates with thermodynamic parameters of adsorption of mono-cationic molecules on clay minerals. On the other hand, few reports systematically discuss the relationship between the structure of clay minerals as host materials and the thermodynamic parameters of adsorption. In order to systematically discuss the effect of the structure of clay minerals on the thermodynamic parameters for adsorption, it is necessary to obtain thermodynamic parameters of adsorption

using clay minerals, of which structure is arbitrarily controlled. However, it is difficult to systematically evaluate the differences in the structures of only natural clay minerals while there are many types of clay minerals in natural. Most papers studying the effect of structures of clay minerals on adsorption discuss only the differences in the type of clay minerals.[11,16–20] Quantitative discussion about structural differences of clay minerals is therefore insufficient. We synthesized saponites with different negative charge distances by adjusting the raw material ratio and reported the effect of the negative charge distances on the adsorption of cationic porphyrins.[21] However, the relationship between the negative charge distance of the clay surface and thermodynamic parameters of adsorption has not been discussed.

In this chapter, we attempted to systematically evaluate the effect of the structure of clay minerals on adsorption by examining thermodynamic parameters of adsorption of acridinium derivatives on synthetic saponites, of which negative charge distance is controlled.

3.2. Experimental section

3.2.1. Materials

Clay minerals (saponite): Sumecton SA (Sap1.2) as a synthetic saponite was purchased from Kunimine Industries Co., Ltd and was used without further purification. The synthetic saponites, named Sap1.0 and Sap1.4, were synthesized by hydrothermal synthesis according to the previous paper.[21] These synthetic saponites were analyzed with atomic force microscopy (AFM), X-ray diffraction (XRD), X-ray fluorescence (XRF), and Fourier transform infrared spectroscopy (FT-IR) as described in the previous paper.[21] The general structure and chemical formulas of synthetic saponites are shown in Figure 1.5 and Table 1.4. According to the paper, the cation-exchange capacity (CEC) values of Sap1.0, Sap1.2, and Sap1.4 were 1.32, 0.99, and

0.69 mequiv. g^{-1}, respectively.[21] Since the specific surface area of the synthetic saponite is 750 nm^2 g^{-1}, the negative charge distances of Sap1.0, Sap1.2, and Sap1.4 were calculated to be 1.04, 1.20, and 1.45 nm on the basis of a hexagonal array, respectively. The aqueous dispersion of synthetic saponites, whose particle size is 100 nm or less, is substantially transparent in the UV-visible range. The water was deionized with an ORGANO BB-5A system (PF filter ×2 + G-10 column).

9-Phenyl-10-methylacridinium perchlorate, 9-(2,5-dimethylphenyl)-10-methylacridinium perchlorate, and 9-mesityl-10-methylacridinium perchlorate were purchased from Tokyo Kasei. 10-Methylacridinium methyl sulfate and 9-mesityl-10-phenylacridinium tetrafluoroborate were purchased from Aldrich. The counter ion was exchanged to perchlorate with an ion-exchange resin (Organo, Amberlite resin IRA-400 treated with $HClO_4$).

3.2.2. Analysis

TG-DTA curves were measured with a Shimadzu DTG-60H analyzer to determine the water content of acridinium derivatives and synthetic saponites. The temperature was ramped from room temperature to 120 ℃ with a heating rate of 10 ℃/min under dry air as a purge gas

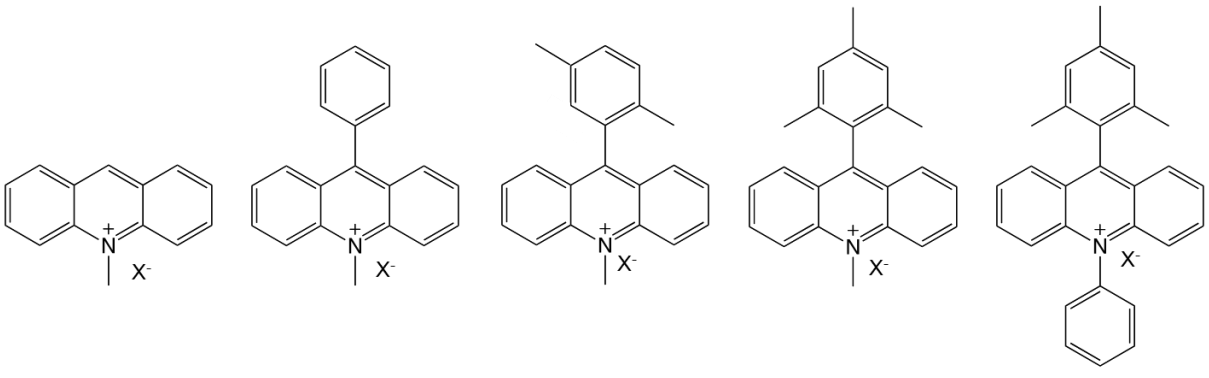

Figure 3.1. Structures of acridinium derivatives. The counter ion X^- is perchlorate

and was held for 60 min. Absorption spectra were obtained on a UV-3150 UV-vis. spectrophotometer (SHIMADZU).

3.2.3. Sample preparation

Acridinium derivatives stock solutions were prepared in a concentration range of 2.28×10^{-6} to 2.59×10^{-5} M. Synthetic saponites stock dispersions were prepared in a concentration range of 1.06×10^{-5} to 1.40×10^{-5} equiv. L^{-1}. In order to prepare acridinium derivatives-clay complexes, the above aqueous stock solutions were mixed at an arbitrary rate and were diluted water under stirring in a quartz cell (1.0 × 1.0 cm). By changing the solution concentration and the volume of stock dispersions of synthetic saponites, the adsorption density of acridinium derivatives was adjusted to be 16.3, 24.5, 32.6, 40.8, 48.9, 65.2, 81.5, 122.3, 163.0, 244.6% vs. CEC of synthetic saponites.

3.3. Result and discussion

3.3.1. Adsorption behavior of acridinium derivatives on synthetic saponites

In Chapter 2, it has been shown that acridinium derivatives showed a redshift by the adsorption on Sap1.2, and this spectral change showed isosbestic points in association with increasing loading level. Since the adsorption of acridinium derivatives on Sap1.2 was represented by the equilibrium system with two components: adsorbed and non-adsorbed components, equilibrium constants K_{eq} could be calculated by the Langmuir plot. The adsorption on Sap1.0 and Sap1.4 were also analyzed by the same method.

The adsorption behavior was examined by measuring the UV-vis absorption spectra of acridinium derivatives. The UV-vis absorption spectra of acridinium derivatives with and without synthetic saponites in water are shown in Figure 3.2 and Figure 3.3. The spectra of

each acridinium derivative with Sap1.0 and Sap1.4 at 16.3% vs. CEC showed a redshift by approximately 3 nm compared to that without Sap1.0 and Sap1.4. The redshift of maximum absorption wavelength indicates the adsorption of acridinium derivatives on the clay surface. The arbitrary observed spectra could be expressed by the spectral fitting using the spectrum in water and the spectrum of 16.3% vs. CEC. Furthermore, the absorption spectra of acridinium derivatives with and without synthetic saponites showed isosbestic points in association with increasing loading level, as shown in Figure S3.1–S3.10. This result indicated that these spectral changes were represented by the equilibrium system with two components: adsorbed and non-adsorbed components.

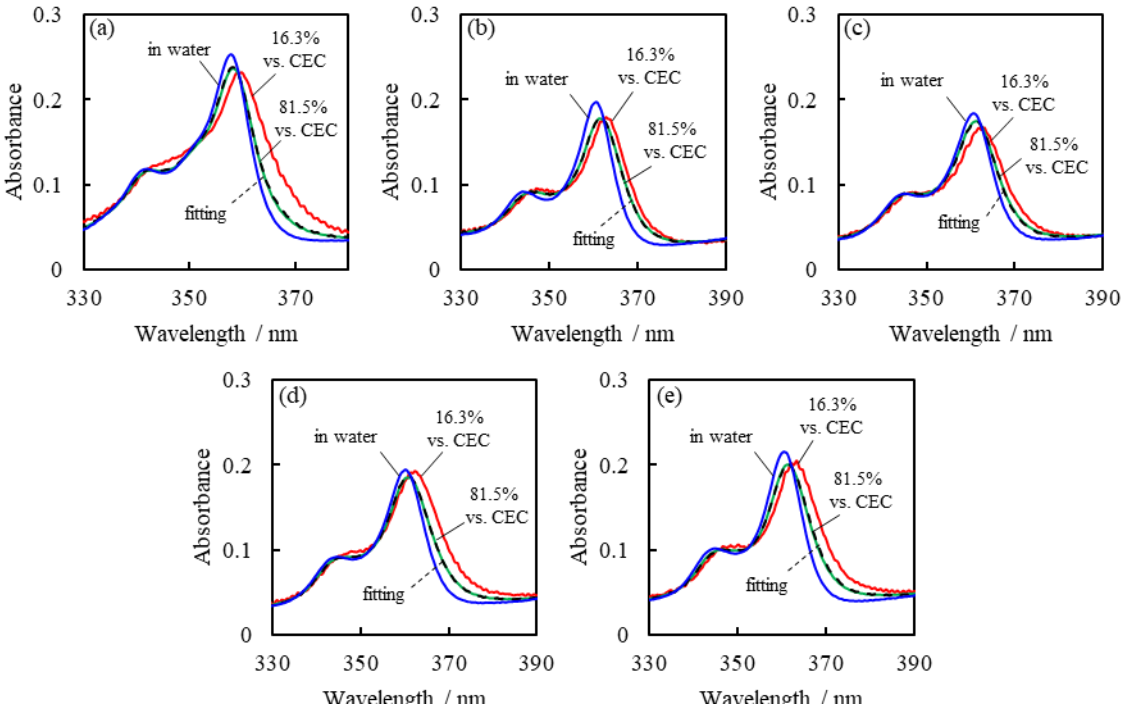

Figure 3.2. UV-vis absorption spectra of acridinium derivatives with and without Sap1.0 in water at 298.15 K. (a) Acr^+, (b) $PhAcr^+$, (c) $DMPhAcr^+$, (d) $MesAcr^+$, and (e) $MesPhAcr^+$ The spectra were corrected with each acridinium derivatives concentration.

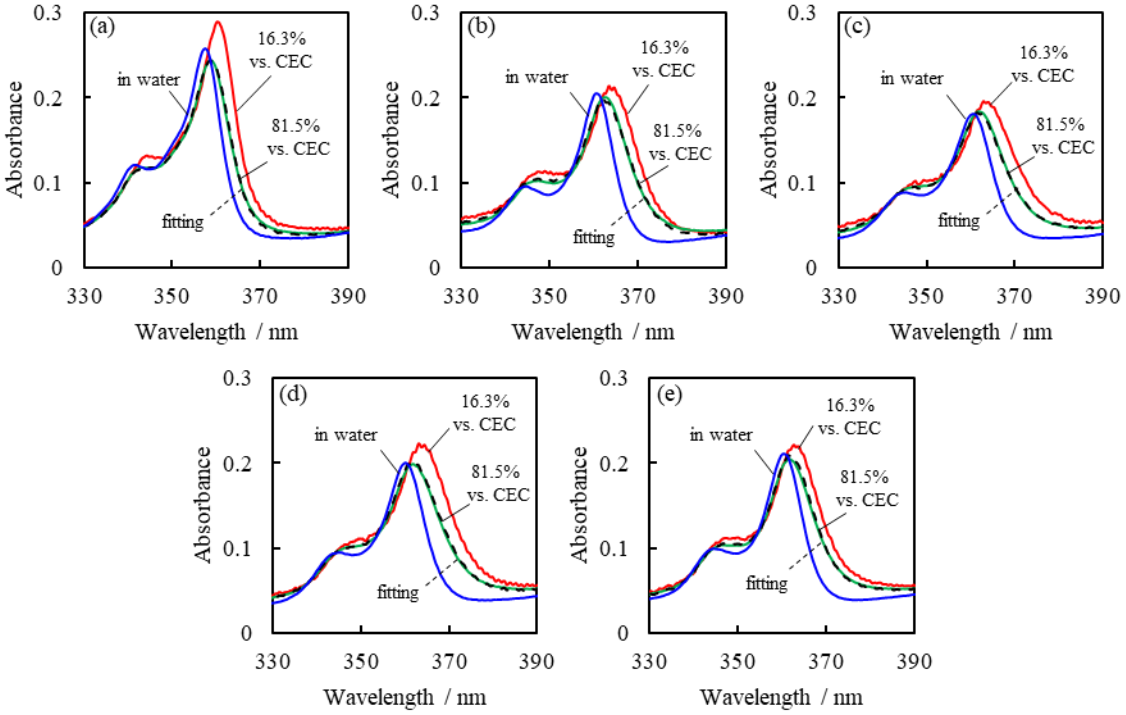

Figure 3.3. UV-vis absorption spectra of acridinium derivatives with and without Sap1.4 in water at 298.15 K. (a) Acr^+, (b) $PhAcr^+$, (c) $DMPhAcr^+$, (d) $MesAcr^+$, and (e) $MesPhAcr^+$ The spectra were corrected with each acridinium derivatives concentration.

3.3.2. Langmuir adsorption isotherms

As mentioned above, the adsorptions on both sap1.0 and sap1.4 were represented by a two-components equilibrium system of adsorbed and non-adsorbed components. Therefore, these systems satisfied the assumption of Langmuir adsorption isotherms described in Subsection 1.3.2. Hence, we calculated the adsorption amount from UV-vis absorption spectral change and analyzed the adsorption parameters using Langmuir plots. In order to obtain thermodynamic parameters from the van't Hoff plot, the adsorption equilibrium constants at 293.15–313.15 K were measured. Figure S3.1–S3.10 shows the UV-vis absorption spectra of five acridinium derivatives at each loading level at each temperature.

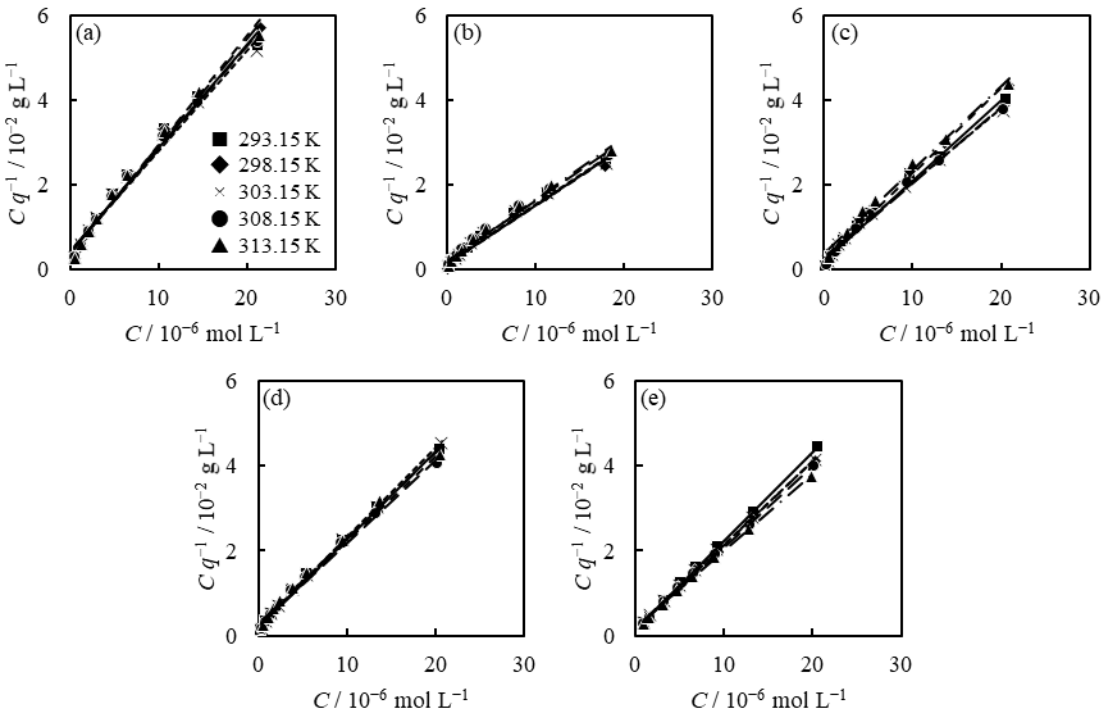

Figure 3.4. Langmuir isotherms for the adsorption of acridinium derivatives (perchlorate) on Sap1.0 at each temperature: (a) Acr^+, (b) $PhAcr^+$, (c) $DMPhAcr^+$, (d) $MesAcr^+$, and (e) $MesPhAcr^+$.

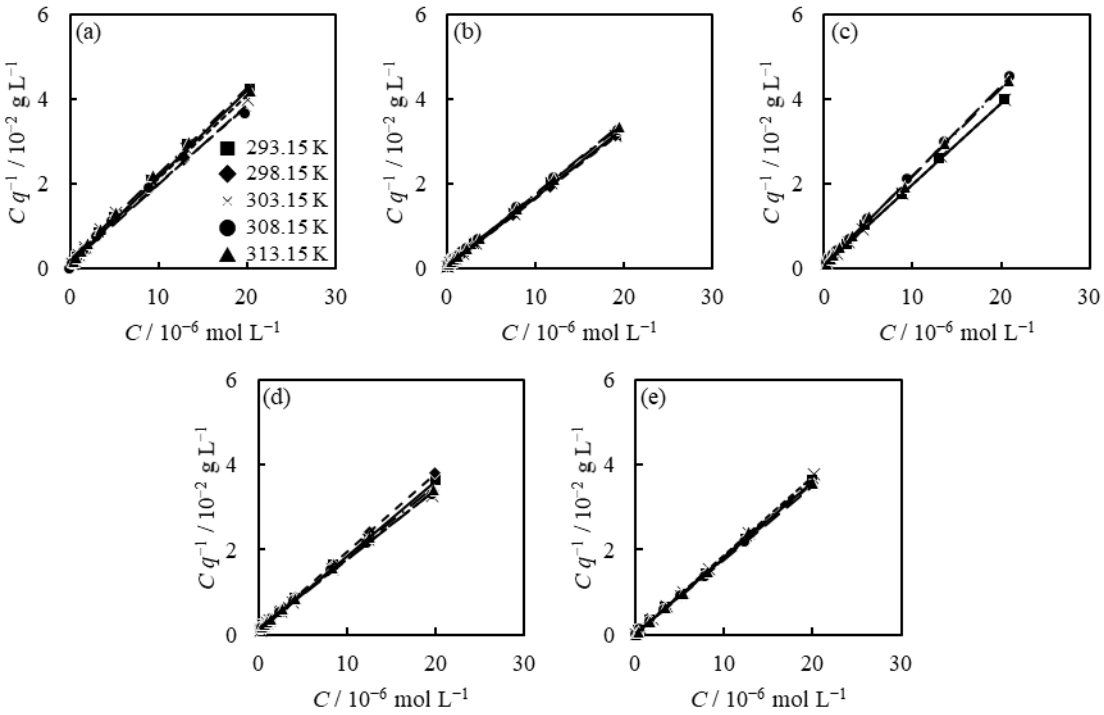

Figure 3.5. Langmuir isotherms for the adsorption of acridinium derivatives (perchlorate) on Sap1.4 at each temperature: (a) Acr^+, (b) $PhAcr^+$, (c) $DMPhAcr^+$, (d) $MesAcr^+$, and (e) $MesPhAcr^+$.

Figure 3.4 and Figure 3.5 show the Langmuir plots calculated from the absorption spectral change in Figure S3.1–S3.10. As can be seen, the Langmuir plots showed linear plots for all acridinium derivatives at each temperature. The parameters, q_{max}, $K_{eq,}$ and ΔG, calculated from these Langmuir plots are summarized in Table 3.1 and Table 3.2. ΔG for adsorption were negative values for all acridinium derivatives, indicating that the adsorption of acridinium derivatives on Sap1.0 and Sap1.4 is an exergonic reaction similar to that of Sap1.2. Moreover,

Table 3.1. Adsorption Equilibrium Constants and Maximum Adsorption Amounts for Acridinium Derivatives on Sap1.0 at Each Temperature

compound	temperature / K	K_{eq} / L mol^{-1}	q_{max} / % vs.CEC	ΔG / kJ mol^{-1}	ΔH / kJ mol^{-1}	ΔS / kJ mol^{-1} K^{-1}
Acr^+	293.15	7.06×10^5	39.0	−32.82	−6.26	0.0898
	298.15	5.32×10^5	42.4	−32.68		
	303.15	6.15×10^5	41.4	−33.59		
	308.15	5.36×10^5	41.7	−33.80		
	313.15	5.75×10^5	40.7	−34.53		
$PhAcr^+$	293.15	1.03×10^6	39.3	−33.73	−9.56	0.0824
	298.15	9.81×10^5	41.1	−34.20		
	303.15	8.30×10^5	36.3	−34.35		
	308.15	8.89×10^5	37.8	−35.09		
	313.15	7.89×10^5	35.6	−35.35		
$DMPhAcr^+$	293.15	8.38×10^5	39.9	−33.24	−14.32	0.0646
	298.15	8.17×10^5	37.5	−33.74		
	303.15	6.06×10^5	43.0	−33.56		
	308.15	7.62×10^5	42.0	−34.70		
	313.15	5.41×10^5	38.1	−34.37		
$MesAcr^+$	293.15	9.84×10^5	36.5	−33.63	−10.30	0.0798
	298.15	8.70×10^5	37.8	−33.90		
	303.15	1.05×10^6	35.7	−34.95		
	308.15	8.47×10^5	38.6	−34.97		
	313.15	7.08×10^5	37.4	−35.07		
$MesAcrPh^+$	293.15	1.85×10^6	35.7	−35.17	−13.03	0.0750
	298.15	1.50×10^6	38.0	−35.25		
	303.15	1.36×10^6	37.8	−35.60		
	308.15	1.43×10^6	39.0	−36.31		
	313.15	1.24×10^6	41.0	−36.53		

Table 3.2. Adsorption Equilibrium Constants and Maximum Adsorption Amounts for Acridinium Derivatives on Sap1.4 at Each Temperature

compound	temperature / K	K_{eq} / L mol^{-1}	q_{max} / % vs.CEC	ΔG / kJ mol^{-1}	ΔH / kJ mol^{-1}	ΔS / kJ mol^{-1} K^{-1}
Acr^+	293.15	1.86×10^6	70.3	−35.19	−11.95	0.0778
	298.15	1.12×10^6	78.9	−34.53		
	303.15	1.19×10^6	73.9	−35.25		
	308.15	1.51×10^6	77.9	−36.46		
	313.15	1.09×10^6	71.4	−36.19		
$PhAcr^+$	293.15	2.71×10^6	89.0	−36.10	−17.28	0.0644
	298.15	2.53×10^6	90.0	−36.55		
	303.15	2.34×10^6	89.5	−36.97		
	308.15	1.77×10^6	87.2	−36.86		
	313.15	1.84×10^6	86.1	−37.56		
$DMPhAcr^+$	293.15	3.16×10^6	74.4	−36.47	−19.21	0.0592
	298.15	-	-	-		
	303.15	2.71×10^6	75.3	−37.34		
	308.15	2.31×10^6	68.3	−37.53		
	313.15	1.87×10^6	70.0	−37.60		
$MesAcr^+$	293.15	1.75×10^6	83.0	−35.03	−15.34	0.0673
	298.15	1.68×10^6	79.4	−35.53		
	303.15	1.32×10^6	88.1	−35.53		
	308.15	1.37×10^6	87.1	−36.20		
	313.15	1.17×10^6	86.5	−36.38		
$MesAcrPh^+$	293.15	2.28×10^7	80.7	−41.29	−29.76	0.0384
	298.15	1.61×10^7	81.5	−41.13		
	303.15	1.17×10^7	78.1	−41.01		
	308.15	1.06×10^7	82.8	−41.44		
	313.15	1.07×10^7	80.2	−42.13		

it was found that the structure of clay minerals influenced the adsorption mechanism because the value of ΔG depended on the structure of substituents.

3.3.3. Thermodynamic parameters for adsorption

As mentioned in Chapter 2, various interactions such as electrostatic interaction, van der Waals forces, and hydrophobic interactions could work for adsorption. As shown in Subsection 1.4.1, the relationship between ΔG, ΔH, and ΔS is represented as Eq. (1.13). It is known that ΔH depends on electrostatic and van der Waals forces interactions and ΔS depends

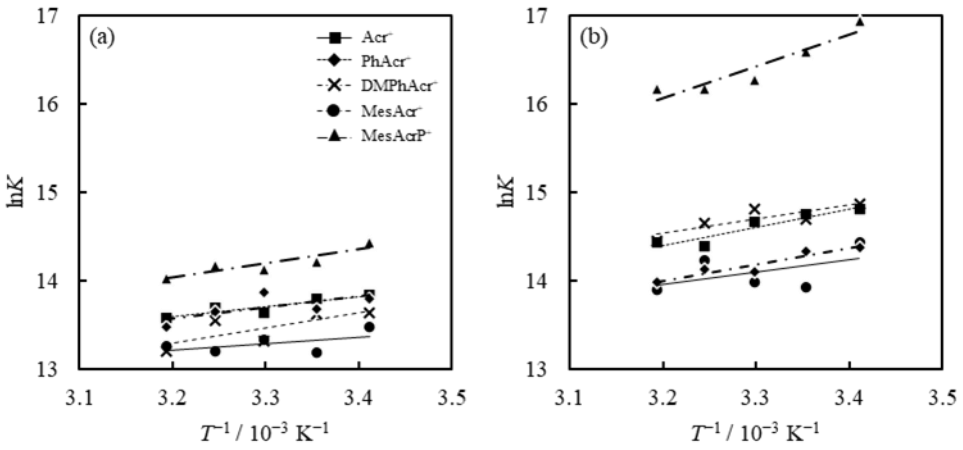

Figure 3.6. van't Hoff plot for adsorption of acridinium derivatives on (a) Sap1.0, (b) Sap1.4.

on hydrophobic interactions.[22,23] The ΔH and ΔS were calculated from the slope and intercept of the van't Hoff plot. Figure 3.6 shows the van't Hoff plots, and Table 3.1 and Table 3.2 show the values of ΔH and ΔS for adsorption of acridinium derivatives on synthetic saponite.

The magnitude of thermodynamic parameters represents the magnitude of the interactions involved in the adsorption process. It should be noted that hydrophobic interactions are apparent interactions. The adsorption equilibrium constants of acridinium derivatives on various synthetic saponites at each temperature (293.15, 298.15, 303.15, 308.15, and 313.15 K) were determined by Langmuir adsorption isotherms. Using these adsorption equilibrium constants, the values of the thermodynamic parameters ΔH and ΔS were calculated to consider how the negative charge distance on the synthetic saponites affects thermodynamic parameters, which are interactions involved in adsorption. The thermodynamic parameters for the adsorption of acridinium derivatives on Sap 1.0 and 1.4 are summarized in Table 3.1 and Table 3.2.

As can be seen from Table 3.1 and Table 3.2, the values of ΔH were negative for all combinations of acridinium derivatives and synthetic saponites, indicating that the adsorption

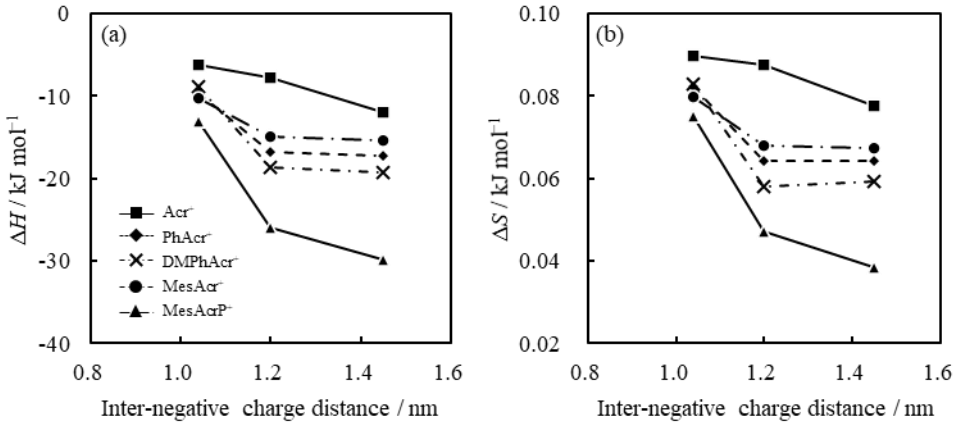

Figure 3.7. Relationships between the inter-negative charge distance with (a) Δ*H* and (a) Δ*S*.

of acridinium derivatives is an exothermic reaction regardless of the structure of synthetic saponites. In addition, the values of Δ*S* were positive for all combinations of acridinium derivatives and synthetic saponites as well. As mentioned in Chapter 2, it is suggested that the water molecules detached from the solid surface by adsorption of the adsorbate, and the iceberg-like water molecules surrounding the adsorbate obtain entropy.

Δ*H* varied in a favorable direction in adsorption, and Δ*S* varied in an unfavorable direction in adsorption as an increase in the inter-negative charge distance on synthetic saponites. The factor why Δ*H* and Δ*S* were affected by the inter-negative charge distance of the synthetic saponites could be attributed to the change in the orderliness of water molecules on the clay surface. According to previous literature, the molecular dynamics simulation shows that the water molecules on the clay surface are strongly oriented as the inter-negative charge distance on the clay surface decreases.[24,25] Another report showed that the bending vibration of water molecules shifts to the lower wavenumber side in FT-IR as the distance between negative charges on the clay surface decreases, indicating that the water molecules are strongly hydrogen-bonded.[26] According to these data, we can infer that the orientation of water

molecules on the clay surface increases as the distance between negative charges on the clay surface decreases. Based on the orientation of the water molecules, we attempted to discuss the change in ΔH and ΔS with the change in the inter-negative charge distance on the surface of synthetic saponites.

First, let us discuss the change in ΔH in the direction favorable to adsorption as the distance between negative charges increases. It is presumed that there are few water molecules remaining between the dye and the clay surface since the orderliness of water molecules on the clay surface with large negative inter-charge distances is weak. We conclude that ΔH changed in the direction favorable to adsorption as a result of the increase in van der Waals forces due to the decrease in distance between the dye and the clay surface.

Secondly, let us discuss the change ΔS in the direction unfavorable to adsorption as the distance between negative charges increases. As mentioned above, water molecules are arranged on the clay surface. When the water molecules are excluded by the dye adsorbed on the clay surface, the hydrophobic interaction works, resulting in it being reflected in ΔS. Therefore, if the excluded water molecules are weakly ordered, ΔS when water molecules on the clay surface are excluded become small. In the case of clays with a large inter-negative charge distance, the orderliness of water molecules on the clay surface is weak. As a result, since the hydrophobic interaction that acts when the acridinium derivatives adsorb on the clay surface becomes weaker, it is assumed that ΔS is unfavorable for adsorption. These results suggest that the orderliness of water molecules on the clay surface, which varies with the inter-negative charge distance on the clay surface, affects the van der Waals force and hydrophobic interaction on adsorption.

3.4. Conclusion

In order to elucidate the effect of the structure of clay minerals, the adsorption behavior of mono-cationic acridinium derivatives on synthetic saponites with various inter-charge distances was thermodynamically investigated by using Langmuir isotherm and the van't Hoff equation. The adsorption behavior of mono-cationic acridinium derivatives on Sap1.0 and Sap1.4 was represented by a two-component equilibrium system of adsorbed and non-adsorbed components, similar to Sap1.2 shown in Chapter 2. The acridinium derivatives were adsorbed onto Sap1.0 and Sap1.4 without aggregation. The adsorption equilibrium constants were determined by analyzing Langmuir adsorption isotherm. The thermodynamic parameters ΔG, ΔH, and ΔS were calculated from the van't Hoff plot using the adsorption equilibrium constants. ΔG (at 298.15 K), ΔH, and ΔS of adsorption of acridinium derivatives on the Sap1.0 were calculated to be –32.68 to −35.25 kJ mol^{-1}, −6.26 to −14.32 kJ mol^{-1}, and 0.064 to 0.082 kJ mol^{-1} K^{-1}, respectively. ΔG (at 298.15 K), ΔH, and ΔS of adsorption of acridinium derivatives on the Sap1.4 were calculated to be −34.53 to −41.13 kJ mol^{-1}, −11.95 to −29.76 kJ mol^{-1}, and 0.038 to 0.077 kJ mol^{-1} K^{-1}, respectively.

The ΔH and ΔS showed good correlations with the inter-negative charge distance on the surface of synthetic saponites. From the relationship between the inter-negative charge distance on the clay surface and the orderliness of the water molecules adsorbed on the surface in the previous literature, we conclude that the factor why ΔH and ΔS of adsorption changed with the change of inter-negative charge distance was attributed to the change in the orderliness of water molecules on the clay surface.

3.5. Supporting information

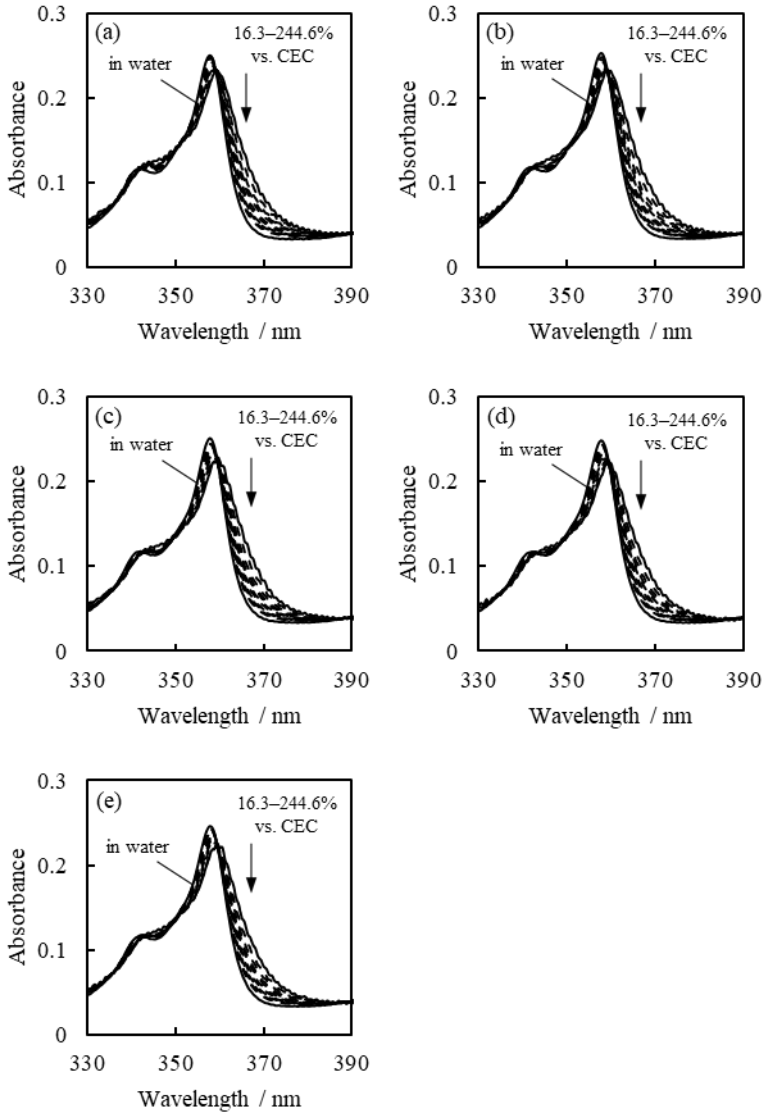

Figure S3.1. UV-vis absorption spectra of Acr^+ with and without Sap1.0 in water. The loading levels of Acr^+ were 16.3, 24.5, 32.6, 40.8 48.9, 65.2, 81.5, 122.3, 163.0, 244.6% vs. CEC: (a)293.15 K, (b)298.15 K, (c)303.15 K, (d)308.15 K, (e)313.15 K. The spectra were corrected with each acridinium derivatives concentration.

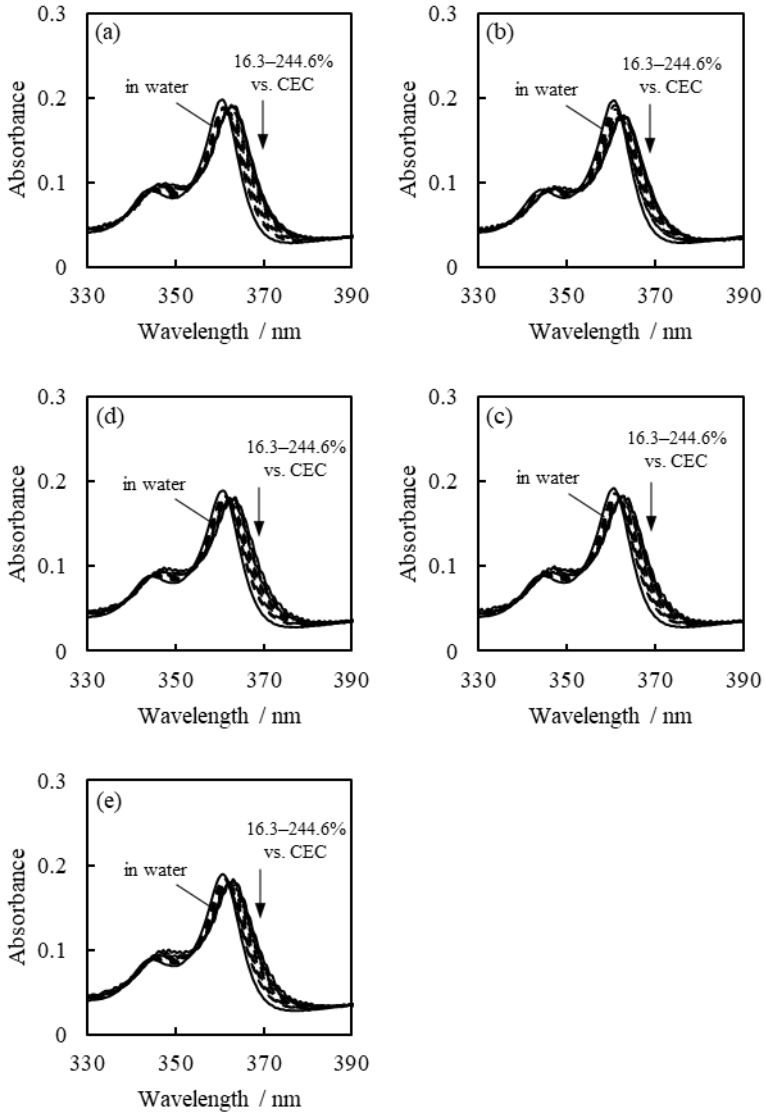

Figure S3.2. UV-vis absorption spectra of $PhAcr^+$ with and without Sap1.0 in water. The loading levels of $PhAcr^+$ were 16.3, 24.5, 32.6, 40.8 48.9, 65.2, 81.5, 122.3, 163.0, 244.6% vs. CEC: (a)293.15 K, (b)298.15 K, (c)303.15 K, (d)308.15 K, (e)313.15 K. The spectra were corrected with each acridinium derivatives concentration.

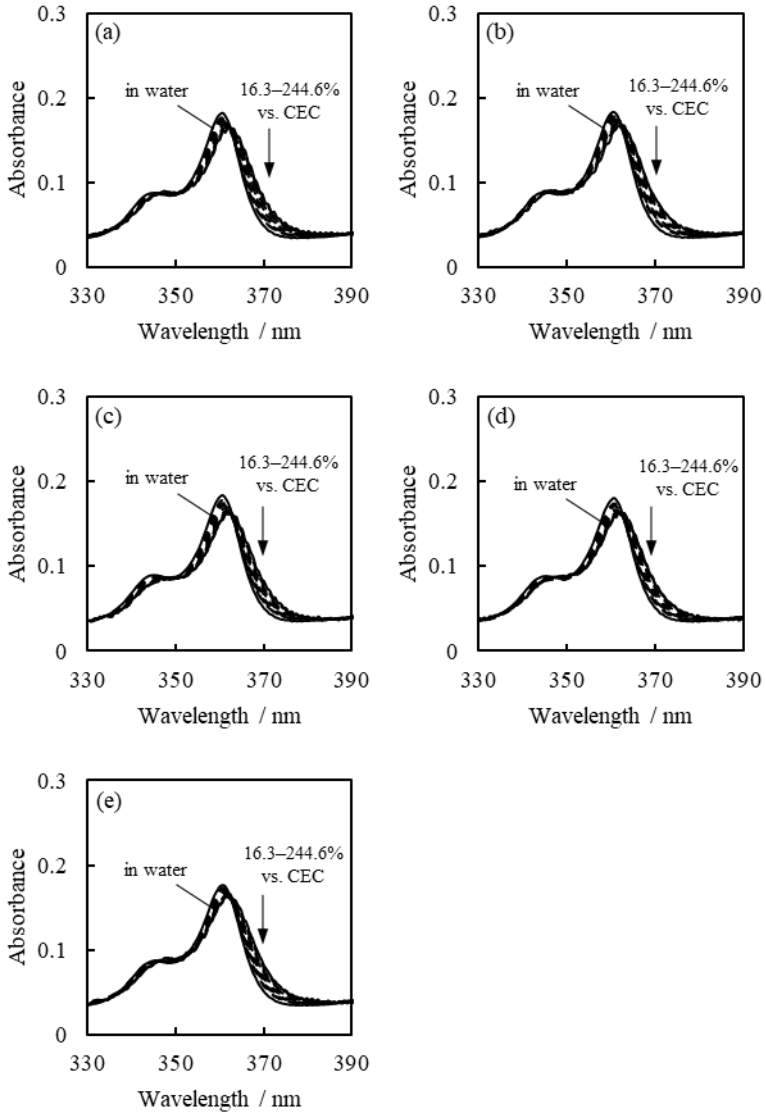

Figure S3.3. UV-vis absorption spectra of $DMPhAcr^+$ with and without Sap1.0 in water. The loading levels of $DMPhAcr^+$ were 16.3, 24.5, 32.6, 40.8 48.9, 65.2, 81.5, 122.3, 163.0, 244.6% vs. CEC: (a)293.15 K, (b)298.15 K, (c)303.15 K, (d)308.15 K, (e)313.15 K. The spectra were corrected with each acridinium derivatives concentration.

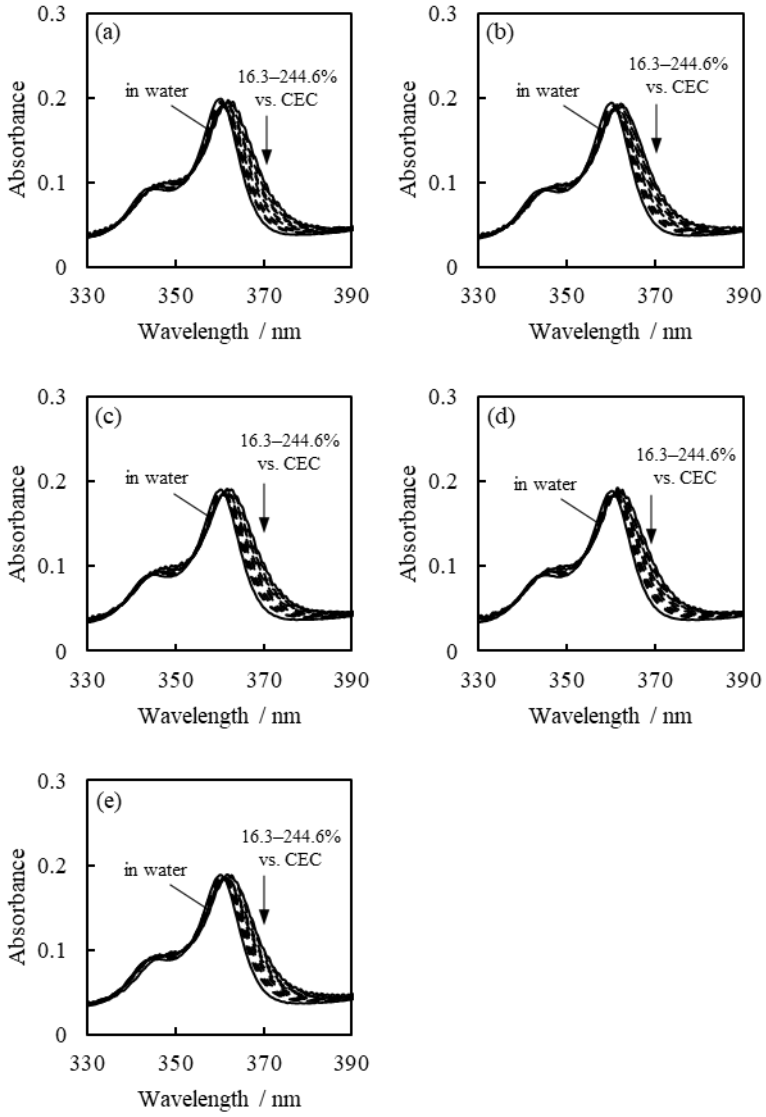

Figure S3.4. UV-vis absorption spectra of $MesAcr^+$ with and without Sap1.0 in water. The loading levels of $MesAcr^+$ were 16.3, 24.5, 32.6, 40.8 48.9, 65.2, 81.5, 122.3, 163.0, 244.6% vs. CEC: (a)293.15 K, (b)298.15 K, (c)303.15 K, (d)308.15 K, (e)313.15 K. The spectra were corrected with each acridinium derivatives concentration.

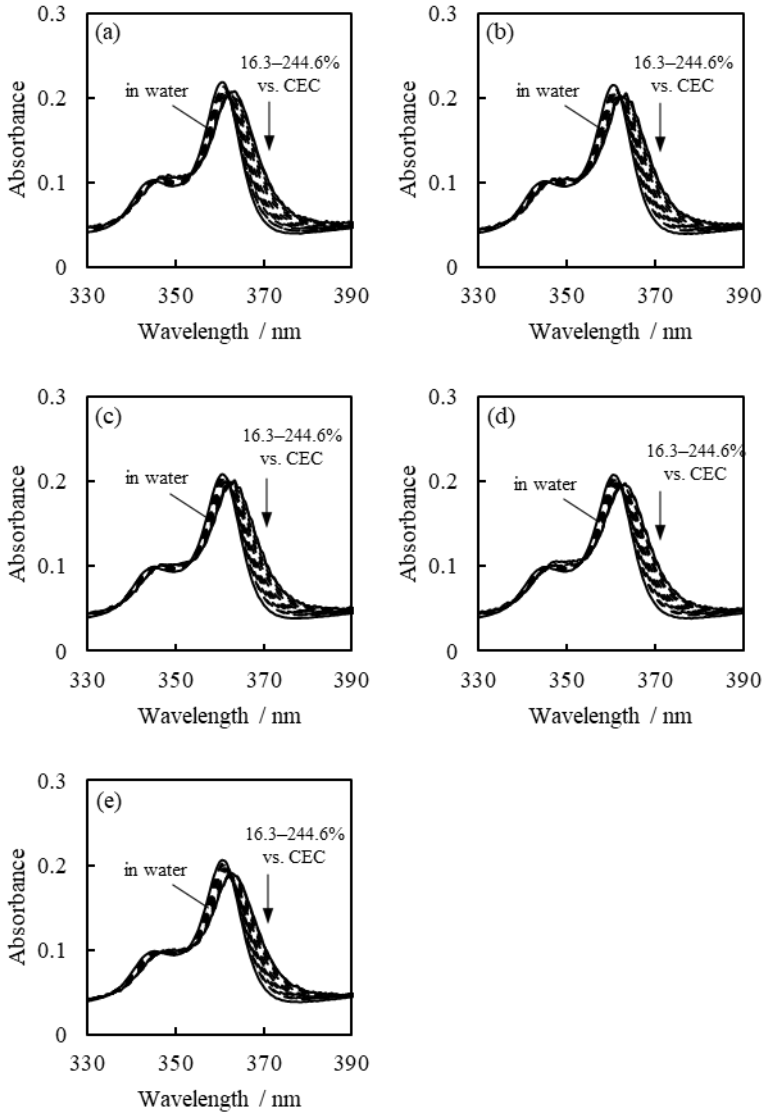

Figure S3.5. UV-vis absorption spectra of $MesAcrPh^+$ with and without Sap1.0 in water. The loading levels of $MesAcrPh^+$ were 16.3, 24.5, 32.6, 40.8 48.9, 65.2, 81.5, 122.3, 163.0, 244.6% vs. CEC: (a)293.15 K, (b)298.15 K, (c)303.15 K, (d)308.15 K, (e)313.15 K. The spectra were corrected with each acridinium derivatives concentration.

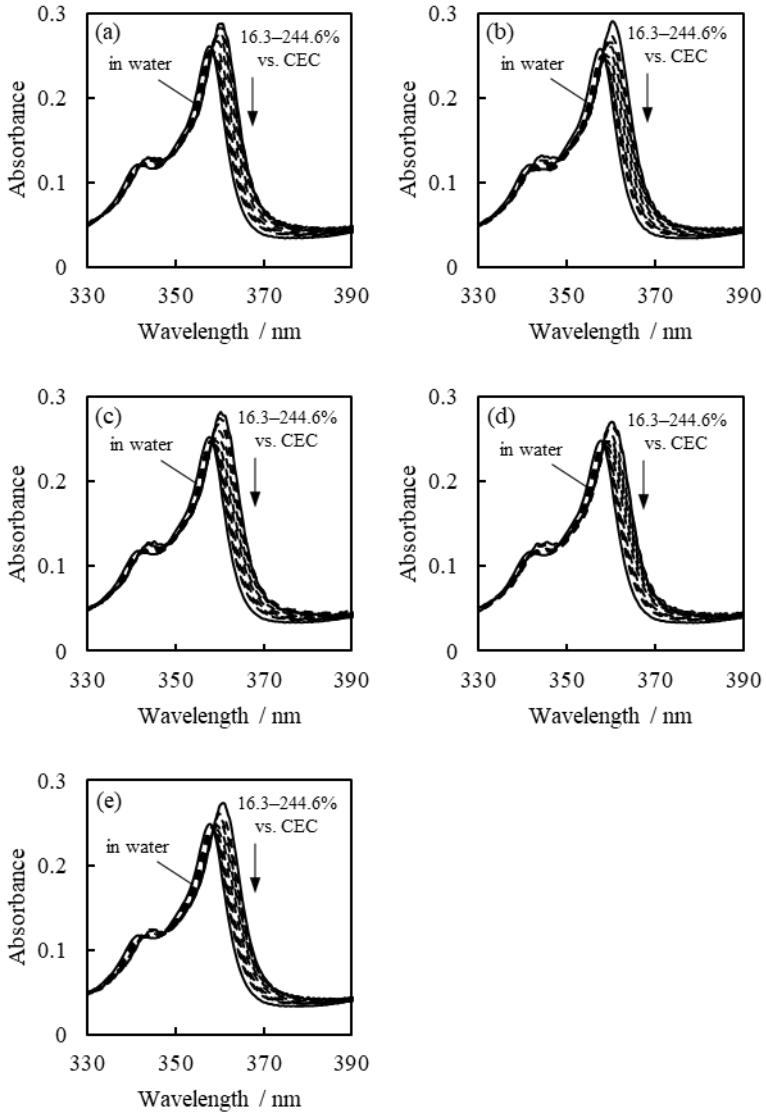

Figure S3.6. UV-vis absorption spectra of Acr^+ with and without Sap1.4 in water. The loading levels of Acr^+ were 16.3, 24.5, 32.6, 40.8 48.9, 65.2, 81.5, 122.3, 163.0, 244.6% vs. CEC: (a)293.15 K, (b)298.15 K, (c)303.15 K, (d)308.15 K, (e)313.15 K. The spectra were corrected with each acridinium derivatives concentration.

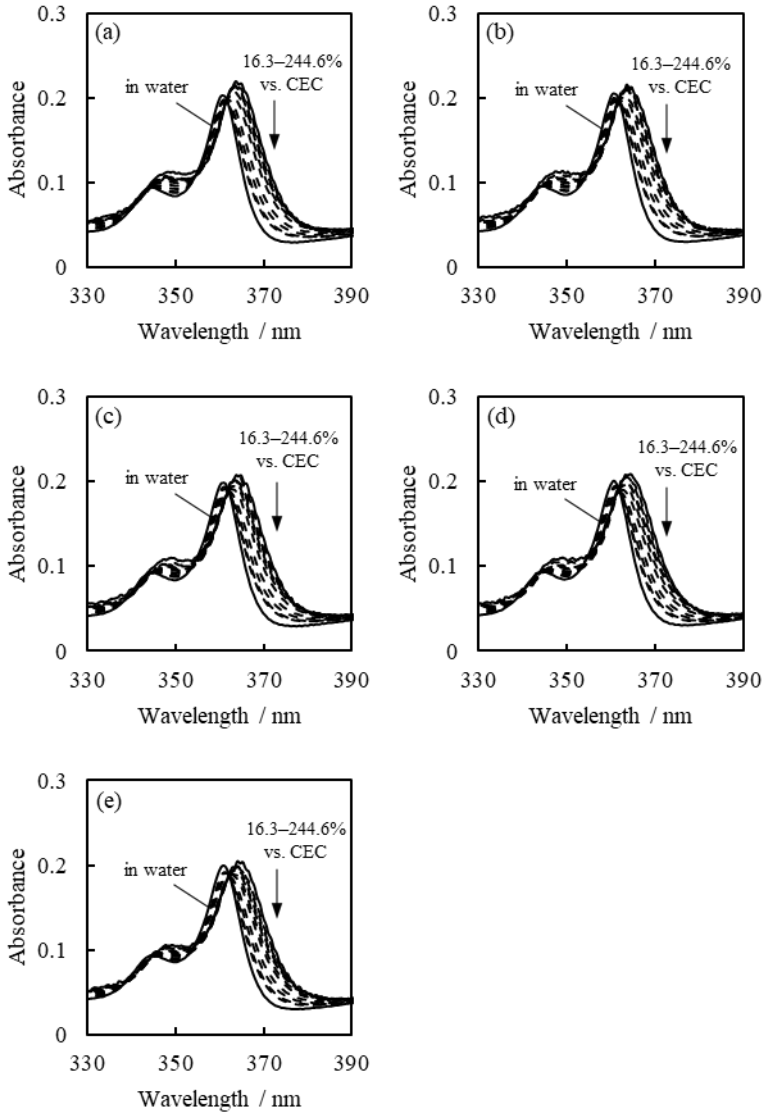

Figure S3.7. UV-vis absorption spectra of $PhAcr^+$ with and without Sap1.4 in water. The loading levels of $PhAcr^+$ were 16.3, 24.5, 32.6, 40.8 48.9, 65.2, 81.5, 122.3, 163.0, 244.6% vs. CEC: (a)293.15 K, (b)298.15 K, (c)303.15 K, (d)308.15 K, (e)313.15 K. The spectra were corrected with each acridinium derivatives concentration.

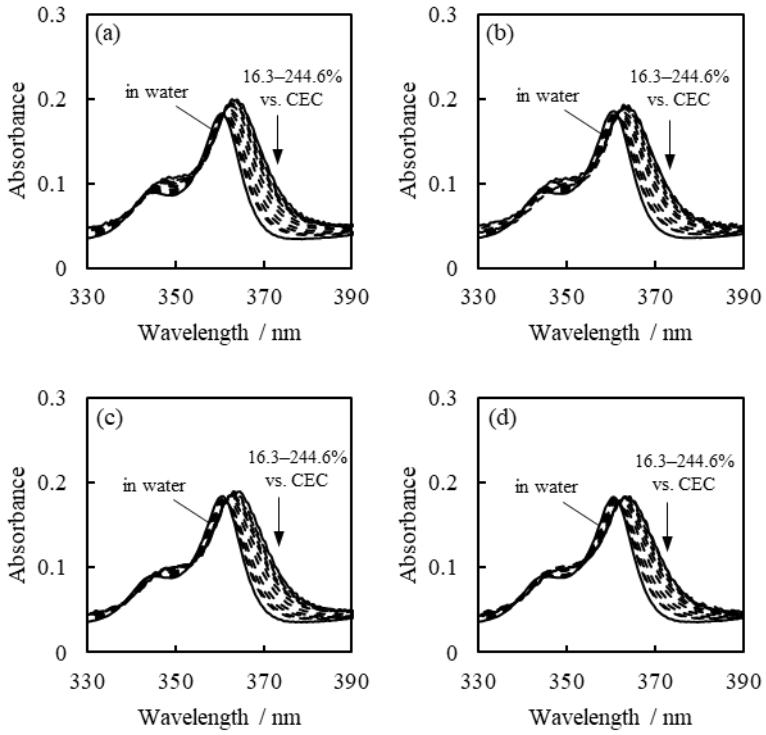

Figure S3.8. UV-vis absorption spectra of $DMPhAcr^+$ with and without Sap1.4 in water. The loading levels of $DMPhAcr^+$ were 16.3, 24.5, 32.6, 40.8 48.9, 65.2, 81.5, 122.3, 163.0, 244.6% vs. CEC: (a)293.15 K, (b)303.15 K, (c)308.15 K, (d)313.15 K. The spectra were corrected with each acridinium derivatives concentration.

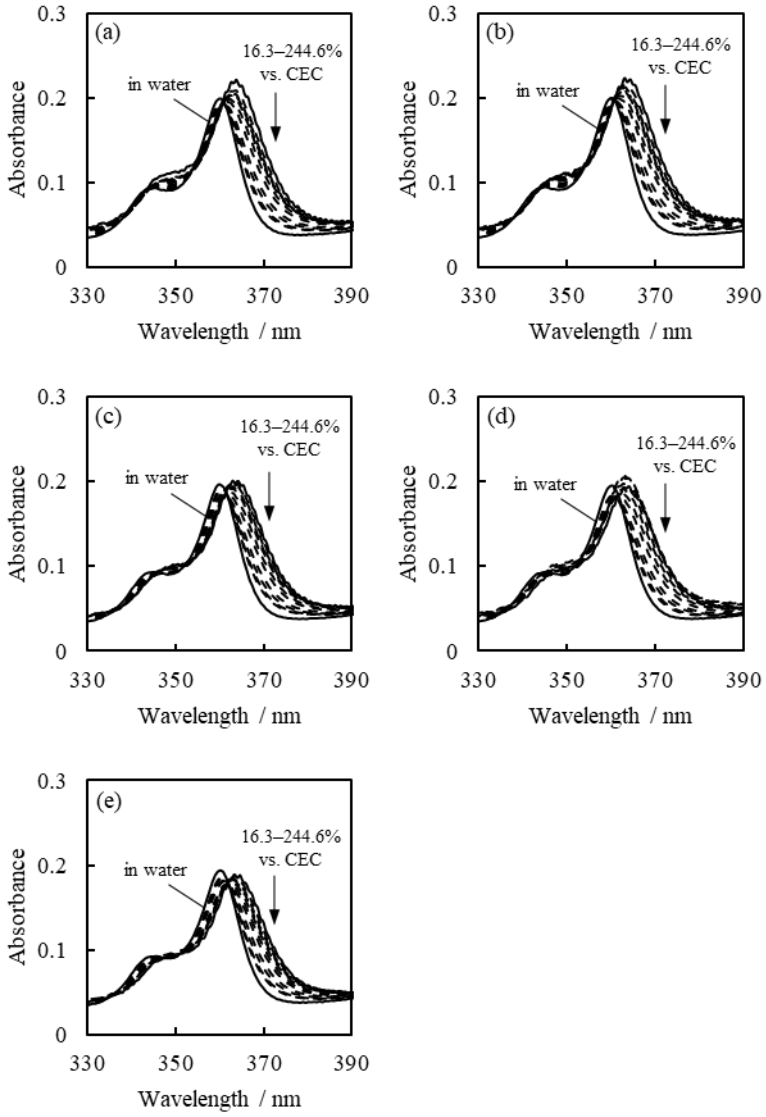

Figure S3.9. UV-vis absorption spectra of $MesAcr^+$ with and without Sap1.4 in water. The loading levels of $MesAcr^+$ were 16.3, 24.5, 32.6, 40.8 48.9, 65.2, 81.5, 122.3, 163.0, 244.6% vs. CEC: (a)293.15 K, (b)298.15 K, (c)303.15 K, (d)308.15 K, (e)313.15 K. The spectra were corrected with each acridinium derivatives concentration.

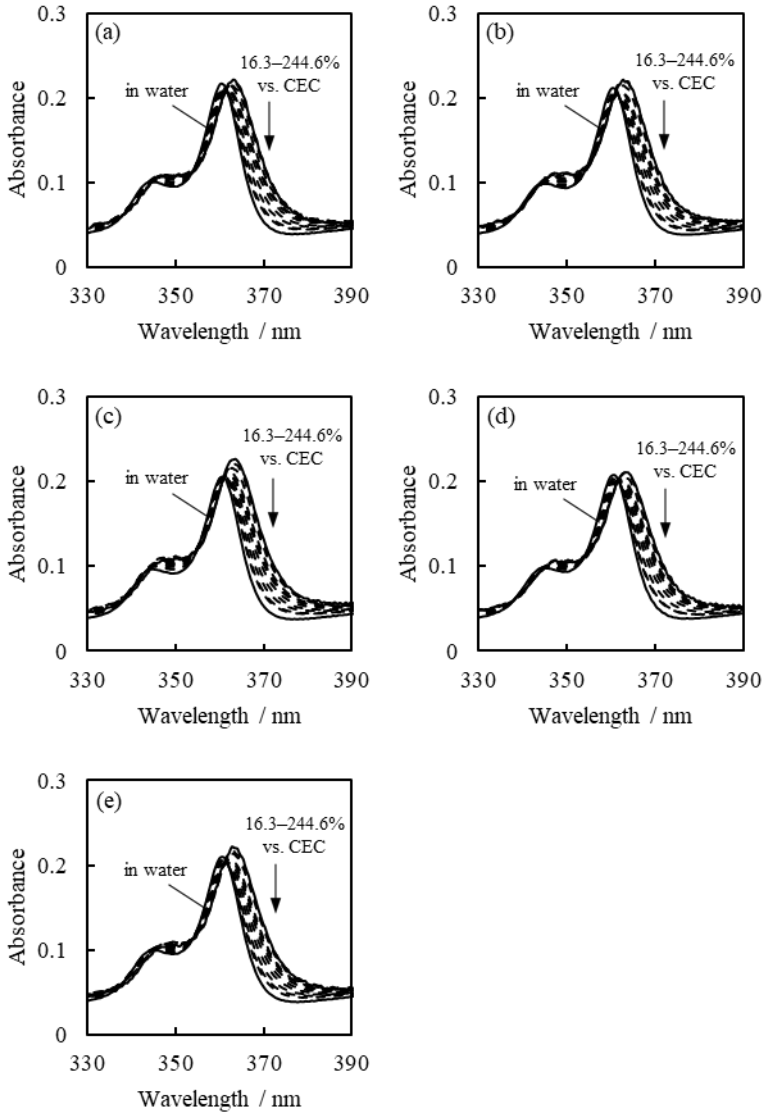

Figure S3.10. UV-vis absorption spectra of $MesAcrPh^+$ with and without Sap1.4 in water. The loading levels of $MesAcrPh^+$ were 16.3, 24.5, 32.6, 40.8 48.9, 65.2, 81.5, 122.3, 163.0, 244.6% vs. CEC: (a)293.15 K, (b)298.15 K, (c)303.15 K, (d)308.15 K, (e)313.15 K. The spectra were corrected with each acridinium derivatives concentration.

3.6. Reference

1. Tahir, S. S.; Rauf, N. Removal of a Cationic Dye from Aqueous Solutions by Adsorption onto Bentonite Clay. *Chemosphere* **2006**, *63*, 1842–1848.
2. Moet, A. S.; Akelah, A. Polymer-clay Nanocomposites: Polystyrene Grafted onto Montmorillonite Interlayers. *Mater. Lett.* **1993**, *18*, 97–102.
3. Weimer, M. W.; Chen, H.; Giannelis, E. P.; Sogah, D. Y. Direct Synthesis of Dispersed Nanocomposites by in Situ Living Free Radical Polymerization Using a Silicate-Anchored Initiator. *J. Am. Chem. Soc.* **1999**, *121*, 1615–1616.
4. Hasegawa, N.; Kawasumi, M.; Kato, M.; Usuki, A.; Okada, A. Preparation and Mechanical Properties of Polypropylene-clay Hybrids Using a Maleic Anhydride-modified Polypropylene Oligomer. *J. Apply. Polym. Sci.* **1998**, *67*, 87–92.
5. Zilg, C.; Thomann, R.; Finter, J.; Mülhaupt, R. The Influence of Silicate Modification and Compatibilizers on Mechanical Properties and Morphology of Anhydride-cured Epoxy Nanocomposites. *Macromol. Mater. Eng.* **2000**, *280–281*, 41–46.
6. Henmi, T.; Huang, P. M. Removal of Phosphorus by Poorly Ordered Clays as Influenced by Heating and Grinding. *Appl. Clay Sci.* **1985**, *1*, 133–144.
7. Danis, T. G.; Albanis, T. A.; Petrakis, D. E.; Pomonis, P. J. Removal of Chlorinated Phenols from Aqueous Solutions by Adsorption on Alumina Pillared Clays and Mesoporous Alumina Aluminum Phosphates. *Water Res.* **1998**, *32*, 295–302.
8. Celis, R.; HermosÍn, M. C.; Cornejo, J. Heavy Metal Adsorption by Functionalized Clays. *Environ. Sci. Technol.* **2000**, *34*, 4593–4599.
9. Bhatt, A. S.; Sakaria, P. L.; Vasudevan, M.; Pawar, R. R.; Sudheesh, N.; Bajaj, H. C.; Mody, H. M. Adsorption of an Anionic Dye from Aqueous Medium by Organoclays: Equilibrium

Modeling, Kinetic and Thermodynamic Exploration. *RSC Adv.* **2012**, *2*, 8663–8671.

10. Ghosh, D.; Bhattacharyya, K. G. Adsorption of Methylene Blue on Kaolinite. *Appl. Clay Sci.* **2002**, *20*, 295–300.
11. Bhattacharyya, K. G.; SenGupta, S.; Sarma, G. K. Interactions of the Dye, Rhodamine B with Kaolinite and Montmorillonite in Water. *Appl. Clay Sci.* **2014**, *99*, 7–17.
12. Ma, Y.; Xu, Z.; Guo, T.; You, P. Adsorption of Methylene Blue on Cu(II)-exchanged Montmorillonite. *J. Colloid Interface Sci.* **2004**, *280*, 283–288.
13. Castellini, E.; Andreoli, R.; Malavasi, G.; Pedone, A. Deflocculant Effects on the Surface Properties of Kaolinite Investigated Through Malachite Green Adsorption. *Colloids Surf. A Physicochem. Eng. Asp.* **2008**, *329*, 31–37.
14. Günay, A.; Ersoy, B.; Dikmen, S.; Evcin, A. Investigation of Equilibrium, Kinetic, Thermodynamic and Mechanism of Basic Blue 16 Adsorption by Montmorillonitic Clay. *Adsorption* **2013**, *19*, 757–768.
15. Rodríguez, A.; Ovejero, G.; Mestanza, M.; García, J. Removal of Dyes from Wastewaters by Adsorption on Sepiolite and Pansil. *Ind. Eng. Chem. Res.* **2010**, *49*, 3207–3216.
16. Ferreiro, E. A.; de Bussetti, S. G. Thermodynamic Parameters of Adsorption of 1,10-Phenanthroline and 2,2′-Bipyridyl on Hematite, Kaolinite and Montmorillonites. *Colloids Surf. A Physicochem. Eng. Asp.* **2007**, *301*, 117–128.
17. Roulia, M.; Vassiliadis, A. A. Sorption Characterization of a Cationic Dye Retained by Clays and Perlite. *Microporous Mesoporous Mater.* **2008**, *116*, 732–740.
18. Rao, W.; Piliouras, P.; Wang, X.; Guido, A.; Kugler, K.; Sieren, B.; Wang, L.; Lv, G.; Li, Z. Zwitterionic Dye Rhodamine B (RhB) Uptake on Different Types of Clay Minerals. *Appl. Clay Sci.* **2020**, *197*, 105790–105800.

19. Sarma, G. K.; SenGupta, S.; Bhattacharyya, K. G. Methylene Blue Adsorption on Natural and Modified Clays. *Sep. Sci. Technol.* **2011**, *46*, 1602–1614.

20. Tran, L.; Wu, P.; Zhu, Y.; Liu, S.; Zhu, N. Comparative Study of Hg(II) Adsorption by Thiol- and Hydroxyl-containing Bifunctional Montmorillonite and Vermiculite. *Appl. Surf. Sci.* **2015**, *356*, 91–101.

21. Egawa, T.; Watanabe, H.; Fujimura, T.; Ishida, Y.; Yamato, M.; Masui, D.; Shimada, T.; Tachibana, H.; Yoshida, H.; Inoue, H.; Takagi, S. Novel Methodology to Control the Adsorption Structure of Cationic Porphyrins on the Clay Surface Using the "Size-Matching Rule." *Langmuir* **2011**, *27*, 10722–10729.

22. Ullah, S.; Bustam, M. A.; Assiri, M. A.; Al-Sehemi, A. G.; Gonfa, G.; Mukhtar, A.; Abdul Kareem, F. A.; Ayoub, M.; Saqib, S.; Mellon, N. B. Synthesis and Characterization of Mesoporous MOF UMCM-1 for CO_2/CH_4 Adsorption; an Experimental, Isotherm Modeling and Thermodynamic Study. *Microporous Mesoporous Mater.* **2020**, *294*, 109844–109848.

23. Krishna, B. S.; Murty, D. S.; Jai Prakash, B. S. Thermodynamics of Chromium (VI) Anionic Species Sorption onto Surfactant-Modifies Montmorillonite Clay. *J. Colloid Interface Sci.* **2000**, *229*, 230–236.

24. Li, Q.; Li, X.; Yang, S.; Gu, P.; Yang, G. Structure, Dynamics, and Stability of Water Molecules during Interfacial Interaction with Clay Minerals: Strong Dependence on Surface Charges. *ACS Omega* **2019**, *4*, 5932–5936.

25. Sheng, G.; Johnston, C. T.; Teppen, B. J. Adsorption of Dinitrophenol Herbicides from Water by Montmorillonites. *Clays Clay Miner.* **2002**, *50*, 25-34.

26. Schnetzer, F.; Johnston, C. T.; Premachandra, G. S.; Giraudo, N.; Schuhmann, R.; Thissen,

P.; Emmerich, K. Impact of Intrinsic Structural Properties on the Hydration of 2:1 Layer Silicates. *ACS Earth Space Chem.* **2017**, *1*, 608-620.

Chapter 4. Enthalpy-Entropy Compensation in Adsorption of Acridinium Derivatives on the Clay Surface

4.1. Introduction

Molecular adsorption is a kind of host-guest system from the viewpoint of supramolecular chemistry. The thermodynamic parameters such as enthalpy change (ΔH) and entropy change (ΔS) represent the driving force of molecular recognition behavior. Therefore, they have been investigated to understand the driving force of complexation not only in 1:1 host-guest systems but also in systems such as adsorption of molecules on adsorbents like clay minerals and zeolites.[1,2–8] Leffler *et al*. have proposed that the enthalpy-entropy compensation relationship is observed in various host-guest systems, in which the values of ΔH and $T\Delta S$ are positively correlated.[9] In order to understand this relationship, a number of studies have been carried out.[10–12] Inoue *et al.* have proposed that the slope α of ΔH and $T\Delta S$ should be used as an indicator of structural change of host and guest during complexation, and the intercept $T\Delta S_0$ of ΔH and $T\Delta S$ should be used as an indicator of desolvation.[13] These reports discuss the slope and intercept of the enthalpy-entropy compensation by integrating the values of ΔH and $T\Delta S$ reported separately in various papers. The characteristics of structural changes and desolvation during complexation have been discussed by using slopes and intercepts of enthalpy-entropy compensation in molecular inclusion by cyclodextrins, cation capture by crown ethers, and DNA/RNA intercalation.[17–19] Although some reports refer to enthalpy-entropy compensation for adsorption of molecules on clay minerals,[6,16] there are no reports discussing the characteristics during complexation by using the slope and intercept of enthalpy-

entropy compensation

Chapter 2 indicated the change in ΔH and ΔS of adsorption with the change in the cross-sectional area of the guest molecule. Chapter 3 indicated the change in ΔH and ΔS of adsorption with the inter-negative charge distance of the surface of synthetic saponites. In this chapter, the slope and intercept of enthalpy-entropy compensation of the adsorption of acridinium derivatives on synthetic saponites derived by the thermodynamic parameters revealed in Chapter 2 and Chapter 3 were compared with those of other host-guest systems. The desolvation and structural change in molecular adsorption on clay minerals were discussed.

4.2. Experimental section

The thermodynamic parameters for the adsorption of acridinium derivatives on synthetic saponite were the values calculated in Chapter 2 and Chapter 3.

4.3. Result and Discussion

4.3.1. Enthalpy-entropy compensation of adsorption of acridinium derivatives on synthetic saponites

In the complexation thermodynamics involving host and guest, the entropic change $T\Delta\Delta S$, induced by internal and external fluctuation such as altering solvent and substituents of host and guest, is proportional to the enthalpic change $\Delta\Delta H$. This relationship is empirically expressed in the eq 4.1 with a proportional coefficient α.[15]

$$T\Delta\Delta S = \alpha\Delta\Delta H \qquad (4.1)$$

Integrating the Eq. (4.1) leads to the extrathermodynamic Eq. (4.2) representing the compensatory relationship between $\Delta\Delta H$ and $T\Delta\Delta S$.

$$T\Delta S = \alpha\Delta H + T\Delta S_0 \quad (4.2)$$

Combining Gibbs-Helmholtz equation (Eq. (4.3)) with Eq. (4.2), Eq. (4.4) is obtained as follows.

$$\Delta\Delta G = \Delta\Delta H - T\Delta\Delta S \quad (4.3)$$

$$\Delta\Delta G = (1 - \alpha)\Delta\Delta H \quad (4.4)$$

Eq (4.4) indicates that, even if the enthalpic gain was obtained by any fluctuation such as ligand, solvent, or any other, this enthalpic gain is not fully reflected in the stabilization of complex and is canceled in part by the entropic loss represented by (1−α). For example, the slope α is smaller in the rigid host-guest system, such as the inclusive complexation of metal ions in cryptand and ligation of pyridine derivatives to metalloporphyrin.[17,20] By contrast, the soft host-guest system such as biological hosts, that are, enzyme and DNA/RNA, have a larger slope α.[15] Thus, the slope of enthalpy-entropy compensation quantitively indicates the entropic loss at complexation. Since the tendency of the slope is related to the flexibility of the host structure, it is reasonable to assume that structural change at complexation is reflected as an entropic loss.[15]

The intercept $T\Delta S_0$ represents that Gibbs free energy change (ΔG) of complexation when ΔH is zero. A positive $T\Delta S_0$ means that the complexation can occur without enthalpic gain. It has been found that $T\Delta S_0$ is positive in many complexes such as artificial hosts, natural hosts, and biomolecules.[15] The factor of positive entropy change is the increase in the degree of freedom caused by desolvation induced by the complexation of host and guest. For example, the intercept of pyridine coordination to metalloporphyrin is very small. On the other hand, DNA and RNA have a much larger intercept, indicating that a large amount of constrained

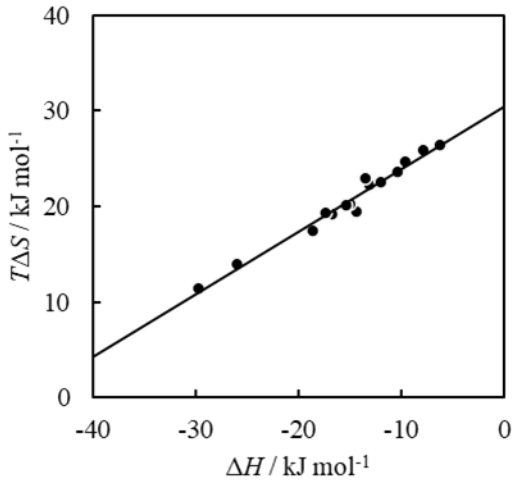

Figure 4.1. Enthalpy-entropy compensation plot for adsorption of acridinium derivatives on synthetic saponites.

Table 4.1. Slopes (α) and Intercepts ($T\Delta S_0$) of the Enthalpy-Entropy Compensation Plot for Acridinium Derivatives-Synthetic Saponite Complex and Other Host-Guest Complexes

host	guest	α	$T\Delta S_0$ / kJ mol^{-1}	reference
synthetic saponites	cationic acridinium	0.65	30.4	this work
crown ether	ion	0.76	10.0	14,18
cryptand	ion	0.51	16.7	14
cyclodextrin	organic molecule	0.90	13.0	13,20
metalloporphyrin	pyridine	0.61	6.7	17
enzyme	coenzyme	1.11	29.3	15
DNA/RNA	intercalator	1.03	35.6	15

solvent (water) is released when DNA is complexed with an intercalator or substrate. Previous literature, therefore, has suggested that $T\Delta S_0$ is the quantitative degree of desolvation induced by the complexation of host and guest.

ΔH and $T\Delta S$ of adsorption of mono-cationic acridinium derivatives on synthetic saponites in this paper showed a linear relationship (Figure 4.1). This relationship suggests that enthalpy and entropy compensate each other in not only the complexation such as supramolecules and biomolecules but also the adsorption on the solid surface. The slope and intercept of ΔH and $T\Delta S$ were 0.65 and 30.4, respectively (Table 4.1). In addition, the slopes

and the intercepts of enthalpy-entropy compensation of other typical host-guest systems are summarized in Table 4.1. The adsorption of mono-cationic acridinium derivatives on synthetic saponites showed a relatively small slope, which was close to the rigid host-guest system such as crown ether and metalloporphyrin. This result suggests that the structural change of synthetic saponite upon adsorption is small and that the rigid structure of synthetic saponite is maintained.

On the other hand, the intercept of the adsorption of mono-cationic acridinium derivatives on synthetic saponites showed a larger value, which was close to the intercept of DNA/RNA and enzyme. As mentioned above, larger intercepts of DNA/RNA and enzyme reflect that a large amount of constrained solvent is released upon the complexation with intercalator or substrate. Since clay minerals have much-adsorbed water on the surface, adsorbed water was desorbed when another molecule adsorbed on the clay surface. It can thus be suggested that the entropy gain due to desolvation at the same level as DNA/RNA and enzyme affects the adsorption in the system of synthetic saponites with mono-cationic acridinium derivatives. Interestingly, the synthetic saponites and acridinium derivatives system showed a small slope specific to the rigid hosts and a large intercept specific to the soft hosts. This is the characteristic in which the entropy loss due to the structural change is small, and the entropy gain due to the desolvation is large, suggesting that clay minerals have an ideal space to form a strong complex.

4.3.2. Enthalpy-entropy compensation of adsorption of mono-cationic dyes on clay minerals in previous literature

To discuss the effect of the type of clay minerals on enthalpy-entropy compensation, we

surveyed ΔH and $T\Delta S$ of adsorption of cationic dye molecules on clay minerals in previous literature. The ΔH and $T\Delta S$ of adsorption of cationic dye molecules on smectite and kaolinite were surveyed. The thermodynamic parameters of adsorption of cationic dye molecules on clay minerals are summarized in Table 4.2 and Table 4.3. The data for smectites are shown in Table 4.2, while those for kaolinites are listed in Table 4.3. It should be noted that ΔG and $T\Delta S$ are the values at 298K. The driving forces of the complexation of clay minerals with cationic dyes in organic solvents may differ from those in water since the swelling property and the dispersity of clay minerals depend on the combination of the type of counter cation of clay minerals and solvents. Thermodynamic parameters, therefore, were collected only from the data experimented in water. For all original data, the standard Gibbs free energy change calculated from the enthalpy and entropy changes reported in the original paper was compared with that calculated from the equilibrium constants at the standard state. If a difference was larger than 4 kJ mol^{-1}, the thermodynamic parameters were recalculated using the raw experimental data in the original paper. The plot of enthalpy-entropy compensation is shown in Figure 4.2. The slopes and intercepts are shown in Table 4.4.

Table 4.2. Thermodynamic Parameters for Adsorption of Cationic Compounds on Smectite

guest	host	clay concentration / g L^{-1}	ΔG / kJ mol^{-1}	ΔH / kJ mol^{-1}	$T\Delta S$ / kJ mol^{-1}	ref
methylene blue	montmorillonite	0.5	−1.69	145.0	146.7	1
malachite green	bentonite	0.5	−23.37	−14.24	9.13	4
malachite green	bentonite	0.5	−23.25	−20.62	2.63	4
malachite green	bentonite	0.5	−22.99	−22.74	0.26	4
malachite green	bentonite	0.5	−22.01	−24.59	−2.58	4
methylene blue	modified montmorillonite by octylphenol polyoxyethylene ether	0.625	−3.05	2.91	5.96	21

Table 4.2. (continued)

guest	host	clay concentration / g L^{-1}	ΔG / kJ mol^{-1}	ΔH / kJ mol^{-1}	$T\Delta S$ / kJ mol^{-1}	ref
methylene blue	modified montmorillonite by octylphenol polyoxyethylene ether	0.625	−4.74	4.20	8.94	21
methylene blue	modified montmorillonite by octylphenol polyoxyethylene ether	0.625	−3.26	2.70	5.96	21
methylene blue	modified montmorillonite by octylphenol polyoxyethylene ether	0.625	−3.96	7.97	11.93	21
methylene blue	modified montmorillonite by octylphenol polyoxyethylene ether	0.625	−3.19	5.75	8.94	21
malachite green	bentonite	10	−5.53	13.44	18.97	22
rhodamine B	montmorillonite	0.4	0.62	7.48	6.86	23
rhodamine B	modified montmorillonite by H_2SO_4	0.4	0.43	7.29	6.86	23
rhodamine B	modified montmorillonite by H_2SO_4	0.4	0.34	7.20	6.86	23
basic red 13	modified montmorillonite by sodium dodecyl sulfate	0.1	−2.23	11.11	13.34	24
1-allyl-3-methy-limidazolium chloride	Na-montmorillonite	2	−4.44	6.50	10.94	25
1-methyl-3-butyl-imidazolium chloride	Na-montmorillonite	2	−3.84	5.40	9.24	25
1-methyl-3-octylimidazolium chloride	Na-montmorillonite	2	−3.80	6.40	10.20	25
1-butylpyridiniym bromide	Na-montmorillonite	2	−4.72	8.70	13.42	25
1-octylpyridiniym bromide	Na-montmorillonite	2	−4.11	9.90	14.01	25
1-hexadecyl-3-methylimidazolium chloride	Ca-montmorillonite	20	−3.99	-2.58	1.41	26
1-hexadecyl-3-methylimidazolium chloride	Ca-montmorillonite	20	−4.17	−2.12	2.05	26
1-hexadecyl-3-methylimidazolium chloride	Ca-montmorillonite	20	−4.12	−3.37	0.75	26
N-pentyl-4-(*p*-*N*,*N*-dimethylamino styryl) pyridinium iodide	Na-montmorillonite	2	4.04	39.93	35.89	27
N-heptyl-4-(*p*-*N*,*N*-dimethylamino styryl) pyridinium iodide	Na-montmorillonite	2	3.14	37.93	34.79	27

Table 4.2. (continued)

guest	host	clay concentration / g L^{-1}	ΔG / kJ mol^{-1}	ΔH / kJ mol^{-1}	$T\Delta S$ / kJ mol^{-1}	ref
N-decyl-4-(*p*-*N*,*N*-dimethylamino styryl) pyridinium iodide	Na-montmorillonite	2	1.79	12.28	10.49	27
N-octadecyl-4-(*p*-*N*,*N*-dimethylamino styryl) pyridinium iodide	Na-montmorillonite	2	1.54	7.97	6.43	27
amitriptyline hydrochloride	Ca-montmorillonite	2.5	−21.85	19.89	41.74	28
basic blue 41	bentonite	5	−10.26	16.80	27.06	9
basic blue 41	Na-montmorillonite	5	−13.17	8.05	21.22	9
rhodamine B	modified bentonite by cetyl-trimethylammonium bromide	0.8	−3.29	6.10	9.39	29
crystal violet	modified bentonite by H_2SO_4 and HCl	10	−16.62	26.07	42.70	30
malachite green	modified montmorillonite by hexadecyltrimethylammonium bromide	8	−16.12	16.32	32.43	31
methylene blue	bentonite	2	−18.28	9.21	27.49	32
basic red 46	bentonite	1	-8.19	8.80	16.99	33
basic yellow 28	bentonite	1	−4.46	8.30	12.76	33
crystal violet	bentonite	1	−6.29	-83.81	-77.52	34
crystal violet	Ni-bentonite	1	−0.91	54.58	53.7	34
crystal violet	Co-bentonite	1	0.20	41.94	41.74	34
crystal violet	Zn-bentonite	1	0.27	39.03	38.76	34
methylene blue	Na-montmorillonite	1	−4.83	2.92	7.75	5
methylene blue	modified Na-montmorillonite by $CuSO_4$	1	−4.69	2.31	7.00	5
methylene blue	Ca-montmorillonite	1	−4.52	2.77	7.29	5
methylene blue	modified Ca-montmorillonite by $CuSO_4$	1	−4.41	2.26	6.67	5
basic blue 16	montmorillonite	2	−10.57	112.7	123.3	6
basic blue 16	montmorillonite	2	−5.43	64.21	69.64	6
basic blue 16	montmorillonite	2	−2.64	20.15	22.79	6
astrazon golden yellow 7GL	modified montmorillonite by H_2SO_4	0.5	−25.13	19.00	44.13	35
supranol yellow 4GL	modified bentonite by cetyl-trimethylammonium bromide	5	−22.97	33.68	56.65	36
promethazine hydrochloride	montmorillonite	4	−6.01	49.74	55.75	37
ammonium chloride	Na-montmorillonite	2	−1.90	-10.50	-8.60	38
methylene blue	montmorillonite	0.4	−2.21	1.02	3.23	21

Table 4.2. (continued)

guest	host	clay concentration / g L^{-1}	ΔG / kJ mol^{-1}	ΔH / kJ mol^{-1}	$T\Delta S$ / kJ mol^{-1}	ref
methylene blue	modified montmorillonite by H_2SO_4	0.4	−2.29	1.22	3.51	21
methylene blue	modified montmorillonite by H_2SO_4	0.4	−2.53	0.97	3.50	21
crystal violet	hydrogel with Na-montmorillonite	1	−1.54	79.26	80.80	39
basic red 18	montmorillonite	0.05	−3.89	42.62	46.54	40
crystal violet	Ca-montmorillonite	1	−1.20	40.42	41.62	41
methyl violet	Na-bentonite	2.5	−6.09	12.94	19.03	42
methyl violet	Na-bentonite	2.5	−8.04	6.66	14.70	42
methyl violet	Na-bentonite	2.5	−7.51	21.02	28.52	42
methyl violet	Na-bentonite	2.5	−8.08	5.27	13.36	42
methyl violet	Na-bentonite	2.5	−8.48	8.58	17.05	42
basic red 46	modified bentonite by HCl	0.1	−7.35	−17.14	−9.79	43
methylene blue	modified bentonite by chitosan	0.2	−21.72	23.90	45.63	44
malachite green	modified Na-montmorillonite by graphene oxide	0.16	−13.66	47.47	61.14	45
methylene blue	modified bentonite by chitosan	0.2	−33.85	−90.50	−56.65	46
methylene blue	Ca-montmorillonite	0.5	−24.26	−22.02	2.31	47
methylene blue	modified Ca-montmorillonite by $CoFe_2O_4$	0.5	−25.67	−25.83	−0.16	47
methylene blue	modified Ca-montmorillonite by $CoFe_2O_4$ and graphene oxide	0.5	−27.62	−39.88	−12.26	47
methylene blue	Na-montmorillonite	1	−1.75	−2.96	−1.21	48
methylene blue	modified montmorillonite by hydroxyapatite and chitosan	1	−28.69	−17.83	10.86	49
methylene blue	modified montmorillonite by n-hexadecyltrimethylammonium chloride	2	−3.15	12.72	15.86	50
rhodamine B	modified Na-bentonite by cetyltrimethylammonium bromide	0.8	−3.29	6.10	9.39	51
rhodamine B	modified Na-bentonite by sodium dodecylbenzene sulfonate	0.8	0.44	3.32	2.79	51
tetracycline	modified Na-montmorillonite by carboxymethyl chitosan	2	−6.31	−18.18	−11.87	52
chlortetracycline	modified Na-montmorillonite by carboxymethyl chitosan	2	−6.82	−25.05	−18.24	52
crystal violet	modified Na-montmorillonite by graphene oxide	0.25	−7.87	7.06	14.93	53
methylene blue	modified montmorillonite by sodium alginate	2	−4.48	62.60	67.08	54
methyl green	montmorillonite	0.196	−21.51	30.63	52.16	55
methylene blue	modified montmorillonite by iron oxide	2	7.45	5.36	−2.10	56

Table 4.2. (continued)

guest	host	clay concentration / g L^{-1}	ΔG / kJ mol^{-1}	ΔH / kJ mol^{-1}	$T\Delta S$ / kJ mol^{-1}	ref
methylene blue	montmorillonite	1.5	−4.64	−28.79	−24.15	57
methylene blue	montmorillonite	1.5	−2.02	−20.81	−18.78	57
methylene blue	montmorillonite	1.5	−0.21	−15.12	−14.91	57
methylene blue	montmorillonite	1.5	0.72	−12.99	−13.71	57
methylene blue	montmorillonite	1.5	1.45	−11.97	−13.42	57
crystal violet	montmorillonite	0.1	−10.83	84.58	95.41	58
neutral red	Na-montmorillonite	0.1	−7.32	−1.95	5.37	59
neutral red	Na-montmorillonite	0.1	−9.44	2.79	12.22	59
neutral red	Na-montmorillonite	0.1	−10.20	8.88	19.08	59
neutral red	Na-montmorillonite	0.1	−9.60	11.57	21.17	59
neutral red	Na-montmorillonite	0.1	−7.32	−1.95	5.37	59
neutral red	Na-montmorillonite	0.1	−9.44	2.79	12.22	59
neutral red	Na-montmorillonite	0.1	−10.20	8.88	19.08	59
neutral red	Na-montmorillonite	0.1	−9.60	11.57	21.17	59
neutral red	Na-montmorillonite	0.1	−8.66	11.32	19.98	59
neutral red	Na-montmorillonite	0.1	−7.74	6.58	14.31	59
malachite green	Na-montmorillonite	0.1	−7.21	2.04	9.24	59
malachite green	Na-montmorillonite	0.1	−9.35	4.66	14.01	59
malachite green	Na-montmorillonite	0.1	−10.09	7.98	17.89	59
malachite green	Na-montmorillonite	0.1	−10.09	16.15	26.24	59
malachite green	Na-montmorillonite	0.1	−10.08	21.23	31.31	59
malachite green	Na-montmorillonite	0.1	−9.39	26.09	35.48	59
methylene blue	modified montmorillonite by $CoFe_2O_4$	2	−10.03	16.85	26.88	60
supranol yellow 4GL	modified montmorillonite by $Cr(NO_3)_3$	0.3	−14.07	−43.53	−29.46	61
rhodamine 6G	Na-montmorillonite	2	−27.80	5.00	32.80	62

Table 4.3. Thermodynamic Parameters for Adsorption of Cationic Compounds on Kaolinite

guest	host	clay concentration / g L^{-1}	ΔG / kJ mol^{-1}	ΔH / kJ mol^{-1}	$T\Delta S$ / kJ mol^{-1}	ref
cationic polyacrylamide	kaolinite	2	−5.15	23.20	28.35	63
methylene blue	kaolinite	2.5	0.76	4.10	3.34	64
methylene blue	modified kaolinite by Fe_3O_4	2.5	−1.43	37.00	38.43	64
methylene blue	raw kaolinite	0.8	−13.97	9.40	23.37	3
methylene blue	pure kaolinite	0.8	−14.38	7.54	21.92	3
methylene blue	calcined raw kaolinite	0.8	−12.75	13.53	26.28	3
methylene blue	calcined pure kaolinite	0.8	−13.30	11.84	25.14	3

Table 4.3. (continued)

guest	host	clay concentration / g L^{-1}	ΔG / kJ mol^{-1}	ΔH / kJ mol^{-1}	$T\Delta S$ / kJ mol^{-1}	ref
methylene blue	modified raw kaolinite by NaOH	0.8	−14.44	7.92	22.36	3
methylene blue	modified pure kaolinite by NaOH	0.8	−14.75	6.03	20.78	3
rhodamine B	kaolinite	2.4	−1.60	50.28	51.88	65
rhodamine B	kaolinite	2.4	−1.13	46.57	47.70	65
rhodamine B	kaolinite	2.4	−0.82	33.47	34.29	65
rhodamine B	kaolinite	2.4	−0.91	22.64	23.55	65
rhodamine B	kaolinite	2.4	−0.37	18.71	19.08	65
methylene blue	kaolinite	2.5	−0.24	14.11	14.35	66
methylene blue	modified kaolinite by H_2SO_4	2.5	−2.87	7.32	10.19	66
basic yellow 28	kaolinite	2	−0.90	17.77	18.66	67
methylene blue	kaolinite	2	−1.31	26.38	27.70	67
malachite green	kaolinite	2	−3.18	68.70	71.88	67
rhodamine B	kaolinite	2	5.13	12.58	7.45	4
rhodamine B	modified kaolinite by H_2SO_4	2	4.92	12.67	7.75	4
rhodamine B	modified kaolinite by H_2SO_4	2	4.69	11.25	6.56	4
crystal violet	kaolinite	1	−3.68	0.24	3.92	68
crystal violet	kaolinite	1	−4.12	0.14	4.26	68
crystal violet	kaolinite	1	−3.14	0.18	3.32	68
brilliant green	kaolinite	1	−4.37	−21.25	−16.83	68
brilliant green	kaolinite	1	−3.61	−23.26	−19.00	68
brilliant green	kaolinite	1	−3.01	−24.84	−20.69	68
rhodamine B	kaolinite	20	−13.53	1.38	14.91	83
rhodamine 6G	kaolinite	25	−14.19	3.70	17.89	62
malachite green	Na-kaolinite	5.3	−31.51	−33.90	−2.39	6
malachite green	modified Na-kaolinite by sodium disilicate	5.3	−30.51	−32.00	−1.49	6
malachite green	modified Na-kaolinite by sodium disilicate	5.3	−29.10	−29.70	−0.60	6
malachite green	modified Na-kaolinite by sodium hexa-metaphospate	5.3	−31.62	−34.60	2.98	6
malachite green	modified Na-kaolinite by sodium hexa-metaphospate	5.3	−31.93	−36.70	−4.77	6
methylene blue	kaolinite	1	−8.53	−26.00	−17.47	69
malachite green	kaolinite	1	−11.27	−25.10	−13.83	69
malachite green	kaolinite	1	−2.98	−29.81	−26.83	70
malachite green	kaolinite	1	−10.93	−61.62	−50.69	70
brilliant green	kaolinite	2	−4.80	8.91	13.71	71
brilliant green	modified kaolinite by H_2SO_4	2	−0.79	14.12	14.91	71
brilliant green	modified kaolinite by H_2SO_4	2	−0.89	15.81	16.70	71
crystal violet	kaolinite	2	1.50	−16.21	−17.71	71
crystal violet	modified kaolinite by H_2SO_4	2	1.36	−16.25	−17.61	71

Table 4.3. (continued)

guest	host	clay concentration / g L^{-1}	ΔG / kJ mol^{-1}	ΔH / kJ mol^{-1}	$T\Delta S$ / kJ mol^{-1}	ref
crystal violet	modified kaolinite by H_2SO_4	2	5.51	−12.45	−17.96	71
methylene blue	kaolinite	2	−5.91	0.02	5.92	21
methylene blue	modified kaolinite by H_2SO_4	2	−5.91	0.03	4.58	21
methylene blue	modified kaolinite by H_2SO_4	2	−5.19	−0.06	4.90	21
basic red 46	kaolinite	0.4	−37.53	−25.60	11.93	72
basic yellow 28	beneficiated kaolinite	10	−1.95	−43.99	−42.04	73
basic yellow 28	raw kaolinite	10	−1.11	−35.70	−34.59	73
basic yellow 28	calcined kaolinite	10	0.35	−30.95	−31.31	73
methylene blue	modified kaolinite by $CuFe_2O_4$	1	−10.61	−71.40	−60.79	74
methyl violet	modified kaolinite by $CuFe_2O_4$	1	−9.53	−58.10	−48.57	74
methylene blue	kaolinite	1	−0.29	10.45	10.73	75
methylene blue	modified kaolinite by DMSO	1	14.10	−2.60	−16.70	75
methyl violet	kaolinite	2.5	−21.11	−6.82	14.29	76
methyl violet	modified kaolinite by $CuFe_2O_4$	1	−9.53	−58.10	−48.57	74
methylene blue	kaolinite	1	−0.29	10.45	10.73	75
methylene blue	modified kaolinite by DMSO	1	14.10	−2.60	−16.70	75
methyl violet	kaolinite	2.5	−21.11	−6.82	14.29	76

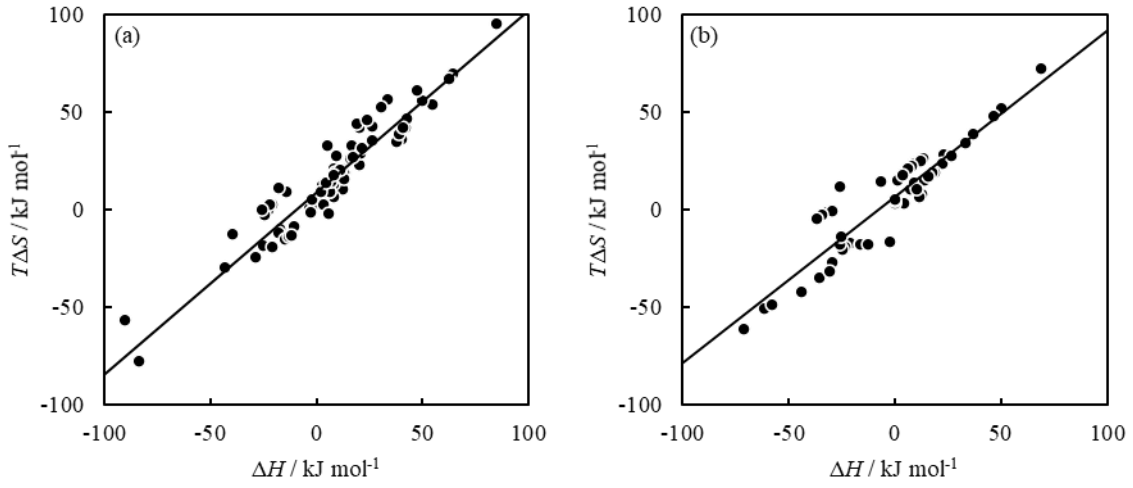

Figure 4.2. Enthalpy-entropy compensation plot for adsorption of mono-cationic dyes on clay minerals (a) smectite (b) kaolinite.

As shown in Figure 4.2, the adsorptions of other cationic dyes on clay minerals indicated enthalpy entropy compensation. However, the slopes of enthalpy-entropy compensation

Table 4.4. Slopes (α) and Intercepts ($T\Delta S_0$) of the Enthalpy-Entropy Compensation Plot for the Complexation of Mono-Cationic Dyes and Clay Minerals

host	α	$T\Delta S_0$ / kJ mol^{-1}
smectite	0.93	8.7
kaolinite	0.85	6.7

shown in Table 4.4 were larger than that of the adsorption of acridinium derivatives on synthetic saponites reported in this paper. The intercepts of enthalpy-entropy compensation shown in Table 4.4 were smaller than that of the adsorption of acridinium derivatives on synthetic saponites reported in this paper as well. Let us discuss the cause of which difference of the slopes and intercepts of enthalpy–entropy compensation in the adsorption appeared, although the type of clay minerals and dyes are the same. As shown in Table 4.4, the slopes and intercepts were about 0.9 and 7, respectively, regardless of the type of clay minerals. This result means that the type of clay minerals did not significantly affect the slope and intercept of enthalpy-entropy compensation.

Secondly, the experimental adsorption condition was focused. As shown in Table 4.2 and Table 4.3, the concentrations of clay minerals under the experimental adsorption condition reported in many papers were different from those reported in this paper. The clay minerals concentrations in other papers were about 10 to 100 times higher than those in this paper. According to multiple reports, when the concentration of clay minerals is high, the clay minerals remain laminated without exfoliation completely or form an aggregation state such as a card-house structure.[77,78] It is possible that the clay minerals remain laminated or form an aggregation at the concentration of 0.1–20 g L^{-1}, which is the condition of the adsorption experiment in previous reports. When the organic molecules adsorb on the clay minerals,

which are laminated or aggregated, the organic molecules intercalate in the interlamellar of clay minerals without breaking the laminated or aggregated state.[79–81] Laminated clay minerals expand their interlayer space to adsorb the organic molecules. It is possible, therefore, that the structural change in host materials occurs when the organic molecules adsorb on clay minerals. By contrast, clay minerals are dispersed in water in an exfoliated state when the concentration of clay minerals is sufficiently low.[82] When any molecules adsorb on exfoliated clay minerals, it can thus be suggested that the structural change in clay minerals as host materials is small because the interlayer distance is already expanded. For this reason, it is possible that the slope of enthalpy-entropy compensation in this paper became smaller than those in previous papers at the concentration of 0.1–20 g L^{-1}.

Finally, let us discuss the surface adsorbed water when clay minerals are laminated or aggregated and when clay minerals are completely exfoliated. When the dye molecules are adsorbed on clay minerals which are exfoliated completely as in the system in this study, it is possible that the water molecules which adsorb on the clay surface are pushed out by the dye molecules and obtain a large degree of freedom. By contrast, when the dye molecules are adsorbed on clay minerals that are laminated or aggregated, the dyes are intercalated in the interlayer space of clay minerals, as mentioned above. It can thus be suggested that the water molecules which are pushed out by the dye molecules are not released much into the solution since they have no way out. This difference is the reason that the intercept of enthalpy-entropy compensation of the system in this study was larger than those in previous papers at the concentration of 0.1–20 g L^{-1}. In summary, it was found that the concentration of clay minerals plays an important role in the driving force of complexation, such as structural change and desolvation.

4.4. Conclusion

The plot of ΔH versus $T\Delta S$ in this system indicated enthalpy-entropy compensation. Compared to other host-guest systems, enthalpy-entropy compensation of adsorption of acridinium derivatives on synthetic saponites indicated a small slope specific to rigid host materials and a large intercept specific to soft host materials. The small slope and the large intercept of enthalpy-entropy compensation in this system suggest that the adsorption of acridinium derivatives on synthetic saponites shows a small structural change specific to rigid host materials and a large desolvation specific to soft host materials. In order to clarify the difference between the system of clay minerals and other host-guest systems previously reported, ΔH and $T\Delta S$ of adsorption of cationic dyes on clay minerals were surveyed from previous papers. The slopes and intercepts of enthalpy-entropy compensation calculated from the survey were about 0.9 and 7.0, respectively, regardless of the type of clay minerals. This suggests that the slope and intercept of enthalpy-entropy compensation plot, that is, structural change and desolvation during complexation, are affected by the concentration of clay minerals rather than the type of clay minerals. Although enthalpy-entropy compensation was often a problem in forming a strong complex and supramolecules, it is suggested that the adsorption of mono-cationic acridinium derivatives on synthetic saponites was an ideal space for forming a strong complex because the entropy loss due to the structural change was small and the entropy gain due to desolvation was large in this system. It is also suggested that the factor that clay minerals form such ideal space is due to the rigid structure of clay minerals and is due to many water molecules covering the clay surface. These findings are beneficial and attractive for constructing a more robust host-guest system.

4.5. References

1. Tahir, S. S.; Rauf, N. Removal of a Cationic Dye from Aqueous Solutions by Adsorption onto Bentonite Clay. *Chemosphere* **2006**, *63*, 1842–1848.
2. Bhatt, A. S.; Sakaria, P. L.; Vasudevan, M.; Pawar, R. R.; Sudheesh, N.; Bajaj, H. C.; Mody, H. M. Adsorption of an Anionic Dye from Aqueous Medium by Organoclays: Equilibrium Modeling, Kinetic and Thermodynamic Exploration. *RSC Adv.* **2012**, *2*, 8663–8671.
3. Ghosh, D.; Bhattacharyya, K. G. Adsorption of Methylene Blue on Kaolinite. *Appl. Clay Sci.* **2002**, *20*, 295–300.
4. Bhattacharyya, K. G.; SenGupta, S.; Sarma, G. K. Interactions of the Dye, Rhodamine B with Kaolinite and Montmorillonite in Water. *Appl. Clay Sci.* **2014**, *99*, 7–17.
5. Ma, Y.; Xu, Z.; Guo, T.; You, P. Adsorption of Methylene Blue on Cu(II)-exchanged Montmorillonite. *J. Colloid Interface Sci.* **2004**, *280*, 283–288.
6. Castellini, E.; Andreoli, R.; Malavasi, G.; Pedone, A. Deflocculant Effects on the Surface Properties of Kaolinite Investigated Through Malachite Green Adsorption. *Colloids Surf. A Physicochem. Eng. Asp.* **2008**, *329*, 31–37.
7. Günay, A.; Ersoy, B.; Dikmen, S.; Evcin, A. Investigation of Equilibrium, Kinetic, Thermodynamic and Mechanism of Basic Blue 16 Adsorption by Montmorillonitic Clay. *Adsorption* **2013**, *19*, 757–768.
8. Rodríguez, A.; Ovejero, G.; Mestanza, M.; García, J. Removal of Dyes from Wastewaters by Adsorption on Sepiolite and Pansil. *Ind. Eng. Chem. Res.* **2010**, *49*, 3207–3216.
9. Leffler, J. E. The Interpretation of Enthalpy and Entropy Data. *J. Org. Chem.* **1966**, *31*,

533–537.

10. Grunwald, E.; Steel, C. Solvent Reorganization and Thermodynamic Enthalpy-Entropy Compensation. *J. Am. Chem. Soc.* **1995**, *117*, 5687-5692.

11. Linert, W.; Han, F. L.; Lukovits, I. The Use of the Isokinetic Relationship and Molecular Mechanics to Investigate Molecular Interactions in Inclusion Complexes of Cyclodextrins. *Chem. Phys*. **1989**, *139*, 441-455.

12. Danil de Namor, A. F.; Tanaka, D. A. P.; Regueira, L. N.; Orellana, I. G. Effect of β-cyclodextrin on the Transfer of N1-substituted Sulfonamides from Water to Chloroform. *J. Chem. Soc., Faraday Trans.* **1992**, *88*, 1665-1668.

13. Rekharsky, M. V.; Inoue, Y. Complexation Thermodynamics of Cyclodextrins. *Chem. Rev.* **1998**, *98*, 1875–1917.

14. Liu, Y.; Tong, L. H.; Tian, B. Z. Complexation Thermodynamics of Bis(crown ether)s. 4. Calorimetric Titration of Intramolecular Sandwich Complexation of Thallium and Sodium Ions with Bis(15-crown-5)s and Bis(12-crown-4)s: Enthalpy-Entropy Compensation. *J. Phys. Chem.* **1990**, *94*, 2666–2670.

15. Inoue, Y.; Wada, T. *Advances in Supramolecular Chemistry*; Gokel, G. W., Ed.; JAI Press Inc.: Greenwich, CT, 1997; Vol. 4, pp 55–96.

16. Rong, X.; Huang, Q.; He, X.; Chen, H.; Cai, P.; Liang, W. Interaction of *Pseudomonas putida* with Kaolinite and Montmorillonite: A Combination Study by Equilibrium Adsorption, ITC, SEM and FTIR. *Colloids Surf. B Biointerfaces* **2008**, *64*, 49–55.

17. Inoue, Y.; Liu, Y.; Tong, L.; Shen, B.; Jin, D. Calorimetric Titration of Inclusion Complexation with Modified β-Cyclodextrins. Enthalpy-Entropy Compensation in Host-Guest Complexation: From Ionophore to Cyclodextrin and Cyclophane. *J. Am.*

Chem. Soc. **1993**, *115*, 10637–10644.

18. Inoue, Y.; Hakushi, T. Enthalpy-entropy Compensation in Complexation of Cations with Crown Ether and Related Ligands. *J. Chem. Soc., Perkin Trans*. 2 **1985**, 935–946.
19. Wada, K.; Mizutani, T.; Matsuoka, H.; Kitagawa, S. A New Strategy for the Design of Water-Soluble Synthetic Receptors: Specific Recognition of DNA Intercalators and Diamines. *Chem. Eur. J.* **2003**, *9*, 2368–2380.
20. Inoue, Y.; Hakushi, T.; Liu, Y.; Tong, L. H.; Shen, B.; Jin, D. Thermodynamics of Molecular Recognition by Cyclodextrins. 1. Calorimetric Titration of Inclusion Complexation of Naphthalenesulfonates with α-, β-, and γ-Cyclodextrins: Enthalpy-Entropy Compensation. *J. Am. Chem. Soc.* **1993**, *115*, 475–481.
21. Almeida, C. A. P.; Debacher, N. A.; Downs, A. J.; Cottet, L.; Mello, C. A. D. Removal of Methylene Blue from Colored Effluents by Adsorption on Montmorillonite Clay. *J. Colloid Interface Sci.* **2009**, *332*, 46–53.
22. Wang, G.; Wang, S.; Sun, Z.; Zheng, S.; Xi, Y. Structures of Nonionic Surfactant Modified Montmorillonites and Their Enhanced Adsorption Capacities Towards a Cationic Organic Dye. *Appl. Clay Sci.* **2017**, *148*, 1–10.
23. Bulut, E.; Özacar, M.; Şengil, İ. A. Adsorption of Malachite Green onto Bentonite: Equilibrium and Kinetic Studies and Process Design. *Microporous Mesoporous Mater.* **2008**, *115*, 234–246.
24. Bayram, T.; Bucak, S.; Ozturk, D. BR13 Dye Removal Using Sodium Dodecyl Sulfate Modified Montmorillonite: Equilibrium, Thermodynamic, Kinetic and Reusability Studies. *Chem. Eng. Process.* **2020**, *158*, 108186–108198.
25. Reinert, L.; Batouche, K.; Lévêque, J.; Muller, F.; Bény, J.; Kebabi, B.; Duclaux, L.

Adsorption of Imidazolium and Pyridinium Ionic Liquids onto Montmorillonite: Characterization and Thermodynamic Calculations. *Chem. Eng. J.* **2012**, *209*, 13–19.

26. Xiao, F.; Yan, B.; Zou, X.; Cao, X.; Dong, L.; Lyu, X.; Li, L.; Qiu, J.; Chen, P.; Hu, S.; Zhang, Q. Study on Ionic Liquid Modified Montmorillonite and Molecular Dynamics Simulation. *Colloids Surf. A Physicochem. Eng. Asp.* **2020**, *587*, 124311–124321.

27. Elsherbiny, A. S.; Salem, M. A.; Ismail, A. A. Influence of the Alkyl Chain Length of Cyanine Dyes on Their Adsorption by Na^{+}-montmorillonite from Aqueous Solutions. *Chem. Eng. J.* **2012**, *200-202*, 283–290.

28. Chang, P.; Jiang, W.; Li, Z.; Kuo, C.; Jean, J.; Chen, W.; Lv, G. Mechanism of Amitriptyline Adsorption on Ca-montmorillonite (SAz-2). *J. Hazard. Mater.* **2014**, *277*, 44–52.

29. Huang, Z.; Li, Y.; Chen, W.; Shi, J.; Zhang, N.; Wang, X.; Li, Z.; Gao, L.; Zhang, Y. Modified Bentonite Adsorption of Organic Pollutants of Dye Wastewater. *Mater. Chem. Phys.* **2017**, *202*, 266–276.

30. Fabryanty, R.; Valencia, C.; Soetaredjo, F. E.; Putro, J. N.; Santoso, S. P.; Kurniawan, A.; Ju, Y.; Ismadji, S. Removal of Crystal Violet Dye by Adsorption Using Bentonite-Alginate Composite. *J. Environ. Chem. Eng.* **2017**, *5*, 5677–5687.

31. Arellano-Cárdenas, S.; López-Cortez, S.; Cornejo-Mazón, M.; Mares-Gutiérrez, J. C. Study of Malachite Green Adsorption by Organically Modified Clay Using a Batch Method. *Appl. Surf. Sci.* **2013**, *280*, 74–78.

32. Hong, S.; Wen, C.; He, J.; Gan, F.; Ho, Y. Adsorption Thermodynamics of Methylene Blue onto Bentonite. *J. Hazard. Mater.* **2009**, *167*, 630–633.

33. Turabik, M. Adsorption of Basic Dyes from Single and Binary Component Systems

onto Bentonite: Simultaneous Analysis of Basic Red 46 and Basic Yellow 28 by First Order Derivative Spectrophotometric Analysis Method. *J. Hazard. Mater.* **2008**, *158*, 52–64.

34. Eren, E.; Afsin, B. Investigation of a Basic Dye Adsorption from Aqueous Solution onto Raw and Pre-treated Bentonite Surfaces. *Dyes Pigm.* **2008**, *76*, 220–225.

35. Çakmak, M.; Taşar, Ş.; Selen, V.; Özer, D.; Özer, A. Removal of Astrazon Golden Yellow 7GL from Colored Wastewater Using Chemically Modified Clay. *J. Cent. South Univ.* **2017**, *24*, 743–753.

36. Khenifi, A.; Bouberka, Z.; Sekrane, F.; Kameche, M.; Derriche, Z. Adsorption Study of an Industrial Dye by an Organic Clay. *Adsorption* **2007**, *13*, 149–158.

37. Seki, Y.; Yurdakoç, K. Adsorption of Promethazine Hydrochloride with KSF Montmorillonite. *Adsorption* **2006**, *12*, 89–100.

38. Mazloomi, F.; Jalali, M. Adsorption of Ammonium from Simulated Wastewater by Montmorillonite Nanoclay and Natural Vermiculite: Experimental Study and Simulation. *Environ. Monit. Assess.* **2017**, *189*, 415.

39. Hosseinzadeh, H.; Zoroufi, S.; Mahdavinia, G. R. Study on Adsorption of Cationic Dye on Novel *kappa*-Carrageenan/Poly(vinyl alcohol)/Montmorillonite Nanocomposite Hydrogels. *Polym. Bull.* **2015**, *72*, 1339–1363.

40. Hasani, S.; Doulati Ardejani, F.; Olya, M. E. Equilibrium and Kinetic Studies of Azo Dye (Basic Red 18) Adsorption onto Montmorillonite: Numerical Simulation and Laboratory Experiments. *Korean J. Chem. Eng.* **2017**, *34*, 2265–2274.

41. Khankhasaeva, S. T.; Dashinamzhilova, E. T.; Badmaeva, S. V.; Bardamova, A. L. Adsorption of Triarylmethane Dye on Ca-Montmorillonite: Equilibrium, Kinetics, and

Thermodynamics. *Colloid J.* **2018**, *80*, 453–458.

42. Boudouara, K.; Ghelamallah, M.; Benzaoui, K. Kinetic and Equilibrium Studies of Methyl Violet Adsorption from Aqueous Solutions by Activated Algerian Bentonite Clay. *Arab. J. Geosci.* **2019**, *12*, 459.

43. Mekatel, E.; Amokrane, S.; Trari, M.; Ferhat, D.; Aid, A.; Nibou, D. Removal of Basic Red 46 Dye from Aqueous Solution by Adsorption and Photocatalysis: Equilibrium, Isotherms, Kinetics, and Thermodynamic Studies. *Sep. Sci. Technol.* **2020**, *55*, 867–885.

44. Karaer, H.; Bulut, Y. Adsorption of Methylene Blue from Aqueous Solution by Crosslinked Chitosan/Bentonite Composite. *J. Dispers. Sci. Technol.* **2015**, *36*, 61–67.

45. Arabkhani, P.; Asfaram, A.; Ateia, M. Easy-to-prepare Graphene Oxide/Sodium Montmorillonite Polymer Nanocomposite with Enhanced Adsorption Performance. *J. Water Process. Eng.* **2020**, *38*, 101651.

46. Dotto, G. L.; Rodrigues, F. K.; Tanabe, E. H.; Fröhlich, R.; Bertuol, D. A.; Martins, T. R.; Foletto, E. L. Development of Chitosan/Bentonite Hybrid Composite to Remove Hazardous Anionic and Cationic Dyes from Colored Effluents. *J. Environ. Chem. Eng.* **2016**, *4*, 3230–3239.

47. Foroutan, R.; Mohammadi, R.; MousaKhanloo, F.; Sahebi, S.; Ramavandi, B.; Senthil Kumar, P.; Vardhan, K. H. Performance of Montmorillonite/Graphene Oxide/$CoFe_2O_4$ as a Magnetic and Recyclable Nanocomposite for Cleaning Methyl Violet Dye-laden Wastewater. *Adv. Powder Technol.* **2020**, *31*, 3993–4004.

48. Rezala, H.; Douba, H.; Boukhatem, H.; Romero, A. Adsorption of Methylene Blue by Hydroxyl-Aluminum Pillared Montmorillonite. *J. Chem. Soc. Pak.* **2020**, *42*, 550–563.

49. Joudi, M.; Nasserlah, H.; Hafdi, H.; Mouldar, J.; Hatimi, B.; El Mhammedi, M. A.;

Bakasse, M. Synthesis of an Efficient Hydroxyapatite–Chitosan–Montmorillonite Thin Film for the Adsorption of Anionic and Cationic Dyes: Adsorption Isotherm, Kinetic and Thermodynamic Study. *SN Appl. Sci.* **2020**, *2*, 1078.

50. Boudjemaa, S.; Zidelkheir, B. Removal Properties of Methylene Blue from Aqueous Solutions by Organomodified Montmorillonite: Isotherm, Thermodynamics and Kinetic Studies. *Rev. Roum. Chim.* **2020**, *65*, 499–508.

51. Li, Y.; Huang, Z.; Xia, Y.; Shi, J.; Gao, L. Adsorption Equilibrium, Isotherm, Kinetics, and Thermodynamic of Modified Bentonite for Removing Rhodamine B. *Indian J. Chem. Technol.* **2020**, *27*, 116–125.

52. Ma, J.; Lei, Y.; Khan, M. A.; Wang, F.; Chu, Y.; Lei, W.; Xia, M.; Zhu, S. Adsorption Properties, Kinetics & Thermodynamics of Tetracycline on Carboxymethyl-Chitosan Reformed Montmorillonite. *Int. J. Biol. Macromol.* **2019**, *124*, 557–567.

53. Puri, C.; Sumana, G. Highly Effective Adsorption of Crystal Violet Dye from Contaminated Water Using Graphene Oxide Intercalated Montmorillonite Nanocomposite. *Appl. Clay Sci.* **2018**, *166*, 102–112.

54. Uyar, G.; Kaygusuz, H.; Erim, F. B. Methylene Blue Removal by Alginate–Clay Quasi-Cryogel Beads. *React. Funct. Polym.* **2016**, *106*, 1–7.

55. Sharma, P.; Borah, D. J.; Das, P.; Das, M. R. Cationic and Anionic Dye Removal from Aqueous Solution Using Montmorillonite Clay: Evaluation of Adsorption Parameters and Mechanism. *Desalin. Water Treat.* **2016**, *57*, 8372–8388.

56. Cottet, L.; Almeida, C. A. P.; Naidek, N.; Viante, M. F.; Lopes, M. C.; Debacher, N. A. Adsorption Characteristics of Montmorillonite Clay Modified with Iron Oxide with Respect to Methylene Blue in Aqueous Media. *Appl. Clay Sci.* **2014**, *95*, 25–31.

57. Fil, B. A.; Özmetin, C.; Korkmaz, M. Cationic Dye (Methylene Blue) Removal from Aqueous Solution by Montmorillonite. *Bull. Korean Chem. Soc.* **2012**, *33*, 3184–3190.

58. Geyikçi, F. The Equilibrium and Kinetics Studies of Crystal Violet Adsorption onto Montmorillonite. *Environ. Eng. Manag. J.* **2012**, *11*, 733–740.

59. Elaziouti, A.; Laouedj, N. Effects of pH and Temperature on the Adsorption of Cationic Dyes from Aqueous Suspension by Maghnia Montmorillonite. *J. Korean Chem. Soc.* **2011**, *55*, 208–217.

60. Ai, L.; Zhou, Y.; Jiang, J. Removal of Methylene Blue from Aqueous Solution by Montmorillonite/$CoFe_2O_4$ Composite with Magnetic Separation Performance. *Desalination* **2011**, *266*, 72–77.

61. Bouberka, Z.; Khenifi, A.; Benderdouche, N.; Derriche, Z. Removal of Supranol Yellow 4GL by Adsorption onto Cr-Intercalated Montmorillonite. *J. Hazard. Mater.* **2006**, *133*, 154–161.

62. Li, Z.; Potter, N.; Rasmussen, J. Removal of Rhodamine 6G with Different Types of Clay Minerals. *Chemosphere* **2018**, *202*, 127–135.

63. Tekin, N.; Demirbaş, Ö.; Alkan, M. Adsorption of Cationic Polyacrylamide onto Kaolinite. *Microporous Mesoporous Mater.* **2005**, *85*, 340–350.

64. Asuha, S.; Fei, F.; Wurendaodi, W. Activation of Kaolinite by a Low-Temperature Chemical Method and its Effect on Methylene Blue Adsorption. *Powder Technol.* **2020**, *361*, 624–632.

65. Khan, T. A.; Dahiya, S. Use of Kaolinite as Adsorbent: Equilibrium, Dynamics and Thermodynamic Studies on the Adsorption of Rhodamine B from Aqueous Solution. *Appl. Clay Sci.* **2012**, *69*, 58–66.

66. Gao, W.; Zhao, S. Direct Acid Activation of Kaolinite and its Effects on the Adsorption of Methylene Blue. *Appl. Clay Sci.* **2016**, *126*, 98–106.

67. Tehrani-Bagha, A. R.; Nikkar, H. The Sorption of Cationic Dyes onto Kaolin: Kinetic, Isotherm and Thermodynamic Studies. *Desalination* **2011**, *266*, 274–280.

68. Nandi, B. K.; Goswami, A. K. Removal of Cationic Dyes from Aqueous Solutions by Kaolin: Kinetic and Equilibrium Studies. *Appl. Clay Sci.* **2009**, *42*, 583–590.

69. Issa, A. A.; Al-Degs, Y. S. Studying Competitive Sorption Behavior of Methylene Blue and Malachite Green Using Multivariate Calibration. *Chem. Eng. J.* **2014**, *240*, 554–564.

70. Suwandi, A. C.; Indraswati, N. Adsorption of N-methylated Diaminotriphenilmethane Dye (Malachite Green) on Natural Rarasaponin Modified Kaolin. *Desalin. Water Treat.* **2012**, *41*, 342–355.

71. Sarma, G. K.; SenGupta, S. Removal of Hazardous Basic Dyes from Aqueous Solution by Adsorption onto Kaolinite and Acid-treated Kaolinite: Kinetics, Isotherm and Mechanistic Study. *SN Appl. Sci.* **2019**, *1*, 211.

72. Karim, A. B.; Mounir, B. Removal of Basic Red 46 Dye from Aqueous Solution by Adsorption onto Moroccan Clay. *J. Hazard. Mater.* **2009**, *168*, 304–309.

73. Aragaw, T. A.; Angerasa, F. T. Synthesis and Characterization of Ethiopian Kaolin for the Removal of Basic Yellow (BY 28) Dye from Aqueous Solution as a Potential Adsorbent. *Heliyon* **2020**, *6*, e04975.

74. Meigoli, B. M.; Esmaeili, H. Ultrasonic Assisted Synthesis of Kaolin/$CuFe_2O_4$ Nanocomposite for Removing Cationic Dyes from Aqueous Media. *J. Environ. Chem. Eng.* **2020**, *8*, 103869.

75. Lellou, S.; Kadi, S. Study of Methylene Blue Adsorption by Modified Kaolinite by Dimethyl Sulfoxide. *Ecol. Chem. Eng. S* **2020**, *27*, 225–239.

76. Sargin, İ.; Ünlü, N. Insights into Cationic Methyl Violet 6B Dye–Kaolinite Interactions: Kinetic, Equilibrium and Thermodynamic Studies. *Clay Miner.* **2013**, *48*, 85–95.

77. Fukushima, Y. X-Ray Diffraction Study of Aqueous Montmorillonite Emulsions. *Clays Clay Miner.* **1984**, *32*, 320–326.

78. Urabe, K.; Sakurai, H. Cation-exchanged Synthetic Saponite as a 'Heat-stable' Acidic Clay Catalyst. *J. Chem. Soc., Chem. Commun.* **1988**, 1520–1521.

79. Serratosa, J. M. Infrared Analysis of the Orientation of Pyridine Molecules in Clay. *Clays Clay Miner.* **1966**, *14*, 385–391.

80. Sugahara, Y.; Satokawa, S. Kaolinite-Pyridine Intercalation Compound Derived from Hydrated Kaolinite. *Clays Clay Miner.* **1989**, *37*, 143–150.

81. Ogawa, M.; Hashizume, T. Intercalation of 2,2'-bipyridine and Complex Formation in the Interlayer Space of Montmorillonite by Solid-Solid Reactions. *Inorg. Chem.* **1991**, *30*, 584–585.

82. Norrish, K. The Swelling of Montmorillonite. *Discuss. Faraday Soc.* **1954**, *18*, 120-134.

83. Rao, W.; Piliouras, P.; Wang, X.; Guido, A.; Kugler, K.; Sieren, B.; Wang, L.; Lv, G.; Li, Z. Zwitterionic Dye Rhodamine B (RhB) Uptake on Different Types of Clay Minerals. *Appl. Clay Sci*. **2020**, *197*, 105790–105800.

Chapter 5. Self-Fluorescence Quenching Behavior of Acridinium Derivatives on the Clay Surface

5.1. Introduction

In order to utilize clay minerals in combination with the dye molecules as photo-functional materials, it is necessary to understand the adsorption and photochemical behavior of the dye on the clay surface. Since the adsorption of the molecules on the solid surface is dynamic equilibrium, the molecules are apparently immobilized, while the molecules are not completely immobilized from a microscopic point of view.[1,2] In other words, the constant movement of molecules on the solid surface may cause contact between the molecules.[3–9] The contact between the molecules causes quenching of excited molecules. It is, therefore, a phenomenon that should be avoided in order to utilize it as a photo-functional material. Many molecules are self-quenched even on the clay surface.[10–14] However, it was found that self-quenching was suppressed when the intermolecular positive charge distance of the tetra-cationic porphyrin and the negative charge distance on the clay surface was in good agreement.[15–19] It was shown that increasing the Coulomb force between a cationic porphyrin as a guest molecule and synthetic saponite as a host material is important to suppress self-quenching. If the molecular structure can be controlled, it is possible to form a state in which fluorescence quenching is suppressed even if molecules are adsorbed at high density.

In this chapter, the self-fluorescence quenching behavior of cationic acridinium derivatives on the synthetic saponites was evaluated. As mentioned above, previous research has elucidated that the main factor of the self-fluorescence quenching of the dye molecule adsorbed on the clay surface is the collision between dye molecules and the formation of aggregation.[10–14] The degree of fluorescence quenching is expected to vary depending on whether the dye molecules are uniformly distributed or segregated on the clay surface. First, the diffusion process of the acridinium derivative on the clay surface was evaluated by observing the time-dependent change in fluorescence intensity of the aclidinium derivative adsorbed on the clay surface. Second, the self-quenching behavior of acridinium derivatives on the synthetic saponite was evaluated in a state where the distribution of the aclidinium derivative on the synthetic saponite was stabilized.

5.2. Experimental section

5.2.1. Materials

Clay minerals (synthetic saponites): Sumecton SA (Sap1.2) was purchased from Kunimine Industries Co., Ltd. and was used without further purification. The synthetic saponites, named Sap1.0, Sap1.4, and Sap1.6, were synthesized by hydrothermal synthesis according to a previous paper.[20] The synthetic saponites were analyzed with atomic force microscopy (AFM), X-ray diffraction (XRD), X-ray fluorescence (XRF), and Fourier transform infrared spectroscopy (FT-IR), as described in the previous paper.[20] The general structure and chemical formulas of synthetic saponites are shown in Figure 1.5 and Table 1.4. According to the paper, the cation-exchange capacity (CEC) of Sap1.0, Sap1.2, Sap1.4, and Sap1.6 were 1.32, 0.99, 0.69, and 0.59 mequiv. g^{-1}, respectively.[20] Since the theoretical specific surface

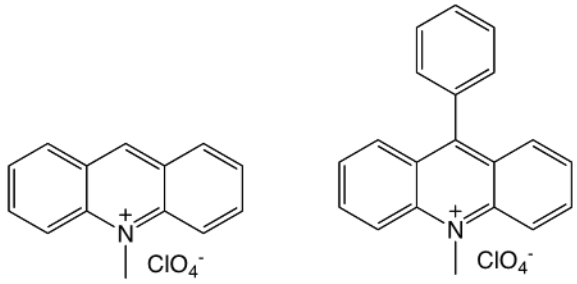

Figure 5.1. Structures of acridinium derivatives.

area of the synthetic saponite is 750 nm^2 g^{-1}, the negative-charge distances of Sap1.0, Sap1.2, Sap1.4, and Sap1.6 were calculated to be 1.04, 1.20, 1.45, and 1.57 nm on the basis of a hexagonal array, respectively. The aqueous dispersion of synthetic saponites, whose particle size is 100 nm or less, is substantially transparent in the UV-visible range. Water was deionized with an ORGANO BB-5A system (PF filter ×2 + G-10 column). 9-Phenyl-10-methylacridinium perchlorate was purchased from Tokyo Kasei. 10-Methylacridinium methyl sulfate was purchased from Aldrich. The counter ion was exchanged to perchlorate with an ion-exchange resin (Organo, Amberlite Resin IRA-400 treated with $HClO_4$).

5.2.2. Analysis

TG-DTA curves were measured with Shimadzu DTG-60H analyzer to determine the water content of acridinium derivatives and synthetic saponites. The temperature was ramped from room temperature to 120°C with a heating rate of 10°C/min under dry air as a purge gas and was held for 60 minutes. Absorption spectra were obtained on a UV-3150 UV-vis. spectrophotometer (SHIMADZU). Fluorescence spectra were obtained on an FP-6500 spectrofluorometer (Jasco), and the excitation light was set at the maximum absorption wavelength of each sample. The reproducibility and signal-to-noise ratio of the fluorescence

intensity is 0.5% and 100:1 or higher. Fluorescence lifetimes were measured by a C4780 picosecond fluorescence lifetime measurement system (Hamamatsu Photonics). An Nd^{3+} YAG laser (EKSPLA PL2210JE + PG-432, fwhm 25 ps, 1 kHz) was used for excitation. The excitation wavelength was 355 nm. The fluorescence lifetimes were calculated by deconvoluting the excitation pulse in each measurement range.

5.2.3. Sample preparation

Stock solutions of acridinium derivatives were prepared in a concentration range of 1.0×10^{-3}–1.0×10^{-4} M. Stock dispersions of synthetic saponites were prepared in a concentration range of 1.0×10^{-3}–1.0×10^{-4} equiv. L^{-1}. In order to prepare acridinium derivative-synthetic saponite complexes, above aqueous stock solutions were mixed at an arbitrary rate and were diluted with water under stirring in a quartz cell (1.0 × 1.0 cm). UV-vis absorption spectra were measured under the concentration of 1×10^{-6} M for acridinium derivatives and 1×10^{-3} equiv. L^{-1} for synthetic saponites. Fluorescence spectra were measured under the concentration of 3.33×10^{-9} M for acridinium derivatives and 2.0×10^{-4}–3.33×10^{-7} equiv. L^{-1} for synthetic saponites. Fluorescence lifetimes were measured under the concentration of 4.0×10^{-8} M for acridinium derivatives and 4.0×10^{-4} equiv. L^{-1} for synthetic saponites.

5.3. Result and discussion

5.3.1. Kinetics of adsorption of acridinium derivatives on synthetic saponites

It was evaluated how acridinium derivatives move on and between the clay surface after adsorption. When the dye molecules are adsorbed on the clay surface, it is presumed that the dye molecules undergo three processes: (i) adsorption on the clay surface, (ii) movement within the clay surface, and (iii) movement between the clay nanosheet. Since the absorption spectra

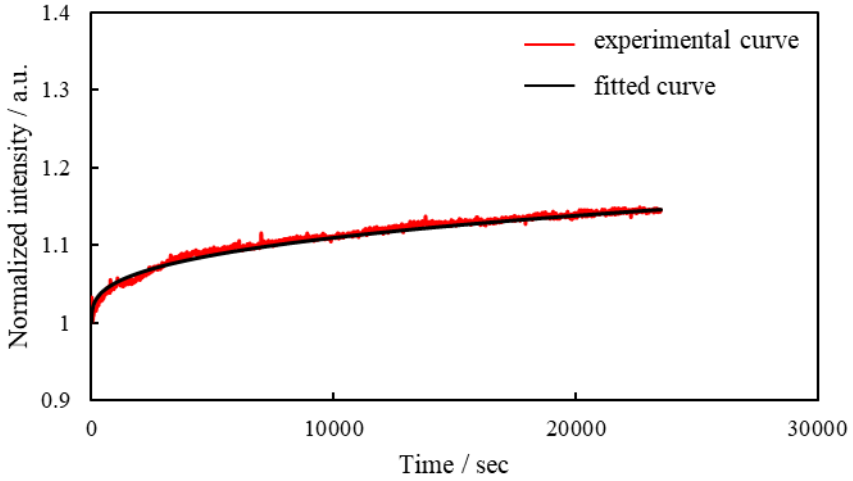

Figure 5.2. Fluorescence intensity profile of Acr^+ on Sap1.2. $[Acr^+] = 3.33\times10^{-9}$ M, [Sap1.2] = 3.33×10^{-5} equiv. L^{-1}. The dye loading levels were 0.010% vs. CEC of the clay. The excitation wavelength was 355 nm.

of the dye molecule change immediately due to the mixing of the dye solution and clay dispersion, it is suggested that the process (i) is very fast. In order to evaluate the process of ii) and iii), synthetic saponite dispersion was added to the solution of acridinium derivative/synthetic saponite complex whose adsorption state was stabilized at 10% vs. CEC to make it 0.01% vs. CEC, and the time transition in its fluorescence intensity was measured. When synthetic saponite was added at 0.01% vs. CEC, the fluorescence intensity increased and saturated in 20000 sec, as shown in Figure 5.2. The rate constants were evaluated by the stretched exponential function in order to evaluate the processes ii) and iii) included in the time transition of fluorescence intensity shown in Figure 5.2. The stretched exponential function can be expressed as in equation (5.1).

$$I = I_0 \cdot exp\left[(-kt)^{\beta}\right] \tag{5.1}$$

where I is the fluorescence intensity, I_0 is the initial fluorescence intensity, k is the rate constant, and β is the stretching exponent. The stretched exponential function can be used to describe

various physical processes.[21–26] As a result of fitting by the nonlinear least-squares method, it was fitted with one component, and k and β were 7.7×10^{-8} s^{-1} and 0.316, respectively. As mentioned above, since the absorption spectrum of dye molecules changes immediately after dye solution is mixed with clay dispersion, process i) is considered to be a very fast process. Therefore, the process i) can be neglected in the time transition of fluorescence intensity shown in Figure 5.2. As the state immediately after i), the dye on the clay is assumed to be either uniformly distributed or segregated. The fluorescence intensity increased with time, suggesting that the fluorescence self-quenching was gradually canceled. In other words, it was suggested that the frequency of collisions between molecules decreased. Therefore, the increase in fluorescence intensity with time indicated that the dye gradually moved from a segregated distribution to a uniform distribution. The rate constant was expressed as one component, suggesting that the rates of ii) and iii) were almost equal or that the distribution of dye molecules shifted to a homogeneous adsorption state by the process of iii) without going through the process of ii). Because it was found that the fluorescence intensity of acridinium derivatives and synthetic saponite takes about 6 hours to stabilize, the fluorescence spectra after section 5.2 were measured after 6 hours of sample preparation.

5.3.2. Self-quenching of acridinium derivatives on synthetic saponites

As mentioned above, the required time for the adsorption state of acridinium derivatives on the synthetic saponite to stabilize was clarified. This section evaluated the self-fluorescence quenching behavior of acridinium derivatives on various synthetic saponites by steady-state fluorescence spectra. The loading level of acridinium derivatives vs. CEC of the synthetic saponites was controlled by changing the concentration of the synthetic saponites.

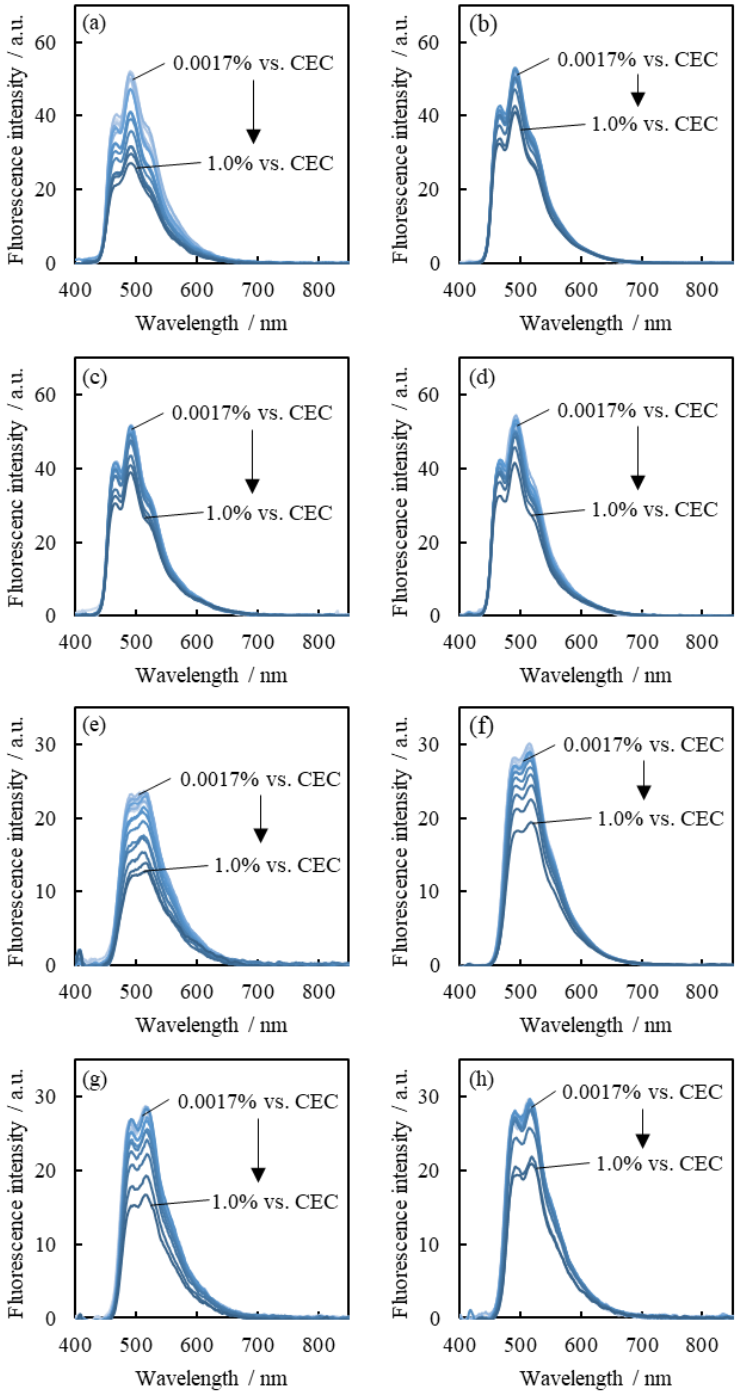

Figure 5.3. Fluorescence spectra of acridinium derivatives-synthetic saponites complexes: (a) Acr^+/Sap1.0, (b) Acr^+/Sap1.2, (c) Acr^+/Sap1.4, (d) Acr^+/Sap1.6 (e) $PhAcr^+$/Sap1.0, (f) $PhAcr^+$/Sap1.2, (g) $PhAcr^+$/Sap1.4, and (h) $PhAcr^+$/Sap1.6 in water. [acridinium derivatives] = 3.33×10^{-9} M, [synthetic saponites] = 2.0×10^{-4}–3.33×10^{-7} equiv. L^{-1}. The dye loading levels were 0.0017, 0.0024, 0.0032, 0.0048, 0.0075, 0.010, 0.017, 0.025, 0.033, 0.050, 0.075, 0.10, 0.25, 0.50 and 1.0% vs. CEC of the clay. The excitation wavelength was 360 nm.

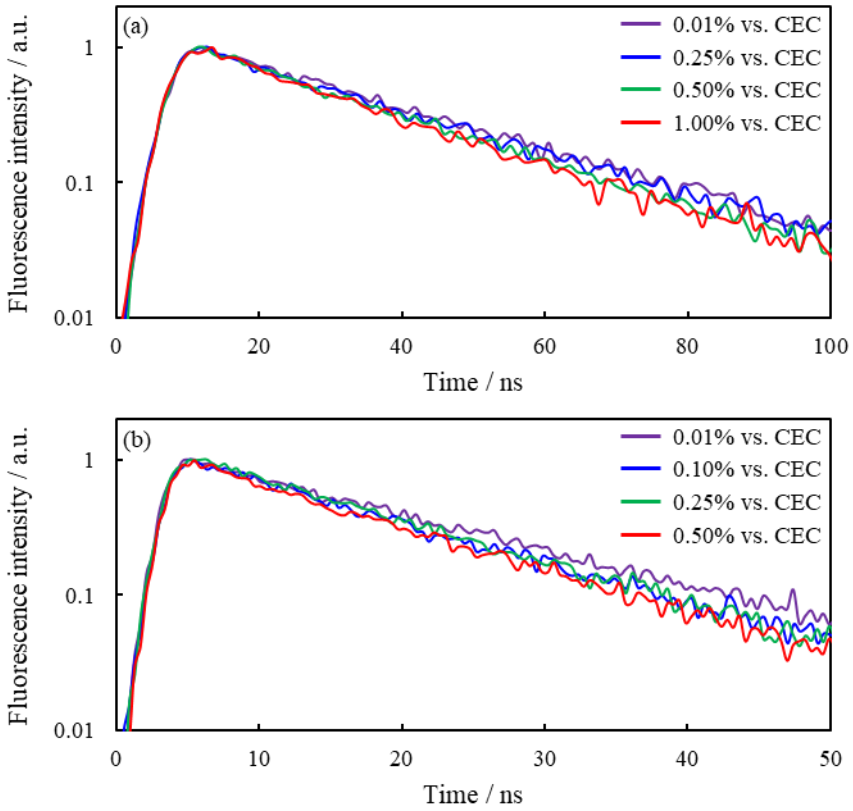

Figure 5.4. Fluorescence decay profiles for (a) Acr^+ and (b) $PhAcr^+$ with and without Sap1.2 in water. [acridinium derivatives] = 3.33×10^{-9} M, [synthetic saponites] = 2.0×10^{-4}–3.33×10^{-7} equiv. L^{-1}. The dye loading levels were 0.010, 0.10, 0.25, 0.50, and 1.0% vs. CEC of the clay. The excitation wavelength was 355 nm.

The steady-state fluorescence spectra of Acr^+ and $PhAcr^+$ at each loading level on various synthetic saponites are shown in Figure 5.3. The fluorescence intensity decreased as the loading level of acridinium derivatives increased. i) The dynamic quenching due to the collision at excited state and ii) the static quenching due to the interaction at ground state are proposed as the factor of decrease in the fluorescence intensity. The factor of self-fluorescence quenching of acridinium derivatives on the synthetic saponite was investigated. When the fluorescence quenching is dynamic, a shorter fluorescence lifetime is observed. On the other hand, the fluorescence lifetime does not change when the fluorescence quenching is

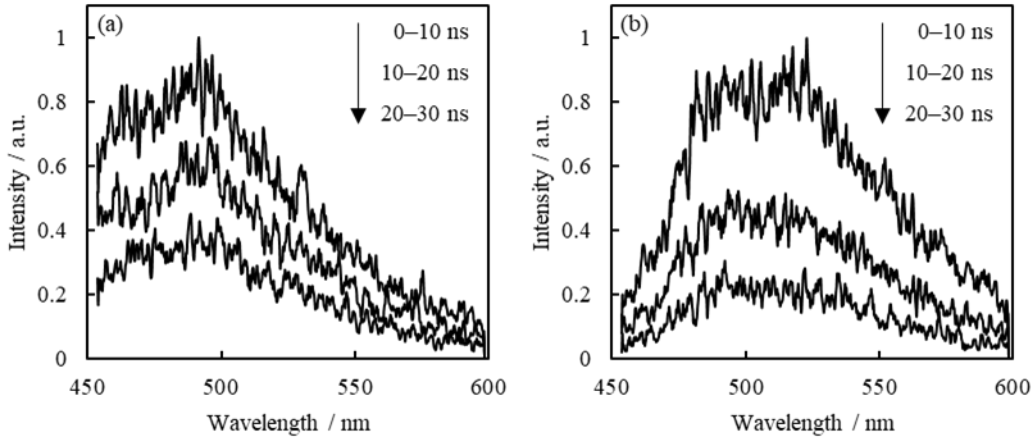

Figure 5.5. The typical time-resolved fluorescence spectra of acridinium derivatives-synthetic saponites complexes: (a) Acr^+/Sap1.2 and (b) $PhAcr^+$/Sap1.2 in water. [acridinium derivatives] = 3.33×10^{-9} M, [synthetic saponites] = $–3.33\times10^{-5}$ equiv. L^{-1}. The dye loading levels were 0.010% vs. CEC of the clay. The excitation wavelength was 355 nm.

static.[6–9,12] The fluorescence lifetimes of acridinium derivatives on synthetic saponites at each loading level were observed. Figure 5.4 shows the fluorescence decay curves of the complexes of Acr^+ and $PhAcr^+$ with Sap1.2 at various loading levels. As shown in Figure 5.4, all profiles can be analyzed as single exponential decays, indicating that all acridinium derivatives adsorbed on the synthetic saponites have almost the same surrounding conditions. Whereas the fluorescence lifetime of dye molecules on the solid surfaces tends to be complicated due to aggregation formation, it was suggested that the present system did not form the aggregation. In addition, the typical time-resolved fluorescence spectra of Acr^+ and $PhAcr^+$ with sap1.2 are shown in Figure 5.5. The fluorescence spectral shapes during the decay were completely the same, indicating that the present system did not form the aggregation.[17]

A decrease in fluorescence lifetime was observed as the loading level increased. The

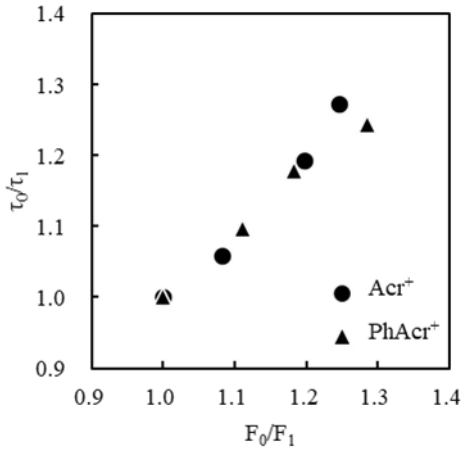

Figure 5.6. Relationship between the decrease ratio of lifetimes (τ_0/τ_1) and those of steady-state fluorescence intensities (I_0/I_1) due to the fluorescence quenching.

fluorescence lifetime when not self-quenched (τ_0) and the fluorescence lifetime when self-quenched (τ_1) are represented by using deactivation rate constants as shown in Eq. (5.2) and Eq. (5.3).

$$\tau_0 = \frac{1}{k_f + k_{nr}} \tag{5.2}$$

$$\tau_1 = \frac{1}{k_f + k_{nr} + k_{SQ}} \tag{5.3}$$

where k_f is the radiative deactivation rate constant, k_{nr} is the sum of nonradiative deactivation rate constant, and k_{SQ} is the self-fluorescence quenching rate constant. The fluorescence quantum yield when not self-quenched (Φ_0) and the fluorescence quantum yield when self-quenched (Φ_1) is represented by using deactivation rate constants as shown in Eq. (5.4) and Eq.(5.5)

$$I_0 = \frac{k_f}{k_f + k_{nr}} \tag{5.4}$$

$$I_1 = \frac{k_f}{k_f + k_{nr} + k_{SQ}} \tag{5.5}$$

Eq. (5.6) is obtained by dividing Eq. (5.2) by Eq. (5.3).

$$\frac{\tau_0}{\tau_1} = 1 + \frac{k_{SQ}}{k_f + k_{nr}} \tag{5.6}$$

Eq. (5.7) is obtained by dividing Eq. (5.4) by Eq. (5.5).

$$\frac{I_0}{I_1} = 1 + \frac{k_{SQ}}{k_f + k_{nr}} \tag{5.7}$$

If static quenching is included in this system, the values of τ_0/τ_1 and I_0/I_1 do not match. The decreased ratios of fluorescence intensities were compared with those of fluorescence lifetimes to evaluate the ratio of dynamic quenching and static quenching. Figure 5.6 shows the plots of τ_0/τ_1 vs. I_0/I_1. The slope of the plot of τ_0/τ_1 vs. I_0/I_1 were almost 1 for both Acr^+ and $PhAcr^+$, indicating that the ratio of decrease in the lifetime (τ_0/τ_1) and the rate of decrease in fluorescence intensity (I_0/I_1) were almost the same. It can thus be suggested that the self-fluorescence quenching of aclidinium derivatives on synthetic saponite is only dynamic quenching, not static quenching.

5.3.3. Adsorption state without self-fluorescence quenching

As mentioned above, it was indicated that the self-fluorescence quenching of acridinium derivatives on the synthetic saponite was dynamic. It suggests that the collision at the excited state causes fluorescence quenching on the synthetic saponite. This section evaluated the correlation between the fluorescence quenching and the distance between acridinium derivatives on the synthetic saponite.

The relationship between loading level and fluorescence intensity derived from the fluorescence spectra of Figure 5.3 was shown in Figure 5.8. The fluorescence quenching was observed at higher loading levels, regardless of the type of synthetic saponites and acridinium derivatives. The larger the distance between the negative charges of the synthetic saponite, the higher the loading level at which the fluorescence quenching started. However, when the loading level was converted to the average intermolecular distance, the intermolecular

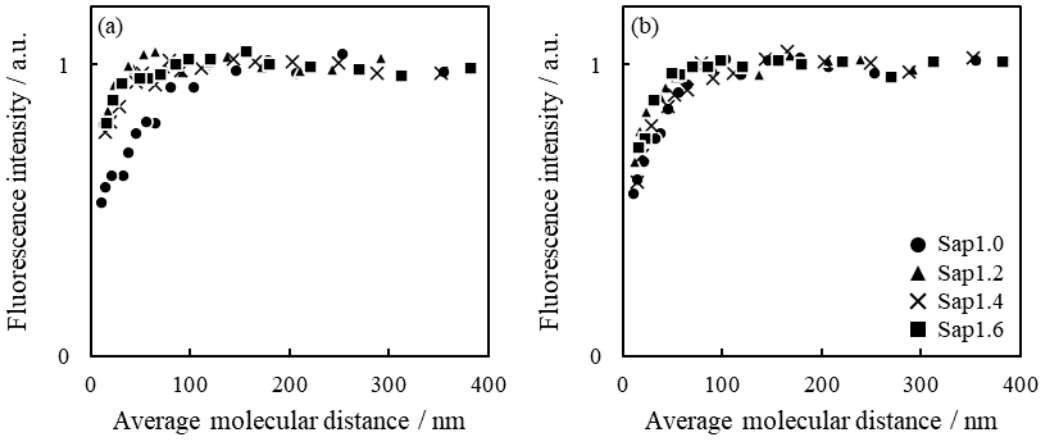

Figure 5.8. Relationship between the theoretical average molecular distances and the fluorescence intensities of acridinium derivatives; (a) Acr^+ (b) $PhAcr^+$

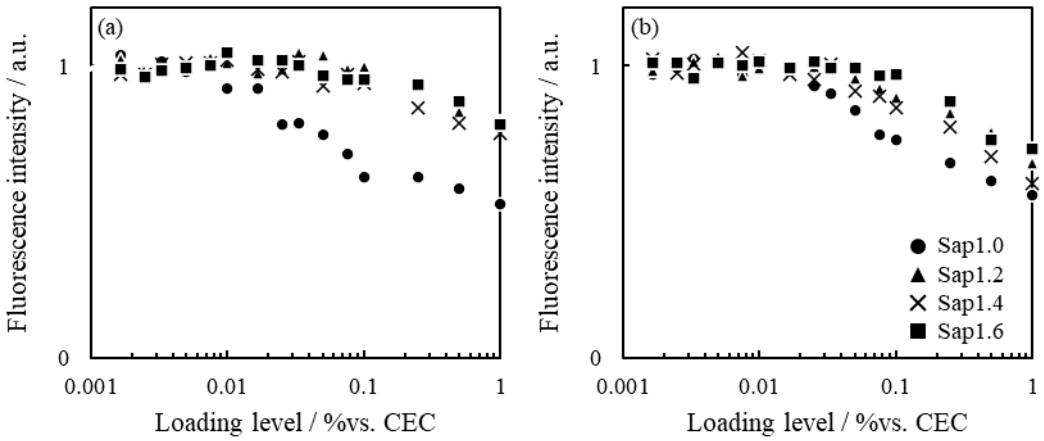

Figure 5.8. Relationship between the loading level of synthetic saponites and the fluorescence intensities of acridinium derivatives; (a) Acr^+ (b) $PhAcr^+$

distances at which fluorescence quenching started were almost 50–100 nm regardless of the negative charge distance of the synthetic saponite (Figure 5.8). The particle size of synthetic saponite is generally about 50 nm.[20] When the distance between adsorbed molecules is more than 50 nm, the number of molecules on one synthetic saponite particle is less than one. Therefore, it is crucial to eliminate the segregation of dye molecules on the clay surface and establish a state in which the number of dye molecules is one or less per clay to suppress the self-fluorescence quenching of mono-cationic dyes.

5.4. Conclusion

This chapter evaluated the behavior of self-fluorescence quenching of mono-cationic acridinium derivatives on the clay surface to clarify the suitable adsorption state for mono-cationic dyes. The diffusion process of the acridinium derivatives on the clay surface was evaluated by observing the time transition of fluorescence intensity from immediately after the acridinium derivatives were adsorbed on the clay surface until stabilization. It was suggested that the migration rates within clay nanosheet of dye molecules and that between clay nanosheet were almost equal, or that dye molecules shifted to a homogeneous adsorption state by migration within clay nanosheet without going through migration between clay nanosheet. It was found that the fluorescence intensity of acridinium derivatives and synthetic saponite takes about 6 hours to stabilize.

The self-fluorescence quenching behavior of acridinium derivatives on various synthetic saponite was evaluated by steady-state fluorescence spectra and fluorescence lifetime measurements. It can thus be suggested that the self-fluorescence quenching of aclidinium derivatives on synthetic saponite is only dynamic, not static.

Finally, the correlation between the fluorescence quenching and the distance between acridinium derivatives on the synthetic saponite was evaluated. When the loading level was converted to the average intermolecular distance, the intermolecular distances at which fluorescence quenching started were almost 50–100 nm regardless of the negative charge distance of the synthetic saponite. This result suggested that it is important to eliminate the segregation of dye molecules on the clay surface and establish a state in which the number of dye molecules is one or less per clay to suppress the self-fluorescence quenching of mono-cationic dyes.

5.5. References

1. Langmuir, I. The Constitution and Fundamental Properties of Solids and Liquids. Part I. Solids. *J. Am. Chem. Soc*. **1916**, *38*, 2221-2295.
2. Langmuir, I. The Constitution and Fundamental Properties of Solids and Liquids. Part II. Liquids. *J. Am. Chem. Soc.* **1917**, *39*, 1848-1906.
3. Evans, T. R. Singlet Quenching Mechanisms. *J. Am. Chem. Soc*. **1971**, *93*, 2081-2082.
4. Nagai, K.; Nishijima, T.; Takamiya, N.; Tada, M.; Kaneko, M. Charge Transfer from Donor to Photoexcited $Ru(bpy)_3^{2+}$ in Solution and Polymer Matrix. *J. Photochem. Photobiol. A* **1995**, *92*, 47-51.
5. Zhang, B.; Zhang, Y.; Mallapragada, S. K.; Clapp, A. R. Sensing Polymer/DNA Polyplex Dissociation Using Quantum Dot Fluorophores. *ACS Nano* **2011**, *5*, 129-138.
6. Phillips, R. L.; Kim, I. B.; Tolbert, L. M.; Brunz, U. H. Fluorescence Self-Quenching of a Mannosylated Poly(*p*-phenyleneethynylene) Induced by Concanavalin A. *J. Am. Chem. Soc*. **2008**, *130*, 6952-6954.

7. Sohmiya, M.; Ogawa, M. Controlled Spatial Distribution of Tris(2,2′-bipyridine)ruthenium Cation ($[Ru(bpy)_3]^{2+}$) in Aluminum Containing Mesoporous Silicas. *Microporous Mesoporous Mater*. **2011**, *142*, 363-370.
8. Boulu, L. G.; Patterson, L. K.; Chauvet, J. P.; Kozak, J. J. Theoretical Investigation of Fluorescence Concentration Quenching in Two-Dimensional Disordered Systems. Application to Chlorophyll a in Monolayers of Dioleylphosphatidylcholine. *J. Chem. Phys*. **1987**, *86*, 503-507.
9. Brown, R. S.; Brennan, J. D.; Krull, U. J. Self-Quenching of Nitrobenzoxadiazole Labeled Phospholipids in Lipid Membranes. *J. Chem. Phys*. **1994**, *100*, 6019-6027.
10. Ahmad, A.; Kurkina, T.; Kern, K.; Balasubramanian, K. Applications of the Static Quenching of Rhodamine B by Carbon Nanotubes. *ChemPhysChem* **2009**, *10*, 2251-2255.
11. Sohmiya, M.; Omata, S.; Ogawa, M. Two Dimensional Size Controlled Confinement of Poly(vinyl pyrrolidone) in the Interlayer Space of Swelling Clay mineral. *Polym. Chem.* **2012**, *3*, 1069-1074.
12. Ishida, Y.; Shimada, T.; Tachibana, H.; Inoue, H.; Takagi, S. Regulation of the Collisional Self-Quenching of Fluorescence in Clay/Porphyrin Complex by Strong Host-Guest Interaction. *J. Phys. Chem. A* **2012**, *116*, 12065-12072.
13. Bujdák, J.; Iyi, N. Spectral and Structural Characteristics of Oxazine 4/Hexadecyltrimethylammonium Montmorillonite Films. *Chem. Mater.* **2006**, *18*, 2618-2624.
14. Bujdák, J.; Martínez, V. M.; Arbeloa, F. L.; Iyi, N. Spectral Properties of Rhodamine 3B Adsorbed on the Surface of Montmorillonites with Variable Layer Charge. *Langmuir* **2007**, *23*, 1851-1859.

15. Takagi, S.; Shimada, T.; Eguchi, M.; Yui, T.; Yoshida, H.; Tryk, D. A.; Inoue, H. High Density Adsorption of Cationic Porphyrins on Clay Layer Surfaces Without Aggregation: The Size-Matching Effect. *Langmuir* **2002**, *18*, 2265-2272.
16. Takagi, S.; Tryk, D. A.; Inoue, H. Photochemical Energy Transfer of Cationic Porphyrin Complexes on Clay Surface. *J. Phys. Chem. B* **2002**, *106*, 5455-5460.
17. Ishida, Y.; Shimada, T.; Masui, D.; Tachibana, H.; Inoue, H.; Takagi, S. Efficient Excited Energy Transfer Reaction in Clay/Porphyrin Complex Toward an Artificial Light-Harvesting System. *J. Am. Chem. Soc* **2011**, *133*, 14280-14286.
18. Ishida, Y.; Masui, D.; Tachibana, H.; Inoue, H.; Shimada, T.; Takagi, S. Controlling the Micro-Adsorption Structure of Porphyrin Dye Assembly on Clay Surfaces Using the "Size-Matching Rule" for Constructing an Efficient Energy Transfer System. *ACS Appl. Mater. Interfaces* **2012**, *4*, 811-816.
19. Ishida, Y.; Masui, D.; Shimada, T.; Tachibana, H.; Inoue, H.; Takagi, S. The Mechanism of the Porphyrin Spectral Shift on Inorganic Nanosheets: The Molecular Flattening Induced by the Strong Host-Guest Interaction Due to the "Size-Matching Rule" *J. Phys. Chem. C* **2012**, *116*, 7879-7885.
20. Egawa, T.; Watanabe, H.; Fujimura, T.; Ishida, Y.; Yamato, M.; Masui, D.; Shimada, T.; Tachibana, H.; Yoshida, H.; Inoue, H.; Takagi, S. Novel Methodology To Control the Adsorption Structure of Cationic Porphyrins on the Clay Surface Using the "Size-Matching Rule." *Langmuir* **2011**, *27*, 10722-10729.
21. Pavesi, L.; Ceschini, M. Stretched-Exponential Decay of the Luminescence in Porous Silicon. *Phys. Rev. B* **1993**, *48*, 17625-17628.
22. Pasternack, R. F.; Fleming, C.; Herring, S.; Collings, P. J.; dePaula, J.; DeCastro, G.; Gibbs,

E. J. Aggregation Kinetics of Extended Porphyrin and Cyanine Dye Assemblies. *Biophys. J.* **2000**, *79*, 550-560.

23. Phillips, J. C. Stretched Exponential Relaxation in Molecular and Electronic Glasses. *Rep. Prog. Phys*. **1996**, *59*, 1137-1207.
24. Snopok, B. A. Nonexponential Kinetics of Surface Chemical Reactions. *Theor. Exp. Chem*. **2014**, *50*, 67-95.
25. Vijayaraghavan, K.; Padmesh, T. V.; Palanivelu, K.; Velan, M. Biosorption of Nickel(II) Ions onto *Sargassum Wightii*: Application of Two-Parameter and Three-Parameter Isotherm Models. *J. Hazard. Mater*. **2006**, *133*, 304-308.
26. Jensen, R. A.; Coropceanu, I.; Chen, Y.; Bawendi, M. G. Thermal Recovery of Colloidal Quantum Dot Ensembles Following Photoinduced Dimming. *J. Phys. Chem. Lett*. **2015**, *6*, 2933-2937.

Chapter 6. Effects of Surface Charge Density of Clay Minerals on Surface-fixation Induced Emission (S-FIE) of Acridinium Derivatives

6.1. Introduction

Fluorescent materials have attracted great attention as probes, sensors, display materials, and optoelectronics materials.[1–7] Organic dyes have been widely used in these fields because they are composed of ubiquitous elements such as C, N, and O and have less environmental impact compared with inorganic phosphors containing transition elements[8,9] and typical quantum dots contain harmful substances such as Cd and In.[10–12] In devices such as OLED and fluorescent sheets, organic dyes are supposed to be used in a solid phase. On the other hand, the problem is that incorporating dyes with a highly flat π-conjugated system into a solid phase provokes a self-fluorescence quenching due to aggregation by π-π interaction.[13,14] Some aggregates, such as cyanine dyes, often show a high fluorescence quantum yield due to the formation of J-aggregates.[15,16] Recently, many studies have reported AIE (aggregation-induced emission)-active dyes whose fluorescence quantum yield is enhanced by suppressing intramolecular vibration and rotation by forming aggregates have been reported.[17,18] However, accurate molecular design and synthesis techniques are required for these AIE-active dyes.

We have proposed a phenomenon called surface-fixation induced emission (S-FIE), in which the fluorescence of the organic dye is enhanced by forming with nanosheets such as clay minerals.[19–22] Clay minerals, which have two- or three-sheet structures where tetrahedral and octahedral sheets are stacked, are typical layered materials. The negative charges on the surface of clay minerals are produced by isomorphic substitution of Si^{4+} by Al^{3+} in tetrahedral sheet or Al^{3+} by Mg^{2+} in octahedral sheet. The structure of typical clay minerals is shown in Figure 1.5. Clay minerals have been utilized for various purposes because they have the properties such as ion adsorption capacity, swelling property, thermal stability, and these are naturally ubiquitous materials.[23–25] Recently, clay minerals have received much attention as host materials since clay minerals have a flat surface at the atomic level, can be exfoliated into a single layer, and have optical transparency in a solution state.[26–35] Although the fluorescence enhancement of methyl viologen by complexing with clay minerals was reported in 1986,[36,37] there is no systematic study since dyes tend to form aggregates on the clay surface.[38–40] However, we have proposed the phenomenon called Size-Matching Effect in which the specific cationic molecules such as multi-cationic porphyrins are adsorbed on the clay surface without aggregation.[30,41] This report enabled and inspired the research on the intrinsic photochemical behavior of various dyes on the clay minerals without aggregation.

Surface-fixation induced emission is a phenomenon in which the fluorescence is enhanced by the adsorption of dyes on a flat surface such as clay minerals.[19,22,42] In this phenomenon, i) a decrease in nonradiative deactivation rate constant due to suppression of molecular motion such as intramolecular vibration and rotation and/or ii) an increase in radiative deactivation rate constant due to resembling molecular structures between the ground and excited states are

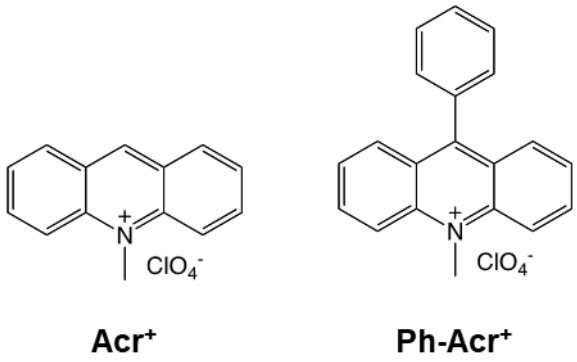

Figure 6.1. Structures of acridinium derivatives.

the cause of fluorescence enhancement. S-FIE has a similar aspect to AIE. S-FIE has the advantage of various cationic dyes being applied with certain expectations. Several researchers have reported fluorescence enhancement due to the adsorption of various dyes on clay minerals.[19–22,35,42] Although previous reports have demonstrated the effect of dye structure for fluorescence enhancement, little has been reported on the effect of the structure of clay minerals. This chapter investigated the photochemical behavior and fluorescence enhancement of mono-cationic acridinium derivatives on the clay surface using two acridinium derivatives as guest molecules (Figure 6.1) and four synthetic saponites, which have different negative charge distances, as host materials.

6.2. Experimental section

6.2.1. Materials

Clay minerals (synthetic saponites): Sumecton SA (Sap1.2) was purchased from Kunimine Industries Co., Ltd. and was used without further purification. According to a previous paper, the synthetic saponites named Sap1.0, Sap1.4, and Sap1.6 were synthesized by hydrothermal synthesis.[41] The synthetic saponites were analyzed with atomic force microscopy (AFM), X-ray diffraction (XRD), X-ray fluorescence (XRF), and Fourier transform infrared spectroscopy

(FT-IR), as described in the previous paper.[41] The general structure and chemical formulas of synthetic saponites are shown in Figure 1.5 and Table 1.4. According to the paper, the cation-exchange capacity (CEC) of Sap1.0, Sap1.2, Sap1.4, and Sap1.6 were 1.32, 0.99, 0.69, and 0.59 mequiv. g^{-1}, respectively. Since the theoretical specific surface area of the synthetic saponite is 750 nm^2 g^{-1}, the inter-negative charge distances of Sap1.0, Sap1.2, Sap1.4, and Sap1.6 were calculated to be 1.04, 1.20, 1.45, and 1.57 nm on the basis of a hexagonal array, respectively. The aqueous dispersion of synthetic saponites, whose particle size is 100 nm or less, is substantially transparent in the UV-visible range. Water was deionized with an ORGANO BB-5A system (PF filter ×2 + G-10 column). 9-Phenyl-9-methylacridinium perchlorate was purchased from Tokyo Kasei. 10-Methylacridinium methyl sulfate was purchased from Aldrich. The counter ion was exchanged to perchlorate with an ion-exchange resin (Organo, Amberlite Resin IRA-400 treated with HClO4).

6.2.2. Analysis

TG-DTA curves were measured with Shimadzu DTG-60H analyzer to determine the water content of acridinium derivatives and synthetic saponites. The temperature was ramped from room temperature to 120°C with a heating rate of 10°C/min under dry air as a purge gas and was held for 60 minutes. Absorption spectra were obtained on a UV-3150 UV-vis. spectrophotometer (SHIMADZU). Fluorescence spectra were obtained on an FP-6500 spectrofluorometer (Jasco), and the excitation light was set at the maximum absorption wavelength of each sample. The reproducibility and signal-to-noise ratio of the fluorescence intensity is 0.5% and 100:1 or higher. The fluorescence quantum yield was determined by the relative method. Rhodamine 6G was used as a standard for calculating the fluorescence

quantum yield of Acr with and without synthetic saponites. The fluorescence quantum yield of Rhodamine 6G in water is 0.90.[43] Fluorescence lifetime was measured by a C4780 picosecond fluorescence lifetime measurement system (Hamamatsu Photonics). An Nd^{3+} YAG laser (EKSPLA PL2210JE + PG-432, fwhm 25 ps, 1 kHz) was used for excitation. The excitation wavelength was 355 nm. The fluorescence lifetimes are calculated by deconvoluting the excitation pulse in each measurement range.

6.2.3. Sample preparation

Stock solutions of acridinium derivatives were prepared in a concentration range of 1.0×10^{-3}–1.0×10^{-4} M. Stock dispersions of synthetic saponites were prepared in a concentration range of 1.0×10^{-3}–1.0×10^{-4} equiv. L^{-1}. In order to prepare acridinium derivative-synthetic saponite complexes, above aqueous stock solutions were mixed at an arbitrary rate and were diluted with water under stirring in a quartz cell (1.0 × 1.0 cm). UV-vis absorption spectra were measured under the concentration of 1×10^{-6} M for acridinium derivatives and 1×10^{-3} equiv. L^{-1} for synthetic saponites. Fluorescence spectra were measured under the concentration of 3.33×10^{-9} M for acridinium derivatives and 2.0×10^{-4}–3.33×10^{-7} equiv. L^{-1} for synthetic saponites. Fluorescence lifetimes were measured under the concentration of 4.0×10^{-8} M for acridinium derivatives and 4.0×10^{-4} equiv. L^{-1} for synthetic saponites.

6.3. Result and discussion

6.3.1. Adsorption behavior of acridinium derivatives in water and on the clay surface

The adsorption behavior of acridinium derivatives on various synthetic saponites was evaluated by measuring UV-vis absorption spectra. The UV-vis absorption spectra of Acr^{+}

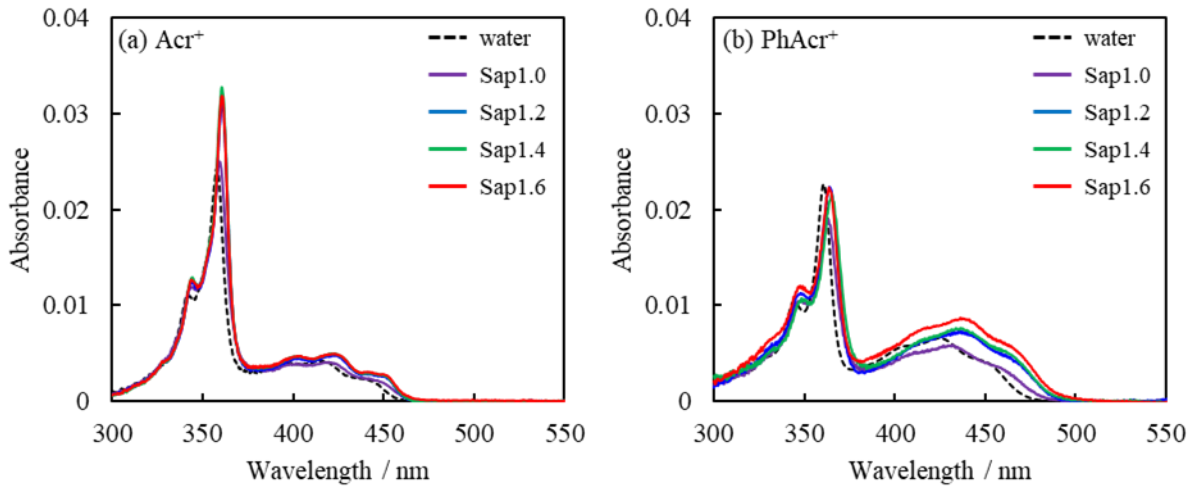

Figure 6.2. UV-vis absorption spectra of acridinium derivatives ((a) Acr^+, (b) $PhAcr^+$ with and without synthetic saponites in aqueous solution. [acridinium derivatives] = 1.0×10^{-6} M, [synthetic saponites] = 1.0×10^{-3} equiv. L^{-1}.

Table 6.1. Band Maxima of Absorption(λ_{ab}) and Fluorescence(λ_{fl}) and Stokes Shift ($\Delta\lambda$) of Acridinium Derivatives with and without Synthetic Saponites in Water

compound	environment	λ_{ab}		λ_{fl}		$\Delta\lambda$	
		nm	cm^{-1}	nm	cm^{-1}	nm	cm^{-1}
Acr^+	water	444	22523	462	21645	18	878
Acr^+	Sap1.0	447	22371	465	21505	18	866
Acr^+	Sap1.2	448	22321	465	21505	17	816
Acr^+	Sap1.4	448	22321	465	21505	17	816
Acr^+	Sap1.6	448	22321	465	21505	17	816
$PhAcr^+$	water	454	22026	485	20619	31	1408
$PhAcr^+$	Sap1.0	460	21739	490	20408	30	1331
$PhAcr^+$	Sap1.2	465	21505	490	20408	25	1097
$PhAcr^+$	Sap1.4	465	21505	490	20408	25	1097
$PhAcr^+$	Sap1.6	468	21368	490	20408	22	959

and $PhAcr^+$ with and without synthetic saponite in water are shown in Figure 6.2. The maximum absorption wavelengths (λ_{ab}) are summarized in Table 6.1.

Both Acr^+ and $PhAcr^+$ showed a redshift by the adsorption on the surface of synthetic saponites. The wavelength shifts of Acr^+ and $PhAcr^+$ on Sap1.2 were 4 nm and 11 nm, respectively. Such spectral shifts due to adsorption on the clay surface have been reported in

many papers.[28–30,36,46,47] These reports proposed that the cause of redshift is the expansion of the π-conjugated system due to flattening of molecules on clay minerals, where the surface is flat at the atomic level.[44–47] $PhAcr^+$, which has a rotational substituent, showed a larger wavelength shift than Acr^+, which does not have a rotational substituent, suggesting that a similar phenomenon occurred in the case of acridinium derivatives. Furthermore, as the inter-negative charge distance of the synthetic saponite increased, the redshift of the maximum absorption wavelength of $PhAcr^+$ increased. It is considered that the further redshift is induced by the increase in adsorption strength due to increase in the inter-negative charge distance on the clay surface.

Acridinium derivatives have two main absorption bands in their absorption spectra, as shown in Figure 6.2. It is known that a very narrow absorption band at about 360 nm and a broad absorption band at about 450 nm are attributed to the S_0-S_2 transition and the S_0-S_1 transition, respectively.[48,49] In order to discuss the S_0-S_1 transition, the integral values of the extinction coefficient at 380–550 nm are summarized in Table 6.2. The integral values of the

Table 6.2. Integral Values of Extinction Coefficients of Acridinium Derivatives with and without Synthetic Saponites in Water[a]

compound	clay minerals	integral of the extinction coefficient / 10^7 M^{-1} cm^{-1}		
		$\int \varepsilon^W$	$\int \varepsilon^C$	$\int \varepsilon^C \int \varepsilon^W$
Acr^+	Sap1.0	1.46	1.44	0.99
Acr^+	Sap1.2	1.46	1.74	1.19
Acr^+	Sap1.4	1.46	1.72	1.18
Acr^+	Sap1.6	1.46	1.80	1.24
$PhAcr^+$	Sap1.0	2.39	2.25	0.94
$PhAcr^+$	Sap1.2	2.39	2.82	1.18
$PhAcr^+$	Sap1.4	2.39	2.99	1.25
$PhAcr^+$	Sap1.6	2.39	3.26	1.37

[a] The integral range is 18182–26315 cm^{-1} (380–550 nm). $\int \varepsilon^W$ and $\int \varepsilon^C$ are the integral values of the extinction coefficients of acridinium derivatives in water and with synthetic saponites, respectively.

extinction coefficient of acridinium derivatives on the surface of synthetic saponites were larger than those in water, indicating an increase in the transition probability, namely the Franck-Condon factor when acridinium derivatives adsorbed on the surface of synthetic saponites. It suggests that the difference of nuclear coordinates of ground and excited states becomes smaller by the adsorption of acridinium derivatives on the surface of synthetic saponites. As the inter-negative charge distance of synthetic saponites increased, the integral value of the extinction coefficient of $PhAcr^+$ increased. Since the surface of synthetic saponites with a larger inter-negative charge distance becomes more hydrophobic, it is presumed that acridinium derivatives on such a more hydrophobic surface were more firmly fixed. Likewise, photochemical properties of $PhAcr^+$ such as λ_{ab} and λ_{fl} were influenced by the adsorption on the surface of synthetic saponites, and the effect of the clay surface became larger as the inter-negative charge distance on the surface of synthetic saponites increased. These results indicate that the hydrophobic interaction between $PhAcr^+$ and the surface of synthetic saponites plays an important role in the photochemical properties of $PhAcr^+$.

6.3.2. Fluorescence behavior of acridinium derivatives in water and on the clay surface

The fluorescence behavior of acridinium derivatives on synthetic saponites was evaluated by fluorescence spectra. Most of the dyes suffer self-fluorescence quenching when adsorbed on the clay surface.[50–53] Whereas acridinium derivatives also were self-quenched when adsorbed on the clay surface, they were not self-quenched when the loading level was less than 0.01% vs. CEC in any combination of acridinium derivatives and clays, as shown in Chapter 5. The fluorescence spectra of acridinium derivatives in water and on synthetic saponites (0.01% vs. CEC) are shown in Figure 6.3. The maximum fluorescence wavelength (λ_{fl}) and

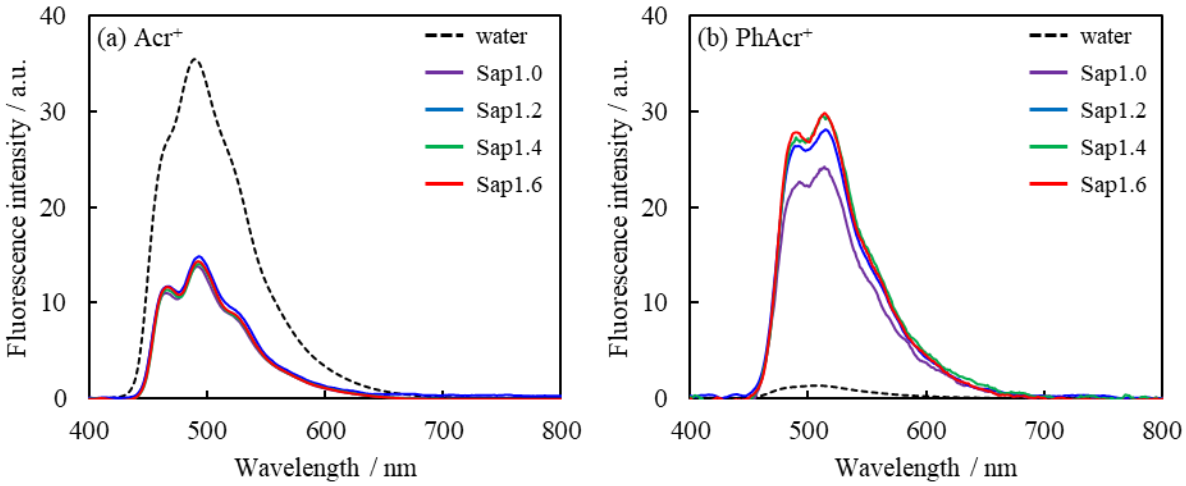

Figure 6.3. Fluorescence spectra of acridinium derivatives ((a) Acr^+, (b) $PhAcr^+$) with and without synthetic saponites in water. [acridinium derivatives] = 3.33×10^{-9} M, [synthetic saponites] = 3.33×10^{-5} equiv. L^{-1}. The excitation wavelength was 360 nm. The spectra were corrected with absorbance at 360 nm.

Stokes shift ($\Delta\lambda$) are summarized in Table 6.1.

In most cases, organic molecules in solution do not show a clear vibrational structure in the fluorescence spectra due to the effect of molecular motion and surrounding solvent reorientation. The fluorescence spectra of Acr^+ and $PhAcr^+$ in water did not show clear vibrational structures, as shown in Figure 6.3 (broken line). On the other hand, The fluorescence spectra of Acr^+ and $PhAcr^+$ on synthetic saponites showed more apparent vibrational structures. For all cases, Stokes shift of acridinium derivatives on synthetic saponites became smaller than that in water, as shown in Table 6.1. The Stokes shift means the degree of solvent reorientation around dye molecules at the electronic transition.[54] It is known that hydrophobic interaction plays an important role in the adsorption of organic dyes on the clay surface.[55,56] When the organic dyes are adsorbed on the clay surface, the number of surrounding water molecules decreased almost half compared to that in water since half of the surface of organic dye is covered by the clay surface. It suggests that the dye molecules

on the clay surface have less solvent reorientation and less molecular structure change in the electronic transition. Therefore, the reasons for the clear vibrational structure and the slight Stokes shift when acridinium derivatives adsorbed on synthetic saponites are the fixation of molecular structure and the less solvent reorientation in the electronic transition. In addition, as the inter-negative charge distance on the surface of synthetic saponite increased, Stokes shift tended to decrease. The hydrophobicity of the clay surface is enhanced by the increase in the inter-negative charge distance.[57,58] Acridinium derivatives should be adsorbed more parallelly on the more hydrophobic clay surface due to the effective hydrophobic interaction between acridinium derivatives and the clay surface. It is presumed that a strong fixation of acridinium derivatives on the clay surface causes a decrease in molecular structure relaxation in the excited state. Therefore, the decrease in Stokes shift with the increase in inter-negative charge distance is attributed to a decrease in the structure change and the solvent reorientation in the excited state.

Table 6.3 shows fluorescence quantum yields (Φ_f) of Acr^+ and $PhAcr^+$ in water and on

Table 6.3. Fluorescence Quantum Yield (Φ_f) and Fluorescence Lifetime (τ) of Acridinium Derivatives with and without Clays in Water[a]

compound	clay minerals	quantum yield			fluorescence lifetime / ns		
		Φ_f^W	Φ_f^C	Φ_f^C/Φ_f^W	τ^W	τ^C	τ^C/τ^W
Acr^+	sap1.0	0.173	0.068	0.39	30.2	28.7	0.95
Acr^+	sap1.2	0.173	0.072	0.42	30.2	29.4	0.97
Acr^+	sap1.4	0.173	0.069	0.40	30.2	29.7	0.98
Acr^+	sap1.6	0.173	0.070	0.41	30.2	30.0	0.99
$PhAcr^+$	sap1.0	0.0065	0.118	18.1	1.55	14.5	9.4
$PhAcr^+$	sap1.2	0.0065	0.137	21.1	1.55	15.8	10.2
$PhAcr^+$	sap1.4	0.0065	0.144	22.2	1.55	15.1	9.7
$PhAcr^+$	sap1.6	0.0065	0.148	22.3	1.55	16.1	10.4

[a] Φ_f^W and Φ_f^C are the Φ_f of Acr in water and on the clay surface. τ^w and τ^C are the τ of acridinium derivatives in water and on the surface of synthetic saponites.

Table 6.4. Radiative (k_f) and Non-radiative (k_{nr}) Deactivation Rate Constants of Acrdinium Derivatives with and without Various Synthetic Saponites in Water[a]

compound	clay minerals	radiative deactivation rate constant / 10^7 s^{-1}			non-radiative deactivation rate constant / 10^7 s^{-1}		
		k_f^W	k_f^C	k_f^C/k_f^W	k_{nr}^W	k_{nr}^C	k_{nr}^C/k_{nr}^W
Acr^+	sap1.0	0.57	0.24	0.41	2.74	3.26	1.19
Acr^+	sap1.2	0.57	0.25	0.43	2.74	3.16	1.15
Acr^+	sap1.4	0.57	0.23	0.41	2.74	3.14	1.15
Acr^+	sap1.6	0.57	0.23	0.41	2.74	3.11	1.14
$PhAcr^+$	sap1.0	0.42	0.81	1.94	64.0	6.08	0.095
$PhAcr^+$	sap1.2	0.42	0.87	2.07	64.0	5.46	0.085
$PhAcr^+$	sap1.4	0.42	0.96	2.28	64.0	5.67	0.089
$PhAcr^+$	sap1.6	0.42	0.92	2.19	64.0	5.29	0.083

[a] k_f^W and k_f^C are the k_f of acridinium derivatives in water and on the clay surface. k_{nr}^W and k_{nr}^C are the k_{nr} of acridinium derivatives in water and on the surface of synthetic saponites.

various synthetic saponites. Although Φ_f of Acr^+ on the surface of synthetic saponites became smaller than in water, Φ_f of $PhAcr^+$ was enhanced approximately 20 times by the adsorption on the surface of synthetic saponites. As the inter-negative charge distance on the surface of synthetic saponites increased, Φ_f of $PhAcr^+$ was enhanced. It is well known that Φ_f of dyes adsorbed on the clay surface without aggregation is often greater than in solution. The effect of the clay surface on the fluorescence enhancement has been proposed as Surface-fixation induced emission (S-FIE).[29,42] Several studies have reported that the major factor of fluorescence enhancement is the fixation of rotational substituents.[21,22] Thus, suppressing the rotational substituent due to strong fixation of acridinium derivatives on the hydrophobic surface of synthetic saponite could be why the synthetic saponite with large inter-negative charge distance induced the large fluorescence enhancement, as in the case with the discussion of Stokes shift.

The time-resolved fluorescence measurement was carried out to discuss further the

photochemical behavior of acridinium derivatives on the surface of synthetic saponites. Fluorescence lifetimes of Acr^+ and $PhAcr^+$ in water and on various clays are shown in Table 6.3. Fluorescence decays are shown in Figure S6.1. The radiative deactivation rate constants (k_f) and the non-radiative deactivation constants (k_{nr}) are calculated from the fluorescence lifetime (τ) and fluorescence quantum yield (Φ_f) according to Eq. (6.1) and Eq. (6.2), and are shown in Table 6.4.

$$k_f = \frac{\Phi_f}{\tau} \tag{6.1}$$

$$k_{nr} = \frac{1 - \Phi_f}{\tau} \tag{6.2}$$

When Acr^+ without rotational substituents was adsorbed on the clay surface, the k_f decreased. On the other hand, when $PhAcr^+$ with a rotational substituent was adsorbed on the clay surface, k_f doubled, and k_{nr} decreased by about one in ten. It is known that k_f and k_{nr} of the dyes showing S-FIE tend to increase and decrease by the adsorption on the clay surface, respectively.[22] Previous reports also indicated that the change in potential energy curve of the ground and excited states of dyes adsorbed on the clay surface causes such changes in k_f and k_{nr}.[22] According to the reports, it has been presumed that (i) the most stable structures of the ground and excited states are relatively similar (effect I) and (ii) the potential energy curve is relatively sensitive against the nuclear coordinates (effect II) for dyes on the clay surface compared to without clay, as can be seen in Figure 6.4 (a) and (b). It was concluded that effects I and II were related to an increase in $\underline{k}_f$ and a decrease in k_{nr}, respectively. Since $PhAcr^+$ has a rotational substituent at 9-position and Acr^+ has no rotational substituents, $PhAcr^+$ is more sensitive against a surrounding environmental change than Acr^+. Consequently, when

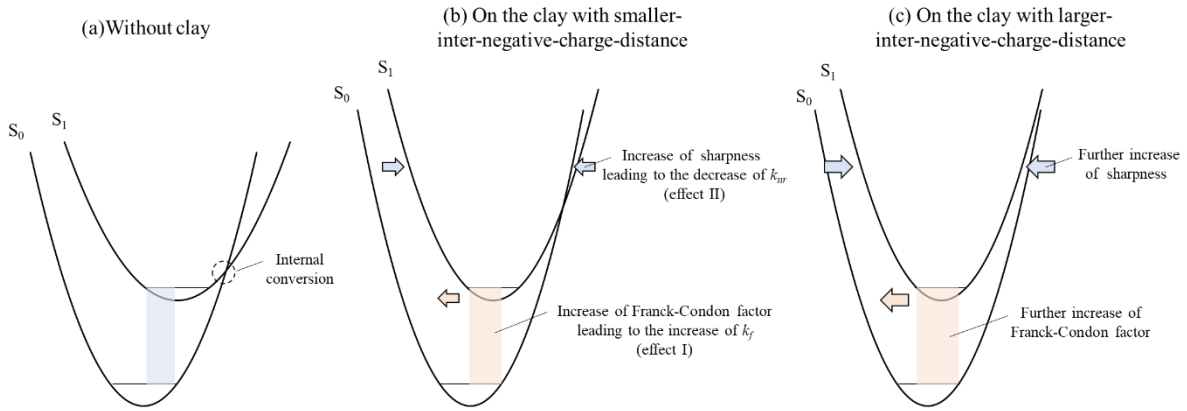

Figure 6.4. Plausible conceptual potential energy curves of ground and excited states for $PhAcr^+$. (a) Without clay (b) On the clay with smaller inter-negative charge distance (c) On the clay with larger inter-negative charge distance.

$PhAcr^+$ adsorbed on the surface of synthetic saponites, the intramolecular rotation of $PhAcr^+$ was suppressed by the clay surface, leading to the increase in k_f (effect I). The increase in the integral values of the extinction coefficient by the adsorption on the surface of synthetic saponites (Table 6.2) can be rationalized in the same way.

The decrease in k_{nr} when acridinium derivatives are adsorbed on the surface of synthetic saponites is attributed to a suppression of the mobility of rotational substituent (effect II). The increase in inter-negative charge distance on the surface of synthetic saponites is related to an increase in k_f and a decrease in k_{nr} due to the adsorption on the clay surface, respectively. These results indicate that the effects I and II were enhanced by the increase in the inter-negative charge distance on the surface of synthetic saponites, as shown in Figure 6.4 (c). As mentioned above, the increase in inter-negative charge distance on the surface of synthetic saponites caused the increase in the extinction coefficient and the redshift of maximum absorption wavelength for $PhAcr^+$ on the surface of synthetic saponites (Table 6.2). Those results consistently suggest that the interaction between $PhAcr^+$ and the surface of synthetic

saponites becomes stronger as the inter-negative charge distance on the clay surface increases. Since clays with large inter-negative charge distances have a highly hydrophobic surface, the hydrophobic interaction causes $PhAcr^+$ to be more firmly immobilized on the clay surface. In conclusion, the present study has demonstrated that the photochemical behavior of acridinium derivatives on the surface of clay minerals was affected by not only the structure of guest molecules but also the structure of clay minerals.

6.4. Conclusion

This chapter evaluated the photochemical behaviors of cationic acridinium derivatives with and without various synthetic saponites. The maximum absorption wavelength showed a redshift when acridinium derivatives were adsorbed on the surface of synthetic saponites. Because the absorption spectra of $PhAcr^+$ on the surface of synthetic saponites showed a longer redshift than that of Acr^+, it was suggested that the expansion of the π-conjugated system of $PhAcr^+$. In addition, an increase in the extinction coefficient and the fluorescence quantum yield were observed for $PhAcr^+$ adsorbed on the surface of synthetic saponites. Furthermore, an increase in k_f and a decrease in k_{nr} were observed. These changes in photochemical properties indicate the suppression of rotational substituent's mobility by flattening the dihedral angle between the rotational substituent and the acridinium ring due to adsorption of $PhAcr^+$ on the surface of synthetic saponites. A decrease in Stokes shift due to adsorption of $PhAcr^+$ on the surface of synthetic saponites indicates that the molecular structural change and the solvent reorientation at excited state decreased. The present results suggest that not only the structure of guest molecules but also the structure of clay minerals as host materials affected the photochemical properties of guest molecules adsorbed on the clay surface.

6.5. Supporting information

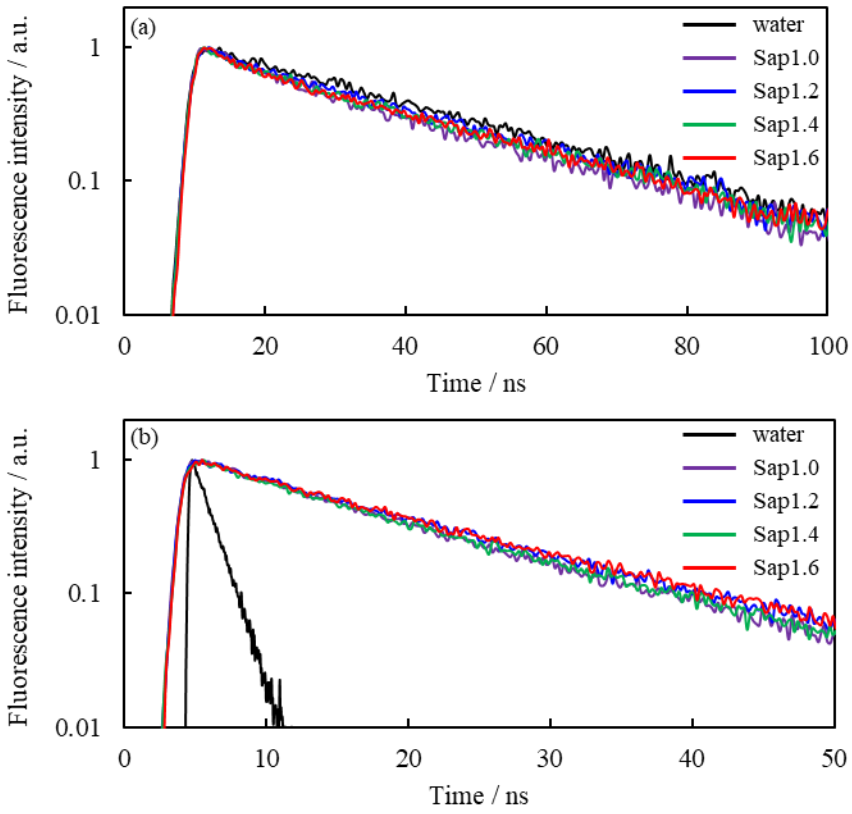

Figure S6.1. Fluorescence decay profiles for (a) Acr^+ and (b) $PhAcr^+$ with and without various synthetic saponites in water. [acridinium derivatives] = 3.33×10^{-9} M, [synthetic saponites] = 3.33×10^{-4} equiv. L^{-1}. The dye loading levels were 0.010% vs. CEC of the clay. The excitation wavelength was 355 nm.

6.6. References

1. Thomas, S. W.; Joly, G. D.; Swager, T. M. Chemical Sensors Based on Amplifying Fluorescent Conjugated Polymers. *Chem. Rev*. **2007**, *107*, 1339–1386.

2. Basabe-Desmonts, L.; Reinhoudt, D. N.; Crego-Calama, M. Design of Fluorescent Materials for Chemical Sensing. *Chem. Soc. Rev.* **2007**, *36*, 993–1017.

3. Minaev, B.; Baryshnikov, G.; Agren, H. Principles of Phosphorescent Organic Light Emitting Devices. *Phys. Chem. Chem. Phys.* **2014**, *16*, 1719–1758.

4. Uoyama, H.; Goushi, K.; Shizu, K.; Nomura, H.; Adachi, C. Highly Efficient Organic Light-emitting Diodes from Delayed Fluorescence. *Nature* **2012**, *492*, 234–238.

5. Lin, C. C.; Liu, R. Advances in Phosphors for Light-emitting Diodes. *J. Phys. Chem. Lett.* **2011**, *2*, 1268–1277.

6. Ito, Y.; Hori, T.; Kusunoki, T.; Nomura, H.; Kondo, H. A Phosphor Sheet and a Backlight System Providing Wider Color Gamut for LCDs. *J. Soc. Inf. Disp.* **2014**, *22*, 419–428.

7. Samuel, I. D.; Tunbulll, G. A. Organic Semiconductor Lasers. *Chem. Rev*. **2007**, *107*, 1272–1295.

8. Paulusz, A. G. Efficient Mn(IV) Emission in Fluorine Coordination. *J. Electrochem. Soc.* **1973**, *120*, 942–947.

9. Zhou, Z.; Zhou, N.; Xia, M.; Yokoyama, M.; Hintzen, H. T. Research Progress and Application Prospects of Transition Metal Mn^{4+}-activated Luminescent Materials. *J. Mater. Chem. C* **2016**, *4*, 9143–9161.

10. Murray, C. B.; Norris, D. J.; Bawendi, M. G. Synthesis and Characterization of Nearly Monodisperse CdE (E = Sulfur, Selenium, Tellurium) Semiconductor Nanocrystallites. *J. Am. Chem. Soc.* **1993**, *115*, 8706–8715.

11. Dabbousi, B. O.; Rodriguez-Viejo, J.; Mikulec, F. V.; Heine, J. R.; Mattoussi, H.; Ober, R.; Jensen, K. F.; Bawendi, M. G. (CdSe)ZnS Core−Shell Quantum Dots: Synthesis and Characterization of a Size Series of Highly Luminescent Nanocrystallites. *J. Phys. Chem. B* **1997**, *101*, 9463–9475.

12. Lim, J.; Park, M.; Bae, W. K.; Lee, D.; Lee, S.; Lee, C.; Char, K. Highly Efficient Cadmium-Free Quantum Dot Light-Emitting Diodes Enabled by the Direct Formation

of Excitons within InP@ZnSeS Quantum Dots. *ACS Nano* **2013**, *7*, 9019–9026.

13. Matsui, M.; Ikeda, R.; Kubota, Y.; Funabiki, K. Red Solid-state Fluorescent Aminoperfluorophenazines. *Tetrahedron Lett.* **2009**, *50*, 5047–5049.

14. Green, A. P.; Buckley, A. R. Solid State Concentration Quenching of Organic Fluorophores in PMMA. *Phys. Chem. Chem. Phys.* **2015**, *17*, 1435–1440.

15. Valandro, S. R.; Poli, A. L.; Correia, T. F.; Lombardo, P. C.; Schmitt, C. C. Photophysical Behavior of Isocyanine/Clay Hybrids in the Solid State. *Langmuir* **2017**, *33*, 891–899.

16. Boháč, P.; Czímerová, A.; Bujdák, J. Enhanced Luminescence of 3,3'-Diethyl-2,2'-thiacyanine Cations Adsorbed on Saponite Particles. *Appl. Clay Sci.* **2016**, *127-128*, 64-69.

17. Luo, J.; Xie, Z.; Lam, J. W.; Cheng, L.; Chen, H.; Qiu, C.; Kwok, H. S.; Zhan, X.; Liu, Y.; Zhu, D.; Tang, B. Z. Aggregation-induced Emission of 1-Methyl-1,2,3,4,5-pentaphenylsilole. *Chem. Commun.* **2001**, 1740–1741.

18. Mei, J.; Leung, N. L.; Kwok, R. T.; Lam, W. Y.; Tang, B. Z. Aggregation-Induced Emission: Together We Shine, United We Soar! *Chem. Rev.* **2015**, *115*, 11718–11940.

19. Tsukamoto, T.; Shimada, T.; Takagi, S. Unique Photochemical Properties of *p*-Substituted Cationic Triphenylbenzene Derivatives on a Clay Layer Surface. *J. Phys. Chem. C* **2013**, *117*, 2774–2889.

20. Ishida, Y.; Shimada, T.; Takagi, S. "Surface-Fixation Induced Emission" of Porphyrazine Dye by a Complexation with Inorganic Nanosheets. *J. Phys. Chem. C* **2014**, *118*, 20466–20471.

21. Tsukamoto, T.; Shimada, T.; Takagi, S. Structure Resembling Effect of Clay Surface on

Photochemical Properties of *meso*-phenyl or Pyridyl-Substituted Monocationic Antimony(V) Porphyrin Derivatives. *RSC Adv.* **2015**, *5*, 8479–8485.

22. Tokieda, D.; Tsukamoto, T.; Ishida, Y.; Ichihara, H.; Shimada, T.; Takagi, S. Unique Fluorescence Behavior of Dyes on the Clay Minerals Surface: Surface Fixation Induced Emission (S-FIE). *J. Photochem. Photobio. A: Chem.* **2017**, *339*, 67–79.

23. Tahir, S. S.; Rauf, N. Removal of a Cationic Dye from Aqueous Solutions by Adsorption onto Bentonite Clay. *Chemosphere* **2006**, *63*, 1842–1848.

24. Moet, A. S.; Akelah, A. Polymer-clay Nanocomposites: Polystyrene Grafted onto Montmorillonite Interlayers. *Mater. Lett.* **1993**, *18*, 97–102.

25. Weimer, M. W.; Chen, H.; Giannelis, E. P.; Sogah, D. Y. Direct Synthesis of Dispersed Nanocomposites by in Situ Living Free Radical Polymerization Using a Silicate-Anchored Initiator. *J. Am. Chem. Soc.* **1999**, *121*, 1615–1616.

26. Takagi, S.; Eguchi, M.; Inoue, H. Photochemical Electron Transfer Reactions in Clay-Porphyrin Complexes. *Clay Sci.* **2006**, *12*, 82–87.

27. Ishida, Y.; Shimada, T.; Masui, D.; Tachibana, H.; Inoue, H.; Takagi, S. Efficient Excited Energy Transfer Reaction in Clay/Porphyrin Complex toward an Artificial Light-Harvesting System. *J. Am. Chem. Soc*. **2011**, *133*, 14280–14286.

28. Eguchi, M.; Shimada, T.; Tryk, D. A.; Inoue, H.; Takagi, S. Role of Hydrophobic Interaction in Controlling the Orientation of Dicationic Porphyrins on Solid Surfaces. *J. Phys. Chem. C.* **2013**, *117*, 9245–9251.

29. Tsukamoto, T.; Shimada, T.; Takagi, S. Photophysical Properties and Adsorption Behaviors of Novel Tri-Cationic Boron(III) Subporphyrin on Anionic Clay Surface. *ACS Appl. Mater. Interfaces* **2016**, *8*, 7522–7528.

30. Takagi, S.; Shimada, T.; Eguchi, M.; Yui, T.; Yoshida, H.; Tryk, D. A.; Inoue, H. High-Density Adsorption of Cationic Porphyrins on Clay Layer Surfaces without Aggregation: The Size-Matching Effect. *Langmuir* **2002**, *18*, 2265–2272.

31. Schoonheydt, R. A.; De Pauw, P.; Vliers, D.; De Schrijver, F. C. Luminescence of Tris(2,2'-Bipyridine)ruthenium(II) in Aqueous Clay Minerals Suspensions. *J. Phys. Chem.* **1984**, *88*, 5113-5118.

32. Suzuki, Y.; Tenma, Y.; Nishioka, Y.; Kawamata, J. Efficient Nonlinear Optical Properties of Dyes Confined in Interlayer Nanospaces of Clay Minerals. *Chem. Asian J.* **2012**, *7*, 1170–1179.

33. Ogawa, M.; Kuroda, K. Photofunctions of Intercalation Compounds. *Chem. Rev*. **1995**, *95*, 399-438.

34. Grabolle, M.; Starke, M.; Resch-Genger, U. Highly Fluorescent Dye-Nanoclay Hybrid Materials Made from Different Dye Classes, *Langmuir* **2016**, *32*, 3506–3513.

35. Wu, L.; Lv, G.; Liu, M.; Li, Z.; Liao, L.; Pan, C. Adjusting the Layer Charges of Host Phyllosilicates To Prevent Luminescence Quenching of Fluorescence Dyes. *J. Phys. Chem. C* **2015**, *119*, 22625–22631.

36. Villemure, G.; Detellier, C.; Szabo, A. G. Fluorescence of Clay-intercalated Methylviologen. *J. Am. Chem. Soc.* **1986**, *108*, 4658–4659.

37. Villemure, G.; Detellier, C.; Szabo, A. G. Fluorescence of Methylviologen Intercalated into Montmorillonite and Hectorite Aqueous Suspensions. *Langmuir* **1991**, *7*, 1215–1221.

38. Bujdák, J.; Iyi, N. Molecular Aggregation of Rhodamine Dyes in Dispersions of Layered Silicates: Influence of Dye Molecular Structure and Silicate Properties. *J. Phys.*

Chem. B **2006**, *110*, 2180-2186.

39. López-Arbeloa, F.; Martínez-Martínez, V.; Bañuelos Prieto, J.; López-Arbeloa, I. Adsorption of Rhodamine 3B Dye on Sapointe Colloidal Particles in Aqueous Suspensions. *Langmuir* **2002**, *18*, 2658-2664.

40. Iyi, N.; Sasai, R.; Fujita, T.; Deguchi, T.; Sota, T.; López-Arbeloa, F.; Kitamura, K. Orientation and Aggregation of Cationic Laser Dyes in a Fluoromica: Polarized Spectrometry Studies. *Appl. Clay Sci.* **2002**, *20*, 125-136.

41. Egawa, T.; Watanabe, H.; Fujimura, T.; Ishida, Y.; Yamato, M.; Masui, D.; Shimada, T.; Tachibana, H.; Yoshida, H.; Inoue, H.; Takagi, S. Novel Methodology to Control the Adsorption Structure of Cationic Porphyrins on the Clay Surface Using the "Size-Matching Rule." *Langmuir* **2011**, *27*, 10722–10729.

42. Kudo, N.; Tsukamoto, T.; Shimada, T.; Takagi, S. Fluorescence Enhancement Behavior of Hemicyanine Derivatives on the Clay Nanosheets: Aggregation Induced Emission (AIE) vs. Surface-fixation Induced Emission (S-FIE). *Chem. Lett.* **2018**, *47*, 636–639.

43. Magde, D.; Wong, R.; Seybold, P. G. Fluorescence Quantum Yields and Their Relation to Lifetimes of Rhodamine 6G and Fluorescein in Nine Solvents: Improved Absolute Standards for Quantum Yields. *Photochem. Photobiol.* **2002**, *75*, 327–334.

44. Eguchi, M.; Takagi, S.; Tachibana, H.; Inoue, H. The 'Size Matching Rule' in Di-, Tri-, and Tetra-cationic Charged Porphyrin/synthetic Clay Complexes: Effect of the Inter-charge Distance and the Number of Charged Sites. *J. Phys. Chem. Solids* **2004**, *65*, 403–407.

45. Kuykendall, V. G.; Thomas, J. K. Photophysical Investigation of the Degree of Dispersion of Aqueous Colloidal Clay. *Langmuir* **1990**, *6*, 1350–1356.

46. Chernia, Z.; Gill, D. Flattening of TMPyP Adsorbed on Laponite. Evidence in Observed and Calculated UV-vis Spectra. *Langmuir* **1999**, *15*, 1625–1633.

47. Nakazato, R.; Sano, K.; Ichihara, H.; Ishida, T.; Shimada, T.; Takagi, S. Factors for the Emission Enhancement of Dimidium in Specific Media such as in DNA and on a Clay Surface. *Phys. Chem. Chem. Phys.* **2019**, *21*, 22732–22739.

48. Hu, J.; Xia, B.; Bao, D.; Ferreira, A.; Wan, J.; Jones, G. II; Vullev, V. I. Long-Lived Photogenerated States of α-Oligothiophene-Acridinium Dyads Have Triplet Character. *J. Phys. Chem. A* **2009**, *113*, 3096-3107.

49. Eberhard, J.; Peuntinger, K.; Fröhlich, R.; Guldi, D. M.; Mattay, J. Synthesis and Properties of Acridine and Acridinium Dye Functionalized Bis(terpyridine) Ruthenium(II) Complexes. *Eur. J. Org. Chem.* **2018**, *2018*, 2682-2700.

50. Ishida, Y.; Shimada, T.; Tachibana, H.; Inoue, H.; Takagi, S. Regulation of the Collisional Self-Quenching of Fluorescence in Clay/Porphyrin Complex by Strong Host-Guest Interaction. *J. Phys. Chem. A* **2012**, *116*, 12065–12072.

51. Wakayama, S.; Takagi, S.; Shimada, T. Adsorption and Photochemical Behavior of Mono-cationic Porphyrin onto Synthetic Saponite. *Clay Sci.* **2016**, *20*, 39–41.

52. Sohmiya, M.; Omata, S.; Ogawa, M. Two Dimensional Size Controlled Confinement of Poly(vinyl pyrrolidone) in the Interlayer Space of Swelling Clay Mineral. *Polym. Chem.* **2012**, *3*, 1069–1074.

53. López-Arbeloa, F.; Martínez-Martínez, V.; Arbeloa, T.; López-Arbeloa, I. Photoresponse and Anisotropy of Rhodamine Dye Intercalated in Ordered Clay Layerd Films. *J. Photochem. Photobiol. C* **2007**, *8*, 85-108.

54. Mataga, N.; Kaifu, Y.; Koizumi, M. The Solvent Effect on Fluorescence Spectrum.

Change of Solute-Solvent Interaction during the Lifetime of Excited Solute Molecule. *Bull. Chem. Soc. Jpn.* **1955**, *28*, 690–691.

55. Takigawa, T.; Yoshida, Y.; Fujimura, T.; Ishida, T.; Shimada, T.; Takagi, S. Adsorption Behavior of Mono-Cationic Pyridinium Salts on the Clay Surface. *Bull. Chem. Soc. Jpn.* **2020**, *93*, 1046–1049.

56. Yoshida, Y.; Shimada, T.; Ishida, T.; Takagi, S. Thermodynamic Study of the Adsorption of Acridinium Derivatives on the Clay Surface. *RSC Adv.* **2020**, *10*, 21360–21368.

57. Saada, A.; Siffert, B.; Papírer, E. Comparison of the Hydrophilicity/Hydrophobicity of Illites and Kaolinites. *J. Colloid Interface Sci.* **1995**, *174*, 185–190.

58. Yin, X.; Gupta, V.; Du, H.; Wang, X.; Miller, J. D. Surface Charge and Wetting Characteristics of Layered silicate minerals. *Adv. Colloid Interface Sci*. **2012**, *179–182*, 43–50.

Chapter 7. Photophysical Behavior of TICT-active Acridinium Derivative adsorbed on Clay Surface

7.1. Introduction

TICT, reported by Grabowski, Rotkiewicz, and Rettig, *et al.,* is a phenomenon found in molecules where the donor and acceptor are bound by a single bond.[1] Molecule that exhibits the equilibrium between the orthogonal and planarized states emit dual fluorescence due to relaxation from the locally excited (LE) state and the charge transfer (CT) state. Because this relaxation pathway can be easily modulated by substituents, polarity, steric hindrance, and the surrounding environment, the TICT process has become one of the design strategies for functional molecules. Therefore, TICT-active molecules have been received great attention for OLEDs, chemical sensors, optoelectronic devices, and catalysis.

In a polar environment, the TICT active molecules form the LE state, which quickly becomes the CT state due to the reorientation of the polar solvent. On the other hand, in a non-polar environment, the LE state is more stable than the CT state because the solvent molecules do not rearrange. The LE and CT states of TICT-active molecules, which depend on the solvent environment, are described by potential curves. For example, several papers have discussed the molecular structure by describing the activation energy and relative relationship between the LE state and CT state in terms of potential curves.[2–6] However, there are no reports focusing on the width of the potential curve or the relative positions of the ground and excited states in TICT-active molecules, as shown in Chapter 6. 9-Mesityl-10-methylacridinium ($MesAcr^+$) is also a TICT-active molecule (Figure 7.1).[7] The long-lived

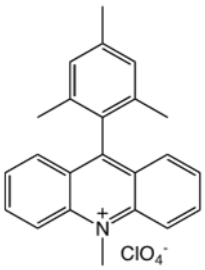

MesAcr$^+$

Figure 7.1. Structure of 9-mesityl-10-methylacridinium (MesAcr$^+$)

charge-separated state reported by Fukuzumi *et al.*[8–11] has led many researchers to focus on the catalytic activity and the charge-separated state of MesAcr$^+$.[12–15] It has also been suggested that MesAcr$^+$ shows the dual fluorescence from LE and CT states,[7] although few reports have discussed this phenomenon in detail.

This chapter aims to explain the influence of the clay surface on the potential curve, including LE and CT states. We evaluated the behavior of MesAcr$^+$ adsorbed on the clay surface to clarify the influence of the surrounding environment on TICT-active molecules by the absorption and steady-state fluorescence spectra and time-resolved fluorescence.

7.2. Experimental section

Clay minerals (synthetic saponites): Sumecton SA (Sap1.2) was purchased from Kunimine Industries Co., Ltd. and was used without further purification. The synthetic saponites were analyzed with atomic force microscopy (AFM), X-ray diffraction (XRD), X-ray fluorescence (XRF), and Fourier transform infrared spectroscopy (FT-IR), as described in the previous paper.[16] The general structure and chemical formulas of synthetic saponites are shown in Figure 1.5 and Table 1.4. According to the paper, the cation-exchange capacity (CEC) of Sap1.2 was 0.99 mequiv. g^{-1}. Since the theoretical specific surface area of the synthetic

saponite is 750 nm^2 g^{-1}, the negative-charge distance of Sap1.2 was calculated to be 1.20 nm on the basis of a hexagonal array. The aqueous dispersion of synthetic saponites, whose particle size is 100 nm or less, is substantially transparent in the UV-visible range. Water was deionized with an ORGANO BB-5A system (PF filter ×2 + G-10 column). 9-Mesityl-10-methylacridinium perchlorate ($MesAcr^+$) was purchased from Tokyo Kasei. The counter ion was exchanged to perchlorate with an ion-exchange resin (Organo, Amberlite Resin IRA-400 treated with $HClO_4$). Organic solvents for spectroscopy were obtained from Kanto Chemical Co., Inc. and were used without further purification.

7.2.1. Analysis

TG-DTA curves were measured with Shimadzu DTG-60H analyzer to determine the water content of $MesAcr^+$ and synthetic saponites. The temperature was ramped from room temperature to 120℃ with a heating rate of 10℃/min under dry air as a purge gas and was held for 60 minutes. Absorption spectra were obtained on a UV-3150 UV-vis. spectrophotometer (SHIMADZU). Fluorescence spectra were obtained on an FP-6500 spectrofluorometer (Jasco), and the excitation light was set at the maximum absorption wavelength of each sample. The reproducibility and signal-to-noise ratio of the fluorescence intensity is 0.5% and 100:1 or higher. The fluorescence quantum yield was determined by the relative method. Rhodamine 6G was used as a standard for the calculation of fluorescence quantum yield of $MesAcr^+$ with and without Sap1.2. The fluorescence quantum yield of Rhodamine 6G in water is 0.90.[17] Fluorescence lifetime was measured by a C4780 picosecond fluorescence lifetime measurement system (Hamamatsu Photonics). An Nd^{3+} YAG laser (EKSPLA PL2210JE + PG-432, fwhm 25 ps, 1 kHz) was used for excitation. The excitation wavelength

was 355 nm. The fluorescence lifetimes were calculated by deconvoluting the excitation pulse in each measurement range.

7.2.2. Sample preparation

The stock solutions of $MesAcr^+$ were prepared in a concentration range of 1.0×10^{-3}–1.0×10^{-4} M. Stock dispersions of Sap1.2 were prepared in a concentration range of 1.0×10^{-3}–1.0×10^{-4} equiv. L^{-1}. In order to prepare $MesAcr^+$-Sap1.2 complexes, above aqueous stock solutions were mixed at an arbitrary rate and were diluted with water under stirring in a quartz cell (1.0 × 1.0 cm). UV-vis absorption spectra were measured under the concentration of 1×10^{-6} M for $MesAcr^+$ and 1×10^{-3} equiv. L^{-1} for Sap1.2. Fluorescence spectra were measured under the concentration of 3.33×10^{-9} M for $MesAcr^+$ and 2.0×10^{-4} equiv. L^{-1} for Sap1.2. Fluorescence lifetimes were measured under the concentration of 4.0×10^{-8} M for $MesAcr^+$ and 4.0×10^{-4} equiv. L^{-1} for Sap1.2.

7.3. Result and discussion

7.3.1. Steady-state results

The adsorption behavior of $MesAcr^+$ on Sap1.2 was evaluated by UV-vis absorption spectra and steady-state fluorescence spectra. The absorption and fluorescence spectra of MesAcr

Table 7.1. Band Maxima of Absorption(λ_{ab}) and Fluorescence(λ_{fl}) of Acridinium Derivatives with and without Sap1.2 in Water

compound	environment	λ_{ab}		λ_{fl}	
		nm	cm^{-1}	nm	cm^{-1}
Acr^+	water	444	22523	462	21645
Acr^+	Sap1.2	448	22321	465	21505
$PhAcr^+$	water	454	22026	485	20619
$PhAcr^+$	Sap1.2	465	21505	490	20408
$MesAcr^+$	water	451	22193	494	20243
$MesAcr^+$	Sap1.2	458	21901	505	19802

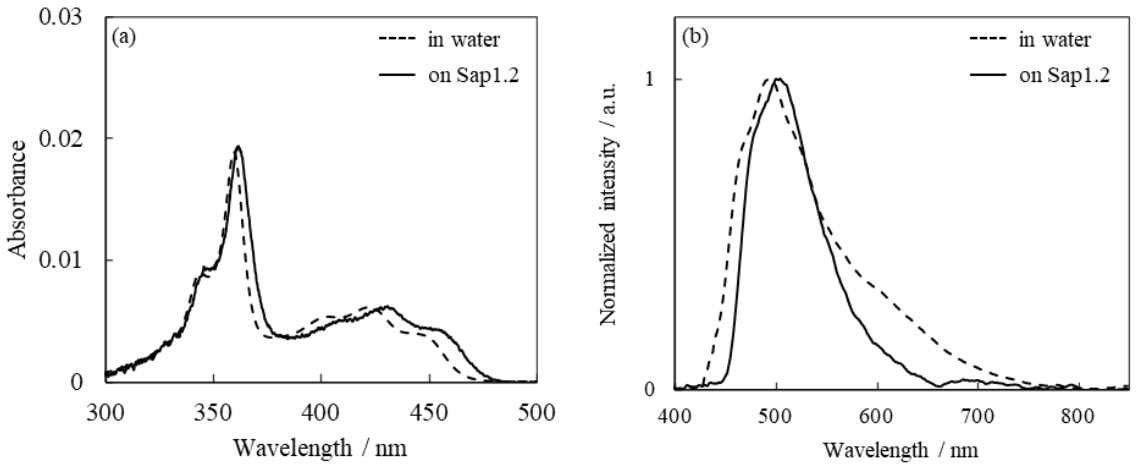

Figure 7.2. (a) UV-vis absorption spectra of $MesAcr^+$ with and without Sap1.2 in aqueous solution. $[MesAcr^+] = 1.0 \times 10^{-6}$ M, [Sap1.2] = 1.0×10^{-3} equiv. L^{-1}. (b) Fluorescence spectra of $MesAcr^+$ with and without Sap1.2 in aqueous solution. $[MesAcr^+] = 3.33 \times 10^{-9}$ M, [Sap1.2] = 2.0×10^{-4} equiv. L^{-1}.

with and without synthetic saponite are shown in Figure 7.1. The maximum absorption and fluorescence wavelength of $MesAcr^+$ are summarized in Table 7.1 with those of Acr^+ and $PhAcr^+$. As shown in Chapter 6, the maximum absorption wavelength of acridinium derivatives shifted to longer wavelengths by adsorption on the clay surface. $PhAcr^+$ and $MesAcr^+$ with a substituent at 9-position showed larger long-wavelength shifts than Acr^+, suggesting that the π-conjugated system was expanded by a flattening of molecules on the clay surface. The long-wavelength shift of $MesAcr^+$ was smaller than that of $PhAcr^+$. It is suggested that the flattening of the MesAcr was suppressed by the steric hindrance of the methyl group in the ortho position of the mesityl group.

The fluorescence spectrum of $MesAcr^+$ in water showed a broad peak at around 600 nm in addition to a peak at 500 nm. Figure 6.3 in Chapter 6 shows that Acr^+ and $PhAcr^+$ do not show such a peak. Since $MesAcr^+$ on the clay surface had no broad fluorescence at 600 nm, it showed a similar fluorescence spectral shape to Acr^+ and $PhAcr^+$. Molecules exhibiting

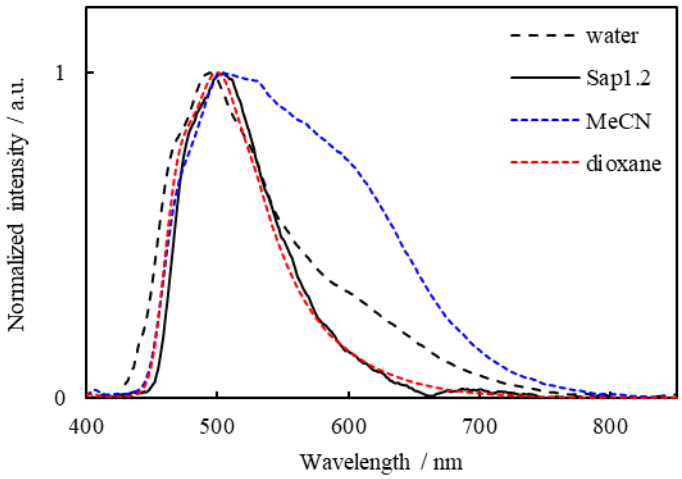

Figure 7.3. Fluorescence spectra of $MesAcr^+$ in water, in acetonitrile, in dioxane, and on Sap1.2.

dual fluorescence from LE and CT state show a change in the ratio of LE to CT depending on the polarity of the solvent.[5,18–20] The fluorescence of LE is dominant in non-polar solvents, while the fluorescence of CT is dominant in polar solvents. Figure 7.3 shows the fluorescence spectra of $MesAcr^+$ in organic solvents with the spectra measured in water. MesAcr in dioxane, a non-polar solvent, showed a sharp fluorescence around 500 nm. MesAcr in acetonitrile, a polar solvent, showed a peak around 600 nm in addition to a fluorescence around 500 nm. The broad peak at 600 nm disappeared in the non-polar solvent, suggesting that the fluorescence around 600 nm of MesAcr was derived from the CT state.

By separating the fluorescence spectra of the LE and CT components in the fluorescence spectrum of $MesAcr^+$, the quantum yield of each component can be obtained.[20] Using the non-linear least-squares method, the fluorescence spectrum of $MesAcr^+$ was expressed as the sum of the fluorescence spectra of the LE and CT components. $F_{Mes}(\nu)$ is expressed by Eq. (7.1), which is the sum of the two fluorescence spectra of LE and CT state.

$$F_{Mes}(\nu) = (1 - f_{CT})F_{LE}(\nu) + f_{CT}F_{CT}(\nu) \qquad (7.1)$$

where v is the frequency (cm^{-1}), $F_{LE}(v)$ is the fluorescence spectrum of LE component, $F_{CT}(v)$ is the fluorescence spectrum of CT component, and f_{CT} is the fraction contribution of CT component. The shifted and broadened shape of the fluorescence spectrum of $PhAcr^+$, $F_{Ph}(v)$, was used as the fluorescence spectrum of the LE component, $F_{LE}(v)$. Shifting and Broadening of $F_{Ph}(v)$ is accomplished by the convolution with a Gaussian function, $g_{LE}(v)$, according to Eq. (7.2) and Eq (7.3).

$$F_{LE}(v) = \int F_{LE}(v-\delta)\, g_{LE}(\delta) d\delta \tag{7.2}$$

$$g_{LE}(\delta) = \frac{1}{\sqrt{2\pi\sigma_{LE}^2}} \exp\left\{-\frac{(\delta-\delta_{LE})^2}{2\sigma_{LE}^2}\right\} \tag{7.3}$$

Since it has been reported that the fluorescence spectrum of CT state, $F_{CT}(v)$, is similar to the Gaussian function,[20] $F_{CT}(v)$ is expressed by the simply Gaussian function as shown in Eq (7.4).

$$F_{CT}(v) = \frac{1}{\sqrt{2\pi\sigma_{CT}^2}} \exp\left\{-\frac{(v-v_{CT})^2}{2\sigma_{CT}^2}\right\} \tag{7.4}$$

where σ_i is the standard deviation of the Gaussian function. The five parameters of this model,

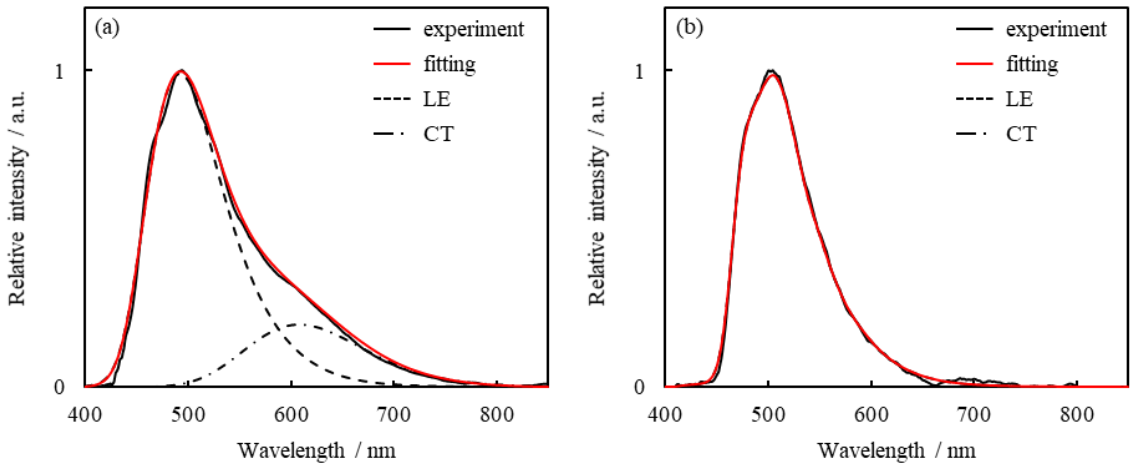

Figure 7.4. Fitting spectra of $MesAcr^+$ (a) in water (b) on Sap1.2.

Table 7.2. Fit Parameters of the Steady-State Fluorescence of $MesAcr^+$

environment	σ_{LE} / cm^{-1}	δ_{LE} / cm^{-1}	σ_{CT} / cm^{-1}	ν_{CT} / cm^{-1}	f_{CT}
water	770	−460	1560	16000	0.270
Sap1.2	1	−130	1560	16000	0.001
dioxane	100	−300	1520	16000	0.040
THF	100	−150	1500	16600	0.280
acetonitrile	703	−20	1457	16347	0.461
acetone	681	0	1490	16266	0.519
methanol	911	−10	1424	16282	0.361
ethanol	699	0	1259	16333	0.266
1-propanol	400	−250	1350	16600	0.220
1-buthanol	180	−180	1450	16600	0.225

$\{\sigma_{LE}, \delta_{LE}, \sigma_{CT}, \nu_{CT}$, and $f_{CT}\}$, are fitted by the non-linear least-squares method. Table 7.2 shows the five parameters of this model of MesAcr in various solvents and the fluorescence quantum yields of LE and CT state calculated by f_{CT}. The fitted fluorescence spectra of $MesAcr^+$ in water and on Sap1.2 are shown in Figure 7.4 as typical spectral fitting. The fitted fluorescence spectra of $MesAcr^+$ in other solvents are shown in Figure S7.1.

The LE and CT fluorescence ratios of $MesAcr^+$ in water were 83% and 17%, respectively. The fluorescence quantum yields of LE and CT states of $MesAcr^+$ in water were 0.0005 and 0.0001, respectively. On the other hand, $MesAcr^+$ on the clay surface emitted only LE fluorescence. The fluorescence quantum yields of the LE state of $MesAcr^+$ on the clay surface was 0.0462. The fluorescence quantum yield of the LE state of $MesAcr^+$ on the clay surface was 90 times that in water. The fluorescence quantum yield of the LE state of $MesAcr^+$ on the clay surface also exceeded that in dioxane. Even when $MesAcr^+$ was present in dioxane, the non-polar solvent, the LE fluorescence was slightly mixed with CT fluorescence. MesAcr mainly exhibited LE fluorescence in non-polar solvents, suggesting that the behavior of TICT-

active molecules was affected by the surrounding environment. $MesAcr^+$ on the clay surface showed a higher ratio and quantum yield of LE fluorescence compared with other environments was attributed to the hydrophobic and smooth environment of the clay, which suppressed the rotational nature of $MesAcr^+$.

7.3.2. Time-resolved results

The kinetics, including LE and CT states, is described as shown in Figure 7.5. The rate constants k^{LE} and k^{CT} indicate the deactivation rate constants of LE and CT states, including radiative and nonradiative processes, respectively. The formation rate constants k_{ET} and k_{BET} denote the forward and reverse charge transfer rate constants between LE and CT states. In order to clarify the kinetics of MesAcr as described in Figure 7.5, we attempted to calculate the rate constants for each process. The fluorescence decay curve was used for kinetic analysis. The kinetic equations for the concentration of LE* and CT* states could be represented as shown in Eq. (7.5) and Eq. (7.6).[4]

$$\frac{[LE^*]}{[LE^*]_0} = \frac{1}{\gamma_1 - \gamma_2}\{(X - \gamma_2)e^{-\gamma_1 t} - (X - \gamma_2)e^{-\gamma_2 t}\} \tag{7.5}$$

$$\frac{[CT^*]}{[LE^*]_0} = \frac{k_{ET}}{\gamma_1 - \gamma_2}\{e^{-\gamma_1 t} - e^{-\gamma_2 t}\} \tag{7.6}$$

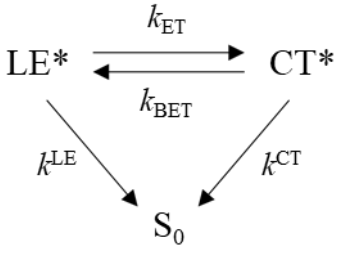

Figure 7.5. Reaction kinetics of $MesAcr^+$ with the relevant rate constants.

γ_1, γ_2, X, and Y are expressed as follows, respectively.

$$X = k^{LE} + k_{ET} \tag{7.7}$$

$$Y = k^{CT} + k_{BET} \tag{7.8}$$

$$\gamma_1 = \frac{1}{2}\left\{(X+Y) + \sqrt{(X-Y)^2 + 4k_{ET}k_{BET}}\right\} \tag{7.9}$$

$$\gamma_2 = \frac{1}{2}\left\{(X+Y) - \sqrt{(X-Y)^2 + 4k_{ET}k_{BET}}\right\} \tag{7.10}$$

Since an iterative fitting method is necessary to determine four unknown rate constants,[4,21,22] the method was applied to the deconvoluted fluorescence decay curve.

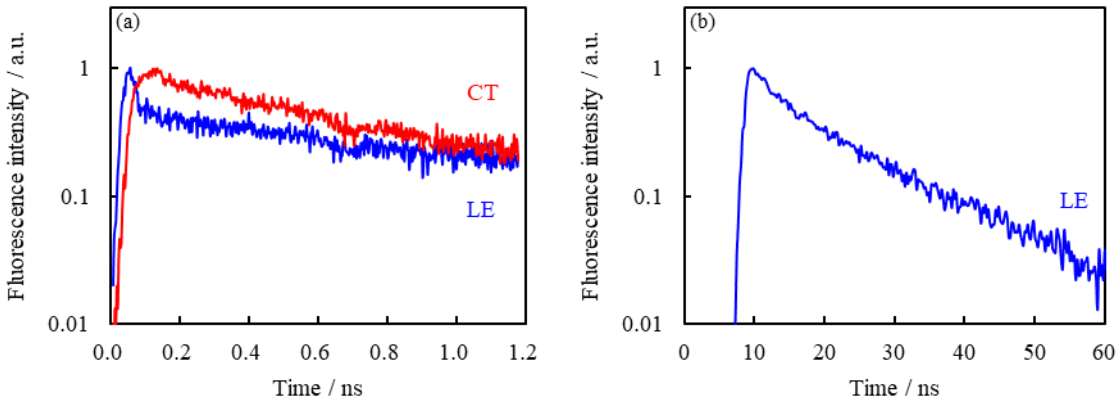

Figure 7.6. Fluorescence decay curves of $MesAcr^+$ (a) in water and (b) on Sap1.2. The decay of LE fluorescnece was observed at 500−550 nm. The decay of CT fluorescnece was observed at 650−700 nm.

Table 7.3. Fluorescence Lifetimes and Rate Constants of the $MesAcr^+$ with and without Sap1.2 in Water

environment	λ_{fl} / nm	τ_1 / ns	τ_2 / ns	a_1	a_2	k^{LE} / s^{-1}	k^{CT} / s^{-1}	k_{ET} / s^{-1}	k_{BET} / s^{-1}
water	500–550	0.008	1.11	0.95	0.05	2.0×10^8	9.5×10^8	1.2×10^{11}	6.5×10^9
	650–700	0.007	0.57	−1.00	1.00	1.0×10^7	1.8×10^9	1.4×10^{11}	6.6×10^9
	average	-	-	-	-	1.1×10^8	1.4×10^9	1.3×10^{11}	6.5×10^9
Sap1.2	500–550	1.17	13.79	0.43	0.57	1.2×10^8	6.4×10^5	2.9×10^8	5.1×10^8
	650–700	-	-	-	-	-	-	-	-
	average	-	-	-	-	1.2×10^8	6.4×10^5	2.9×10^8	5.1×10^8

Fluorescence decay curves of $MesAcr^+$ in water and on the clay surface are shown in Figure 7.6. The lifetime analysis by the deconvolution method provides a time resolution of about a tenth of the instrumental response function (IRF).[23] In this case, the time resolution is 2~3 ps since the instrumental response function is about 25 ps. Table 7.3 lists the fluorescence lifetime and the resulting rate constants of $MesAcr^+$ in water and on the clay surface calculated by the iterative fitting method. It should be noted that iterative fitting was applied only to the decay curve of LE fluorescence since $MesAcr^+$ on the clay surface has no CT fluorescence.

$MesAcr^+$ in water showed a fast decay in LE fluorescence and a fast rise in CT fluorescence, suggesting the fast charge transfer from LE to CT state occurred. On the other hand, $MesAcr^+$ on the clay surface has no CT fluorescence, and the decay of LE fluorescence was slower than that in water. It is suggested that the adsorption on the clay surface affects the charge transfer from LE to CT state.

The k^{CT} on the clay surface was smaller than in water, although the k^{LE} on the clay surface was the same as that in water. It is indicated that the deactivation process from the CT state has almost disappeared. The lower fluorescence quantum yield of $MesAcr^+$ in water was due to the low quantum yield of CT fluorescence. The fluorescence quantum yield of $MesAcr^+$ on the clay surface was higher than in water due to the disappearance of this process. Both k_{ET} and k_{BET} on the clay surface were smaller than in water. The free energy change ΔG is given by the following equation:

$$\Delta G = -RT \ln \frac{k_{ET}}{k_{BET}} \tag{7.11}$$

The ΔG of the transition from LE to CT state in water and on the clay surface were −7.2 and 1.2 kJ/mol, respectively. This result indicates that the charge transfer to the CT state in water

is an exergonic reaction, whereas on the clay surface is an endergonic reaction. It is suggested that the charge transfer between the donor and acceptor in the $MesAcr^+$ was less likely to occur. In order to refine the above conclusions, the k^{LE} and k^{CT} were resolved into the radiative and non-radiative deactivation rate constants. The fluorescence quantum yields of LE and CT states in the reversible regime are expressed as the following equations:[24]

$$\Phi_f^{LE} = \frac{k_f^{LE} Y}{XY - k_{ET} k_{BET}} \tag{7.12}$$

$$\Phi_f^{CT} = \frac{k_f^{CT} k_{ET}}{XY - k_{ET} k_{BET}} \tag{7.13}$$

where k_f is the radiative deactivation rate constant. The non-radiative deactivation rate constant k_{nr} is expressed as the following equation:

$$k^i = k_f^i + k_{nr}^i \tag{7.14}$$

The k_f and k_{nr} of the LE and CT states are tabulated in Table 7.4. Both k_f^{LE} and k_{nr}^{LE} on the clay surface was smaller than in water. Since $MesAcr^+$ on the clay surface had no CT fluorescence, k_f^{CT} was zero. However, k_{nr}^{CT} on the clay surface was one in a thousand compared with that in water. It can thus be suggested that the significant decrease of k_{nr}^{CT} is the factor of the disappearance of the decay from the CT state.

Let us discuss how the adsorption on the clay affected the potential curves of LE and CT

Table 7.4. Deactivation Rate Constants of the $MesAcr^+$ with and without Sap1.2 in Water

environment	k_f^{LE} / s^{-1}	k_{nr}^{LE} / s^{-1}	k_f^{CT} / s^{-1}	k_{nr}^{CT} / s^{-1}
water	1.1×10^7	9.4×10^7	1.7×10^5	1.4×10^9
Sap1.2	5.6×10^6	1.1×10^8	0	6.4×10^5

states from the above rate constant changes. Figure 7.7 shows the plausible potential curves of $MesAcr^+$ in water and on the clay surface. The significant decrease of k_{nr}^{CT} indicates the decrease of internal crossing, suggesting that the potential curve of the CT state is sharpened. The positive ΔG between LE and CT states when $MesAcr^+$ adsorbed on the clay surface suggests that the relative position of the CT state is higher than the LE state. The absorption spectra in Figure 7.2 shows that the orthogonal donor and acceptor become planer when $MesAcr^+$ is adsorbed on the clay surface. Since the stable state of the CT state is presumed to be orthogonal, it is presumed that the relative position of the CT state is higher than that of the LE state because the planarization destabilized the orthogonal structure. Chapter 6 in this thesis and previous papers have provided sharpening and resembling the potential curve as the effects of S-FIE.[25–28] The results in this Chapter newly propose that the effect of S-FIE is to increase the ΔG of the charge transfer to CT state to the positive side.

Moreover, it has been reported that the relative positions of the potential curves of LE and

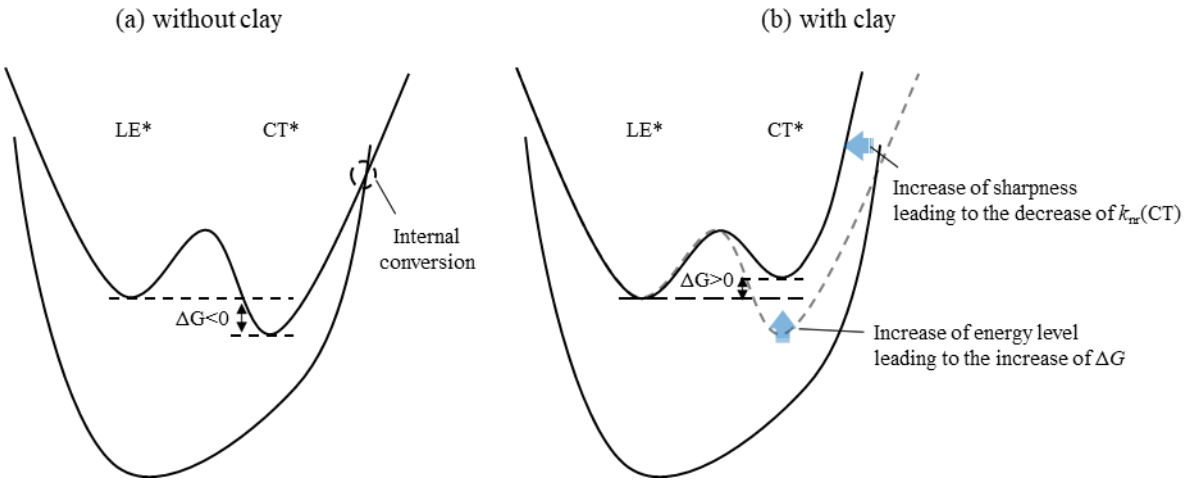

Figure 7.7. Plausible conceptual potential energy curves of ground and excited states for $MesAcr^+$. (a) Without clay (b) With clay.

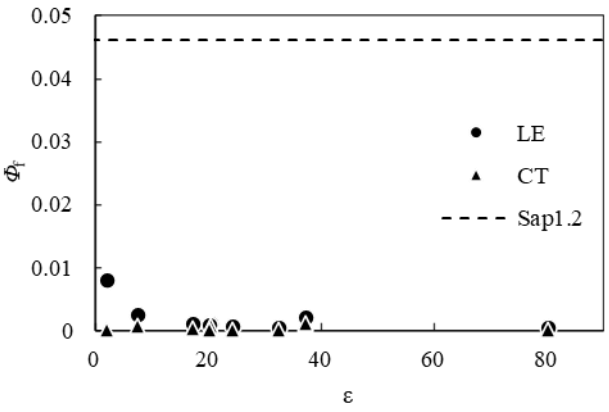

Figure 7.8. Relationship between the fluorescence quantum yields (Φ_f) of $MesAcr^+$ and the dielectric constants (ε)

CT state in the TICT-active molecules change with the solvent polarity (5). In particular, the LE fluorescence is predominant in non-polar solvents. As shown in Figure 7.8, the solvent polarity also affected the ratio of LE and CT fluorescence of $MesAcr^+$. $MesAcr^+$ adsorbed on the clay surface emitted only LE fluorescence, suggesting that their surface provides a very hydrophobic environment, although clay minerals are colloids dispersed in water.

7.4. Conclusion

Chapter 7 investigated the adsorption behavior of $MesAcr^+$ on the clay surface by absorption spectra, steady-state fluorescence spectra, and time-resolved fluorescence to explain the influence of the clay surface on the potential curve of TICT-active molecules.

$MesAcr^+$ showed dual fluorescence from the LE and CT states. The ratio of the two components varied depending on the surrounding environment, such as solvent. The dual fluorescence of $MesAcr^+$ was expressed as the sum of the LE and CT components using the nonlinear least-squares method. The fluorescence of $MesAcr^+$ in non-polar solvents and on the clay surface showed a high ratio of LE fluorescence. $MesAcr^+$ on the clay surface showed a higher ratio and quantum yield of LE fluorescence compared with other environments was

attributed to the hydrophobic and smooth environment of the clay, which suppressed the rotational nature of $MesAcr^+$.

In order to analyze the dual fluorescence dynamically, several unknown rate constants were obtained by applying an iterative fitting method to the fluorescence decay curve of $MesAcr^+$. The k_{nr}^{CT} was decreased when $MesAcr^+$ adsorbed on the clay surface, indicating the decrease of internal crossing. This result suggests that the potential curve of the CT state is sharpened. Moreover, the ΔG of the charge transfer, which was a negative value in water, became positive when $MesAcr^+$ adsorbed on the clay surface. The positive ΔG suggests that the relative position of the CT state is higher than the LE state. It is newly proposed as the effect of S-FIE. Moreover, these results suggest that the clay surface provides a very hydrophobic environment, although clay minerals are colloids dispersed in water.

7.5. Supporting information

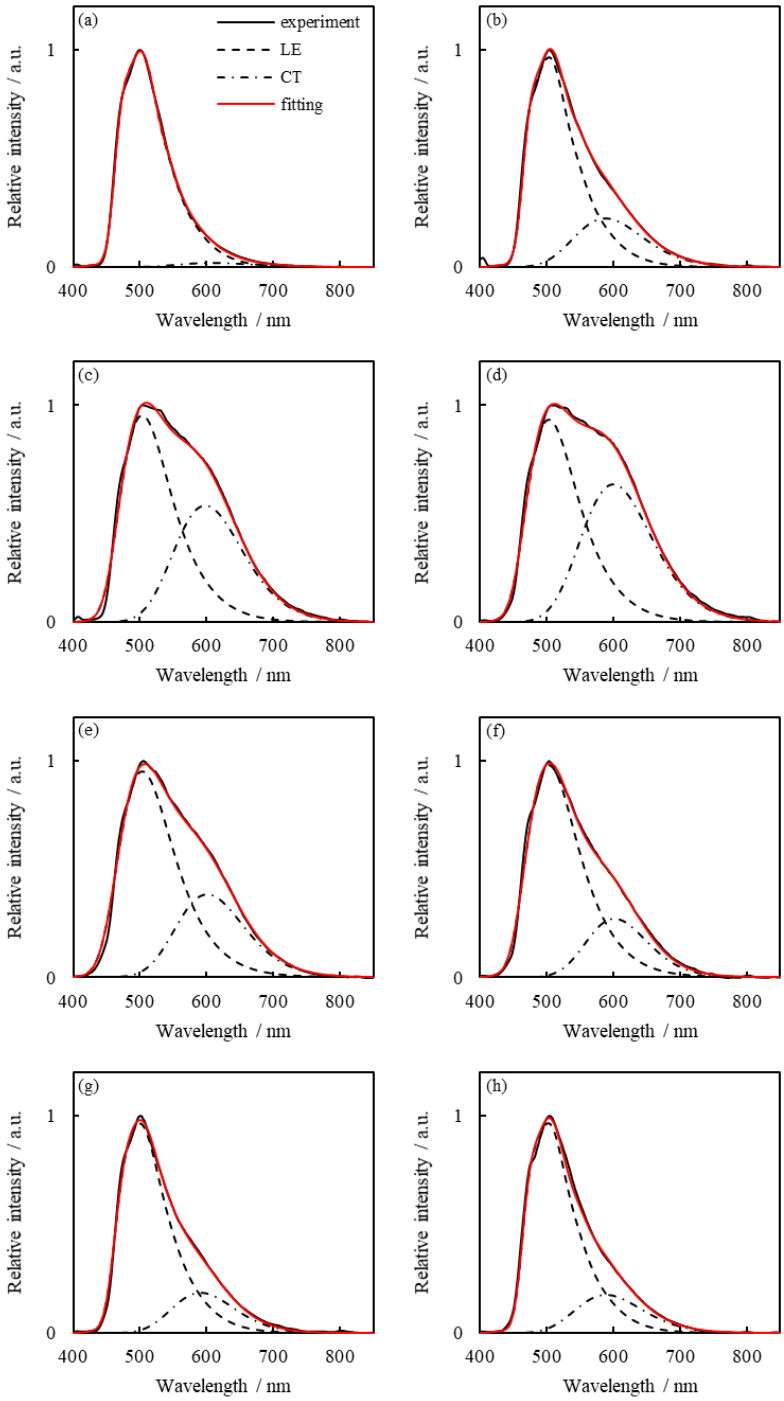

Figure S7.1. Fitted fluorescence spectra of $MesAcr^+$ in (a) dioxane, (b) THF, (c) acetonitrile, (d) acetone, (e) methanol, (f) ethanol, (g) 1-propanol, and (h) 1-buthanol.

7.6. References

1. Grabowski, Z. R.; Rotkiewicz, K.; Rettig, W. Structural Changes Accompanying Intramolecular Electron Transfer: Focus on Twisted Intramolecular Charge-Transfer States and Structures. *Chem. Rev*. **2003**, *103*, 3899-4032.
2. Druzhinin, S. I.; Ernsting, N. P.; Kovalenko, S. A.; Lustres, L. P.; Senyushkina, T. A.; Zachariasse, K. A. Dynamics of Ultrafast Intramolecular Charge Transfer with 4-(Dimethylamino)benzonitrile in Acetonitrile. *J. Phys. Chem. A* **2006**, *110*, 2955-2969.
3. Zirak, P.; Penzkofer, A.; Mathes, T.; Hegemann, P. Photo-Dynamics of Roseoflavin and Riboflavin in Aqueous and Organic Solvents. *Chem. Phys*. **2009**, *358*, 111-122.
4. Rumble, C. A.; Maroncelli, M. Solvent Controlled Intramolecular Electron Transfer in Mixtures of 1-Butyl-3-methylimidizolium Tetrafluoroborate and Acetonitrile. *J. Chem. Phys*. **2018**, *148*, 193801.
5. Kuramoto, Y.; Nakagiri, T.; Matsui, Y.; Ohta, E.; Ogaki, T.; Ikeda, H. A Leaning Amine–Ketone Dyad with a Nonconjugated Linker: Solvatofluorochromism and Dual Fluorescence Associated with Intramolecular Charge Transfer. *Photochem. Photobiol. Sci*. **2018**, *17*, 1157-1168.
6. Chen, D. G.; Ranganathan, R.; Lin, J. A.; Huang, C. Y.; Ho, M. L.; Chi, Y.; Chou, P. T. Ratiometric Tuning of Luminescence: Interplay between the Locally Excited and Interligand Charge-Transfer States in Pyrazolate-Based Boron Compounds. *J. Phys. Chem. C* **2019**, *123*, 4022-4028.
7. Benniston, A. C.; Harriman, A.; Li, P.; Rostron, J. P.; van Ramesdonk, H. J.; Groeneveld, M. M.; Zhang, H.; Verhoeven, J. W. Charge Shift and Triplet State Formation in the 9-Mesityl-10-methylacridinium Cation. *J. Am. Chem. Soc*. **2005**, *127*, 16054-16064.

8. Fukuzumi, S.; Kotani, H.; Ohkubo, K.; Ogo, S.; Tkachenko, N. V.; Lemmetyinen, H. Electron-Transfer State of 9-Mesityl-10-methylacridinium Ion with a Much Longer Lifetime and Higher Energy Than That of the Natural Photosynthetic Reaction Center. *J. Am. Chem. Soc.* **2004**, *126*, 1600-1601.

9. Ohkubo, K.; Kotani, H.; Fukuzumi, S. Misleading Effects of Impurities Derived from the Extremely Long-Lived Electron-Transfer State of 9-Mesityl-10-methylacridinium Ion. *Chem. Commun.* **2005**, 4520-4522.

10. Tanaka, M.; Ohkubo, K.; Gros, C. P.; Guilard, R.; Fukuzumi, S. Persistent Electron-Transfer State of a π-Complex of Acridinium Ion Inserted between Porphyrin Rings of Cofacial Bisporphyrins. *J. Am. Chem. Soc*. **2006**, *128*, 14625-14633.

11. Tsukada, T.; Kotani, H.; Ohkubo, K.; Nakagawa, T.; Tkachenko, N. V.; Lemmetyinen, H.; Fukuzumi, S. Photoinduced Electron Transfer in 9-Substituted 10-Methylacridinium Ions. *Chem. Eur. J.* **2014**, *23*, 1306-1317.

12. Ohkubo, K.; Nanjo, T.; Fukuzumi, S. Efficient Photocatalytic Oxygenation of Aromatic Alkene to 1,2-Dioxetane with Oxygen via Electron Transfer, *Org. Lett*. **2005**, *7*, 4265-4268.

13. Joshi-Pangu, A.; Lévesque, F.; Roth, H. G.; Oliver, S. F.; Campeau, L.; Nicewicz, D. A.; Dirocco, D. Acridinium-Based Photocatalysts: A Sustainable Option in Photoredox Catalysis. *J. Org. Chem.* **2016**, *81*, 7244-7249.

14. Mcmanus, J. B.; Nicewicz, D. A. Direct C–H Cyanation of Arenes via Organic Photoredox Catalysis. *J. Am. Chem. Soc.* **2017**, *139*, 2880-2883.

15. Ohkubo, K.; Mizushima, K.; Iwata, R.; Fukuzumi, S. Selective Photocatalytic Aerobic Bromination with Hydrogen Bromide via an Electron-Transfer State of 9-Mesityl-10-

methylacridinium Ion. *Chem. Sci.* **2011**, *2*, 715-722.

16. Egawa, T.; Watanabe, H.; Fujimura, T.; Ishida, Y.; Yamato, M.; Masui, D.; Shimada, T.; Tachibana, H.; Yoshida, H.; Inoue, H.; Takagi, S. Novel Methodology To Control the Adsorption Structure of Cationic Porphyrins on the Clay Surface Using the "Size-Matching Rule." *Langmuir* **2011**, *27*, 10722-10729.

17. Magde, D.; Wong, R.; Seybold, P. G. Fluorescence Quantum Yields and Their Relation to Lifetimes of Rhodamine 6G and Fluorescein in Nine Solvents: Improved Absolute Standards for Quantum Yields. *Photochem. Photobiol*. **2002**, *75*, 327-334.

18. Dahl, K.; Biswas, R.; Ito, N.; Maroncelli, M. Solvent Dependence of the Spectra and Kinetics of Excited-State Charge Transfer in Three (Alkylamino)benzonitriles. *J. Phys. Chem. B* **2005**, *109*, 1563-1585.

19. Li, X.; Maroncelli, M. Solvent-Controlled Electron Transfer in Crystal Violet Lactone. *J. Phys. Chem. A* **2011**, *115*, 3746-3754.

20. Li, X.; Liang, M.; Chakraborty, A.; Kondo, M.; Maroncelli, M. Solvent-Controlled Intramolecular Electron Transfer in Ionic Liquids. *J. Phys. Chem. B*. **2011**, *115*, 6592-6607.

21. Nishimura, Y.; Shimamura, K.; Ohmori, Y.; Shinohara, Y.; Arai, T. Kinetic Studies of Emissive Guanine Derivatives Bearing Anthracene Moiety. *J. Photochem. Photobiol*. **2011**, *218*, 69-75.

22. Tang, K. C.; Chang, M. J.; Lin, T. Y.; Pan, H. A.; Fang, T. C.; Chen, K. Y.; Hung, W. Y.; Hsu, Y. H.; Chou, P. T. Fine Tuning the Energetics of Excited-State Intramolecular Proton Transfer (ESIPT): White Light Generation in A Single ESIPT System. *J. Am. Chem. Soc.* **2011**, *133*, 17738-17745.

23. O'Connor, D. V.; Phillips, D. *Time-Correlated Single Photon Counting*, Academic Press, 1984, Chapter 7, 211-251.

24. Maus, M.; Rettig, W. The Excited State Equilibrium between Two Rotational Conformers of a Sterically Restricted Donor−Acceptor Biphenyl As Characterized by Global Fluorescence Decay Analysis. *J. Phys. Chem. A* **2002**, *106*, 2104-2111.

25. Tsukamoto, T.; Shimada, T.; Takagi, S. Unique Photochemical Properties of *p*-Substituted Cationic Triphenylbenzene Derivatives on a Clay Layer Surface. *J. Phys. Chem. C* **2013**, *117*, 2774-2889.

26. Ishida, Y.; Shimada, T.; Takagi, S. "Surface-Fixation Induced Emission" of Porphyrazine Dye by a Complexation with Inorganic Nanosheets. *J. Phys. Chem. C* **2014**, *118*, 20466-20471.

27. Tsukamoto, T.; Shimada, T.; Takagi, S. Structure Resembling Effect of Clay Surface on Photochemical Properties of meso-phenyl or Pyridyl-substituted Monocationic Antimony(V) Porphyrin Derivatives. *RSC Adv*. **2015**, *5*, 8479-8485.

28. Tokieda, D.; Tsukamoto, T.; Ishida, Y.; Ichihara, H.; Shimada, T.; Takagi, S. Unique Fluorescence Behavior of Dyes on the Clay Minerals Surface: Surface Fixation Induced Emission (S-FIE). *J. Photochem. Photobio. A: Chem.* **2017**, *339*, 67-79.

Chapter 8. Summary

This thesis aimed to elucidate the driving force for the adsorption of cationic acridinium derivatives on synthetic saponites and their photophysical behavior. Mono-cationic acridinium derivatives and synthetic saponites, whose inter-negative charge distance on the surface can be modulated, were selected as guest molecules and host materials, respectively. Their complex formation behavior was evaluated.

Chapters 2 and 3 evaluated the effects of the guest molecule and host material structures on the adsorption of acridinium derivatives on clay minerals. The adsorption behavior of acridinium derivatives on synthetic saponites was expressed by a two-components equilibrium system of adsorbed and non-adsorbed components, indicating that acridinium derivatives adsorb on Sap1.2 without aggregation. Negative enthalpy change (ΔH) and positive entropy change ($T\Delta S$), which were calculated by van't Hoff plot, indicate that both van der Waals interaction and hydrophobic interaction contributed to the adsorption of acridinium derivatives on synthetic saponites. The thermodynamic parameters strongly correlate with the molecular cross-sectional area of acridinium derivatives and the negative charge distance of synthetic saponites. The increase in ΔH and decrease in $T\Delta S$ with the increase in the molecular cross-sectional area suggest the decrease in the contribution of hydrophobic interaction on adsorption. The increase in ΔH and decrease in $T\Delta S$ with the increase in the negative charge distance also suggest the decrease in the contribution of hydrophobic interaction on the adsorption. These results propose that the molecular cross-sectional area and negative charge distance affect the driving force for the adsorption.

Chapter 4 evaluated the compensation relationship between ΔH and $T\Delta S$ for the adsorption

of acridinium derivatives on synthetic saponites. The enthalpy-entropy compensation plot of the adsorption of acridinium derivatives on synthetic saponites showed a linear relationship with a small slope specific to rigid host materials and a large intercept specific to soft host materials. ΔH and $T\Delta S$ of adsorption of cationic dyes on clay minerals were surveyed from previous papers. The slopes and intercepts of enthalpy-entropy compensation calculated from previously reported ΔH and $T\Delta S$ of adsorption of cationic dyes on clay minerals were about 0.9 and 7.0, respectively, regardless of the type of clay minerals. This suggests that the structural change and desolvation during complexation are affected by the concentration of clay minerals rather than the type of clay minerals

Chapter 5 evaluated the fluorescence self-quenching behavior of acridinium derivatives on synthetic saponites. The presence or absence of a substituent at the 9-position of the acridinium derivative had no significant influence on the self-quenching behavior. The intermolecular distances at which fluorescence quenching started were almost 50–100 nm regardless of the negative charge distance of the synthetic saponite. This result suggests that it is important to eliminate the segregation of dye molecules on the clay surface and establish a state in which the number of dye molecules is one or less per clay to suppress the self-fluorescence quenching of mono-cationic dyes.

Chapter 6 evaluated the effects of guest and host structures on the fluorescence enhancement behavior of acridinium derivatives on synthetic saponites. Although the fluorescence quantum yield (Φ_f) of Acr^+ on the clay surface became smaller than in water, Φ_f of $PhAcr^+$ was enhanced approximately 20 times by the adsorption on the clay surface. In addition, as the inter-negative charge distance on the clay surface increased, Φ_f of $PhAcr^+$ increased. It has been clarified that the fluorescence was enhanced by the increase in the

radiative deactivation rate constant and the decrease in the radiative deactivation rate constant due to the fixation of rotational substituents on the clay surface. It was found that an increase in the inter-negative charge distance on the clay surface further amplified these effects, resulting in even greater fluorescence enhancement. These results suggest that not only the guest dye structure but also the clay structure as host materials affected the photophysical property of dyes adsorbed on the clay surface.

Chapter 7 evaluated the adsorption behavior of 9-mesityl-10-methylacridinium ($MesAcr^+$) on the clay surface to explain the influence of the clay surface on the potential curve of TICT-active molecules. The fluorescence of $MesAcr^+$ in non-polar solvents and on the clay surface showed a high ratio of LE fluorescence. The non-radiative deactivation rate constant k_{nr}^{CT} was decreased when $MesAcr^+$ adsorbed on the clay surface. These results suggest that the potential curve of the CT state is sharpened. Moreover, the ΔG of the charge transfer, which was a negative value in water, became positive when $MesAcr^+$ adsorbed on the clay surface. The positive ΔG suggests that the relative position of the CT state is higher than the LE state. It is newly proposed as the effect of S-FIE. Moreover, these results suggest that the clay surface provides a very hydrophobic environment, although clay minerals are colloids dispersed in water.

This thesis elucidated the influence of the structure of the guest molecule, acridinium derivative, and the host material, clay minerals, on the adsorption and photophysical behaviors. It is suggested that clay minerals have an ideal space to form a strong complex. These investigations provide new strategies for using the complex of mono-cationic dyes and clay minerals as photo-functional materials and will facilitate the organic-inorganic composites with new functions in the future.

List of Publications

Takigawa, T.; Yoshida, Y.; Fujimura, T.; Ishida, T.; Shimada, T.; Takagi, S. Adsorption Behavior of Mono-Cationic Pyridinium Salts on the Clay Surface. *Bull. Chem. Soc. Jpn*. **2020**, *93*, 1046–1049.

Yoshida. Y; Shimada. T; Ishida. T; Takagi. S; Thermodynamic study for Adsorption of Acridinium Derivatives on the Clay Surface. *RSC Adv*. **2020**, *10*, 21360-21368.

Yoshida. Y; Shimada. T; Ishida. T; Takagi. S. Effects of Surface Charge Density of Clay Minerals on Surface-fixation Induced Emission (S-FIE) of Acridinium Derivatives. *ACS Omega* **2021**, *6*, 21702–21708.

Acknowledgments

This thesis has been carried out under the supervision of Professor Shinsuke Takagi at the Division of Applied Chemistry for Environment, Graduate School of Urban Environmental Sciences, Tokyo Metropolitan University.

First, I would like to express my sincere gratitude to Professor Shinsuke Takagi at the Division of Applied Chemistry for Environment, Graduate School of Urban Environmental Sciences, Tokyo Metropolitan University, for his valuable advice, encouragement, and hospitality. I would also like to thank him for graciously accepting my entry into the doctoral program.

I would like to thank Associate Professor Takashi Takei, Associate Professor Tamao Ishida, and Assistant Professor Tetsuya Shimada at the Division of Applied Chemistry for Environment, Graduate School of Urban Environmental Sciences, Tokyo Metropolitan University, for their helpful advice and comments.

I would like to thank the members of the research group under the direction of Professor Shinsuke Takagi for their kind support.

I would like to thank Mr. Hiroaki Takahashi, Dr. Masato Nishimura, Mr. Tomoyuki Nakamura, and all my colleagues at the former Transparent Materials R&D Dept and Information and Communication R&D Center of Showa Denko Materials Co., Ltd. for their understanding and support in conducting this research.

I would like to thank Dr. Shigeaki Funyu, my senior in the laboratory and in the company, for his encouragement and advice in going on to the doctoral program.

I would like to thank my mother, Nami Yoshida, and my late father, Masahiro Yoshida, my father-in-law, Dr. Masafumi Hirato, and my mother-in-law, Dr. Junko Hirato, and their families for their understanding and support.

Finally, I would like to express my deepest gratitude to my wife, Shiho Yoshida, for her support and heartfelt encouragement. Without her support, this thesis would not have been possible.

March 7th, 2022

Yuma YOSHIDA